School of Earth and Planetary Sciences

A Geochronological and Thermobarometric Investigation of Eclogites and overlying Hyllestad Schists from the Southern Western Gneiss Complex, Norway

Sean W. Makin
0000-0001-5057-1977

This thesis is presented for the Degree of
Master of Research (Earth and Planetary Sciences)
of
Curtin University

January 2021

DECLARATION

To the best of my knowledge and belief this thesis contains no material previously published by any other person except where due acknowledgement has been made. This thesis contains no material which has been accepted for the award of any other degree or diploma in any university.

The author acknowledges that copyright of published works contained within this thesis resides with the copyright holder(s) of those works. I warrant that I have obtained, where necessary, permission from the copyright owners to use any third-party copyright material reproduced in the thesis (e.g. questionnaires, artwork, unpublished letters), or to use any of my own published work (e.g. journal articles) in which the copyright is held by another party (e.g. publisher, co-author).

Sean W. Makin	12/01/2021
	Date

ABSTRACT

The Nordfjord–Sogn Detachment zone (NSD) in western Norway is a large-scale (>100 km long) brittle–ductile extensional structure of Caledonian age. In the Sognefjorden area, the NSD juxtaposes mostly metapelitic rocks of the allochthonous Hyllestad Complex in the hanging wall, against mostly felsic gneisses of the (para)autochthonous Western Gneiss Complex (WGC) in the footwall. Phase equilibrium modelling of a suite of eclogite pods and lenses within the southern part of the WGC, from which data are scarce, indicate peak *P–T* conditions of 24–28 kbar and 670–780˚C, conditions that plot along the *P–T* trajectory for a large number of analysed samples from more northern exposures within the WGC. These data, which potentially reflect a fossilised subduction geotherm, support a model of more-or-less homogenous subduction and exhumation across the entire Western Gneiss Complex. Phase equilibrium modelling of an aluminous schist with the assemblage garnet–kyanite–staurolite–muscovite–paragonite–ilmenite–rutile–quartz from the Hyllestad Complex indicates peak *P–T* conditions of 14–15 kbar and 600–650˚C were reached at c. 429–425 Ma. These peak conditions record a geothermal gradient that is significantly warmer than proposed in numerous other studies from the WGC and overlying rocks. Micro-shear bands, defined by an alignment of fine-grained biotite and sillimanite, are interpreted to record top-to-the-east movement of the NSD. Marginal replacement of kyanite porphyroblasts by sillimanite suggests that the rocks were exhumed to depths of less than 20 km at high temperature. Shear heating during exhumation along the NSD is proposed to account for this thermal perturbation, in which the heat supplied was sufficient to maintain near-isothermal conditions during exhumation. Extension during the waning stages of the Scandian phase of Caledonian orogenesis facilitated rapid juxtaposition of a very large (30 km) section of crust along the NSD, allowing the preservation of high temperatures at shallow depths, likely reflecting 70–100 km of movement along the detachment surface. Subsequent to this movement, the Hyllestad Complex would have been exhumed to depth of less than 20 km account for cooling through rutile closure temperatures at 575–600˚C, which was followed by a greenschist to amphibolite facies overprint. These rutile cooling ages are similar to those obtained from former ultrahigh-pressure domains further to the north, indicating near homogeneous flat-slab exhumation after activation of the NSD.

ACKNOWLEDGEMENTS

I am incredibly grateful to both Chris Clark and Tim Johnson for this amazing opportunity to study and observe an amazing aspect of the earth's geology in the field and the lab. Your support, time given, occasional kick along and importantly sense of humour throughout the past few years is greatly appreciated. I guess Seamus has stuck?

To Andrew Kylander-Clark and Martin Hand I cannot thank you enough for your time and assistance in the field, your knowledge and discussion of all things Western Gneiss as well as making for a great week spent in Norway is greatly appreciated.

Without the help of staff from various facilities around the world this thesis would not have been possible. Thanks to Ben Wade at Adelaide Microscopy, Adelaide University your patience in teaching the ins and outs of the electron microprobe. To Noreen Evans, Brad Mcdonald and Kai Rankenburg from the GeoHistory Facility, Curtin University; your assistance and time with LA–ICP–MS setup, operation and introducing me to data reduction and all laser ablation is appreciated. To Jeff Vervoort and Chao Zhang your time, knowledge and guidance while visiting the Radiogenic Isotope and Geochronology Laboratory, Washington State University was invaluable, along with Chris Fisher and Da Wang for their assistance and keeping me sane for many long hours running on the Neptune.

To Nick Timms, thank you for helping us get through the teething stages of the degree and for always having an open door to chat all things structural. To Pete Kinny, thank you for as always making teaching mineralogy ever humorous and other enlightening conversations that came along with it. I also have enormous gratitude towards too many other staff members at Curtin to name, your time, from a quick corridor discussion to something more in-depth about all aspects of geology, your time and expertise is much appreciated.

Finally, a massive thank you to Mum and Dad and the rest of my family for all your love and support throughout the past few years at Curtin.

TABLE OF CONTENTS

LIST OF ADDITIONAL PUBLICATIONS RELEVANT TO THE THESIS

The publications are listed below, as well as their reason for their inclusion as part of the additional publications.

CONFERENCE PRESENTATION: Makin, S., Clark, C., Johnson, T.E., Kylander-Clark, A.R.C, and Hand, M. 2019, Shear heating during exhumation: An example from the Nordfjord–Sogn Detachment, Hyllestad, Norway: SGTSG – Convergence on the Coast 2019, 17–22 November, Port Lincoln, South Australia.

– This presentation at an international conference is for the work in Chapter 3.

LIST OF FIGURES

LIST OF TABLES

1. INTRODUCTION

INTRODUCTION

The early Palaeozoic Western Gneiss Complex (WGC) of southwestern Norway (Figure 1.1) represents one of the world's largest and most well-exposed occurrences of a high to ultrahigh-pressure terrane. The WGC has an areal extent of > 30,000 km^2 with 5,000 km^2 of this region inferred to have experienced ultrahigh-pressure conditions (Kylander-Clark, Hacker, Johnson, Beard, & Mahlen, 2009; Kylander-Clark et al., 2007; Kylander-Clark, Hacker, & Mattinson, 2008; Root et al., 2005).

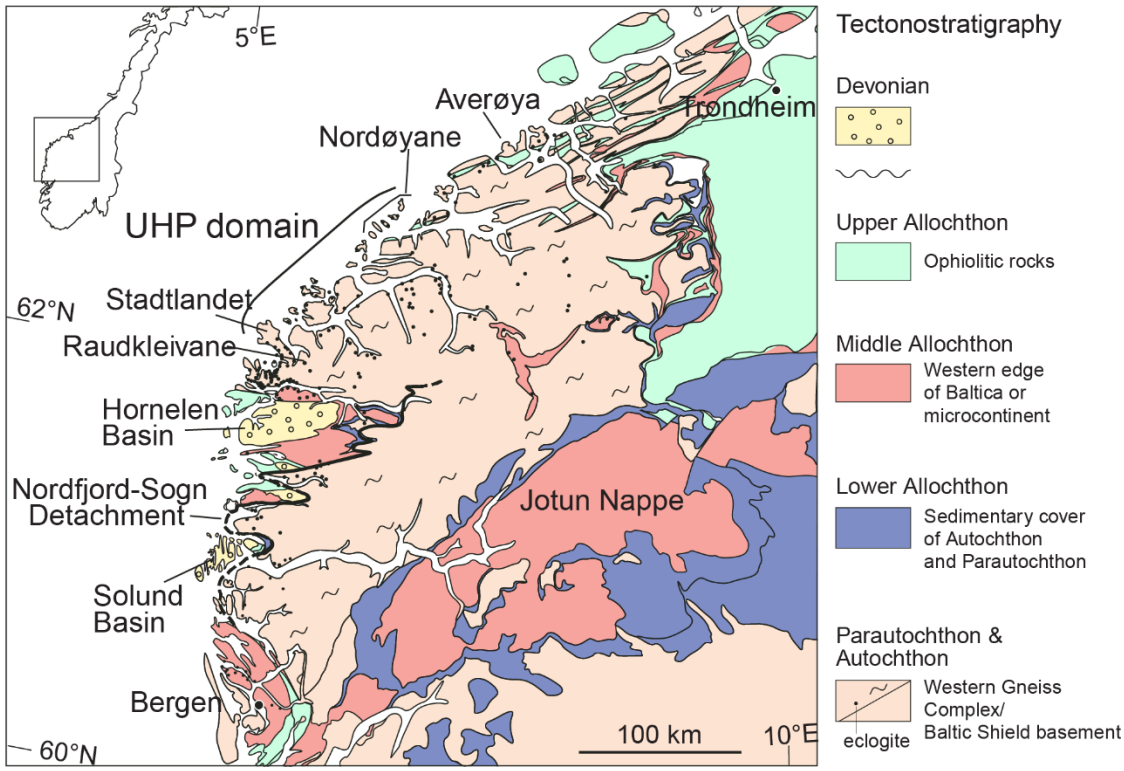

Figure 1.1: Tectonostratigraphy of south-western Norway, Western Gneiss Complex in pale pink. UHP domains to the north. Modified from Walsh, Hacker, Gans, Grove, and Gehrels (2007)

The WGC formed during the c. 430–400 Ma Scandian Phase of the Caledonian Orogeny that was driven by the westwards under-thrusting and subsequent collision of Baltica (mostly present-day Europe) with Laurentia (mostly present-day Greenland & North America). This phase of the Caledonian Orogeny resulted in the emplacement of nappe stacks of allochthonous (Laurentian-derived) material on the Precambrian crystalline basement of Baltica (Andersen & Andresen, 1994; Milnes, Wennberg, Skar, & Koestler, 1997; Roberts, 2003; Roberts & Gee, 1985; Tucker et al., 2004). Segments of the WGC were subducted to depths in excess of 140–150 km (Hacker et al., 2010; Krogh Ravna & Terry, 2004), which resulted in the formation of coesite-bearing eclogites (Smith, 1984) and microdiamond-

bearing gneisses (Dobrzhinetskaya et al., 1995), a type of metamorphism referred to as ultrahigh-pressure (UHP) metamorphism, during which subducted material reached minimum pressures above the quartz–coesite transition (28–29 kbar). These (U)HP rocks represent the returned remnants of deeply subducted continental lithosphere that are important in preserving a record of a wide range of subduction and exhumation related processes including material cycling, interactions with H_2O and other volatiles.

DISTRUBUTION OF (U)HP METAMORPHISM

Ultrahigh-pressure terranes first appear in the metamorphic rock record during the Cryogenian (Figure 1.2; ~655 Ma; Brown & Johnson, 2018; John & Schenk, 2003; John, Schenk, Mezger, & Tembo, 2004) and UHP metamorphism is inferred to still be occurring today, for example in Papua New Guinea (Baldwin, Webb, & Monteleone, 2008; Brown & Johnson, 2018; Zirakparvar, Baldwin, & Vervoort, 2011).

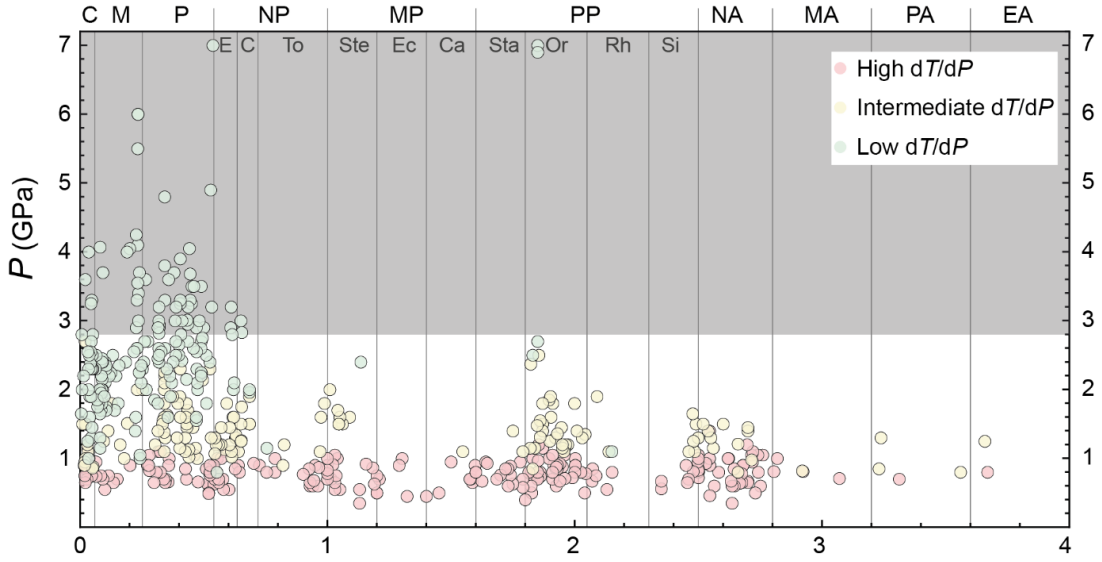

Figure 1.2: Metamorphic pressure vs age for 456 localities from Brown and Johnson (2018), grey box represents quartz to coesite UHP transition. Note near zero UHP metamorphism prior to the Cryogenian (720 Ma).

Occurrences of UHP rocks are spatially associated with late Neoproterozoic and Phanerozoic orogenic belts and are interpreted to record the deep subduction of continental crust (Figure 1.3; Burov et al., 2014a; Burov, Francois, Yamato, & Wolf, 2014b; Ernst & Liou, 2008; J. G. Liou, Ernst, Zhang, Tsujimori, & Jahn, 2009).

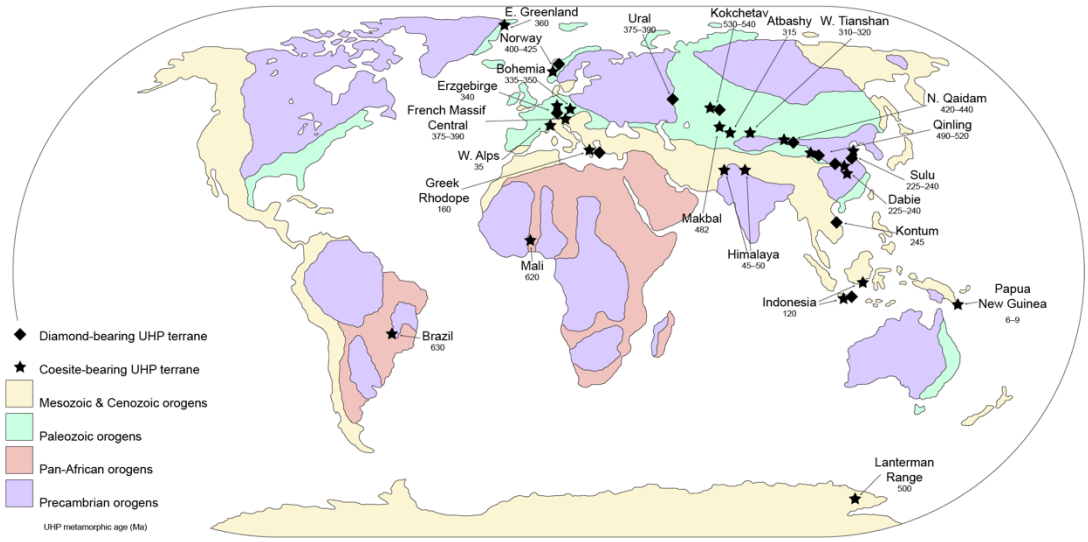

Figure 1.3: Distribution of coesite and diamond bearing UHP terranes, UHP metamorphic age (Ma) listed below locality, adapted from Burov et al. (2014a); J. G. Liou et al. (2009).

The occurrence of UHP rocks has been suggested to represent the transition from a shallow hot-subduction tectonic regime, identifiable as paired low d*T*/d*P* and high d*T*/d*P* metamorphism, that operated from the Neoarchean until the late Mesoproterozoic, before transitioning to modern-style cold, deep subduction that characterises the Phanerozoic Earth (Brown & Johnson, 2018; Holder, Viete, Brown, & Johnson, 2019).

MECHANISMS OF EXHUMATION

How UHP rocks are exhumed from depths in excess of 100–150 km remains a fundamental geodynamic question. The mechanism has been the focus of considerable debate since the discovery of coesite (Chopin, 1984; Smith, 1984) and subsequently microdiamond (Dobrzhinetskaya et al., 1995; Sobolev & Shatsky, 1990) within subducted rocks. One physical parameter that is generally considered to exert a significant control on the exhumation of continental rocks is the positive buoyancy of continental crust relative to upper mantle and oceanic crust, even under eclogite facies conditions (Burov et al., 2014b; Hacker & Gerya, 2013; Hacker, Gerya, & Gilotti, 2013).

More recently there has been an increased awareness of the potential of non-lithostatic drivers (i.e., tectonic overpressure) for the formation of UHP terranes (Mancktelow, 1995, 2008; Petrini & Podladchikov, 2000; Schmalholz, Duretz, Schenker, & Podladchikov, 2014; Schmalholz & Podladchikov, 2013). These studies suggest that the high-pressures recorded by these rocks may reflect non-lithostatic (non-burial) processes, or ‘tectonic overpressure’, such that pressures may be higher by a factor of two or more. Thus, UHP rocks may never have reached depths of 100–150 km or more. Despite this, full scale 3D thermomechanical modelling of subduction (Li, Gerya, & Burg, 2010; Toussaint, Burov, & Jolivet, 2004) do not

reproduce this non-lithostatic pressure (Burov et al., 2014a). Models invoking non-lithostatic pressure also do not explain the similarities in *P–T* gradient (~8–10 ˚C/km) for both oceanic and continental UHP rocks from similar settings (Agard, Jolivet, & Goffe, 2001), nor why UHP terranes are only found in areas where dense, subducted oceanic slab is imaged (by seismic tomography) at depth (Burov et al., 2014a). Despite it being unlikely that an entire terrane may have experienced regional scale tectonic overpressure to produce U(HP) conditions there are isoloated examples within the WGC that exist outside the regional pressure gradient, with tectonic overpressure proposed to explain these pertubations (Cutts, Smit, & Vrijmoed, 2019b; Vrijmoed, Podladchikov, Andersen, & Hartz, 2009). As such, this thesis will consider a traditional pressure–depth equivalence, whilst being mindful of this developing area of research.

There are currently six primary mechanisms proposed to explain the exhumation of continental UHP rocks (Figure 1.4), with each attempting to explain a set of geological observations in a variety of differing terranes. These are: (1) large scale crustal stacking (Chemenda, Burg, & Mattauer, 2000; Chemenda, Mattauer, Malavieille, & Bokun, 1995; Sizova, Gerya, & Brown, 2012); (2) subduction channel flow (Beaumont, Jamieson, Butler, & Warren, 2009; Gerya, Perchuk, & Burg, 2008; Sizova et al., 2012; Warren, Beaumont, & Jamieson, 2008a, 2008b); (3) eduction (Andersen, Jamtveit, Dewey, & Swensson, 1991; Brueckner & Van Roermund, 2004; Duretz, Gerya, Kaus, & Andersen, 2012); (4) trans-mantle diapirs (Gerya & Stöckhert, 2006; Hacker et al., 2005; Little et al., 2011; Sizova et al., 2012; Yin et al., 2007); (5) microplate motion (Hacker & Gerya, 2013; Hacker et al., 2000; Webb, Baldwin, Little, & Fitzgerald, 2008), and; (6) slab rollback (Sizova, Hauzenberger, Fritz, Faryad, & Gerya, 2019).

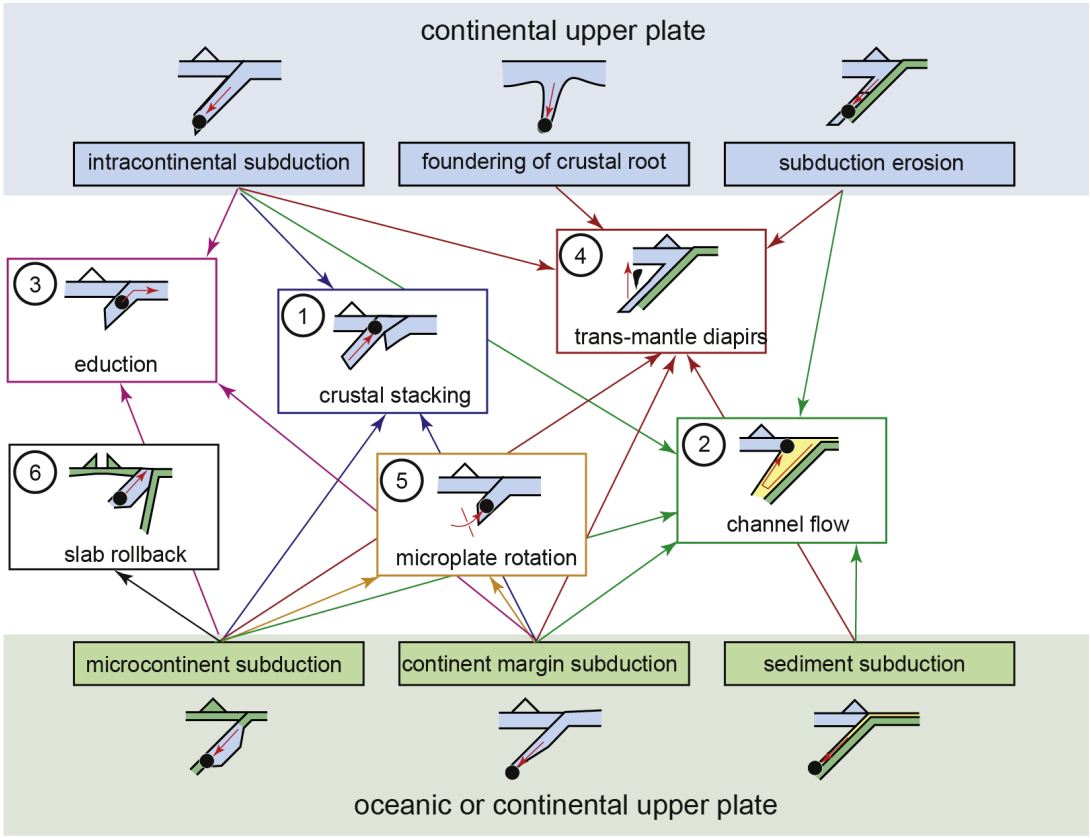

Figure 1.4: Summary of differing mechanisms and associated settings to explain the exhumation of ultra-high-pressure rock (Hacker et al. 2013). See above paragraph for further references discussing each model.

Despite these different mechanisms, terranes can be ascribed to one of two endmembers, forming during differing stages of subduction. (1) Smaller UHP terranes with shorter residence times (<10 Ma) in the subduction channel likely formed early during orogeny with the orogen terminating before large volumes of continental material enter the subduction zone (Kylander-Clark, Hacker, & Mattinson, 2012). (2) Larger continental terranes will have greater residence times (10–30 Ma), and are likely to have formed during a more protracted orogeny, allowing larger volumes of continental material to enter the subduction zone (Kylander-Clark et al., 2012). See Table 1.1 for a detailed summary of worldwide examples.

Terrane	*Minimum volume*		Peak UHP age (Ma)	Lower-crustal age (Ma)	Mid–upper crustal age (Ma)	Subduction duration (Myr)	Exhumation duration (Myr)	Total duration (Myr)
	Area (km^2)	Thickness (km)						
Lago Cignana[1]	< 500 (2)	0.3	40.6 ± 2.6	n/d	38 ± 2	~ 8	~ 2	~ 10
Kaghan Valley[2]	< 1000	< 5	46.4 ± 0.1	n/d	44.1 ± 1.0	7–9	~ 2	9–11
Papua New Guinea[3]	4000	n/d	7.9 ± 1.9	~ 3.5	~ 1.5	n/d	~ 4	> 4
Tso Morari[4]	5000	< 15	53.3 ± 0.7	47 ± 11	48 ± 2	n/d	~ 5	> 5
Dora Maira[5]	500 (50)	1	35.4 ± 2.7	32.9 ± 0.9	31.8 ± 0.5	n/d	~ 4	> 4
Erzgebirge[6]	2500 (1)	3	336.8 ± 2.8	330.2 ± 5.8	340–330	n/d	< 7	n/d
Kokchetav[7]	< 1500	< 2	~ 533	528 ± 8	~ 529	n/d	~ 6	> 6
Greenland[8]	40,000 (> 40)	> 5	364 ± 8	342 ± 6	~ 329	n/d	~ 35	> 35
Qaidam[9]	25,000	n/d	446–423	n/d	401.5 ± 1.6	> 13	> 21	~ 58
Western Gneiss Region[10]	30,000 (5,000)	> 15	405–400	~ 390	385–375	> 20	> 15	> 35
Dabie–Sulu[11]	30,000 (10,000)	> 10	245–222	222–210	200–180	> 12	> 20	~ 45

Table 1.1: Summary table of worldwide UHP terranes from Kylander-Clark et al., (2012). 1) Amato, Johnson, Baumgartner, and Beard (1999); Lapen et al. (2003); 2) Kaneko et al. (2003); Parrish, Gough, Searle, and Waters (2006); 3) Monteleone et al. (2007); 4) de Sigoyer et al. (2000); Leech, Singh, and Jain (2007); 5) Gebauer, Schertl, Brix, and Schreyer (1997); Henry, Michard, and Chopin (1993); Rubatto and Hermann (2001); 6) Kröner and Willner (1998); Massonne, Kennedy, Nasdala, and Theye (2007); Werner and Lippolt (2000); 7) Hacker, Calvert, Zhang, Ernst, and Liou (2003b); Hermann, Rubatto, Korsakov, and Shatsky (2001); Kaneko et al. (2000); Shatsky et al. (1999); Yamamoto, Ishikawa, Anma, and Kaneko (2000); 8) Gilotti, Nutman, and Brueckner (2004); Gilotti and Ravna (2002); McClelland, Power, Gilotti, Mazdab, and Wopenka (2006); 9) Mattinson, Wooden, Liou, Bird, and Wu (2006); Song et al. (2006); 10) Kylander-Clark et al. (2009); Kylander-Clark et al. (2007); Kylander-Clark et al. (2008); Root et al. (2005); 11) Hacker et al. (2000); Hacker, Wallis, Ratschbacher, Grove, and Gehrels (2006).

The driver of this is likely related to differing rates of subduction and/or proportions of subducting oceanic to continental crust and mantle lithosphere (Figure 1.5; Kylander-Clark et al., 2012). Initiation of subduction leads to thinned continental crust, such as a microcontinent, and the subduction of proportionally more dense oceanic crust, leading to rapid slab subduction at a steep angle (Figure 1.5), if subduction terminates here a small U(HP) terrane may be produced. As subduction continues a transition to thicker continental crust occurs,

leading to a greater buoyancy in the subducting plate, which slows and flattens subduction, producing a larger U(HP) terrane (Kylander-Clark et al., 2012).

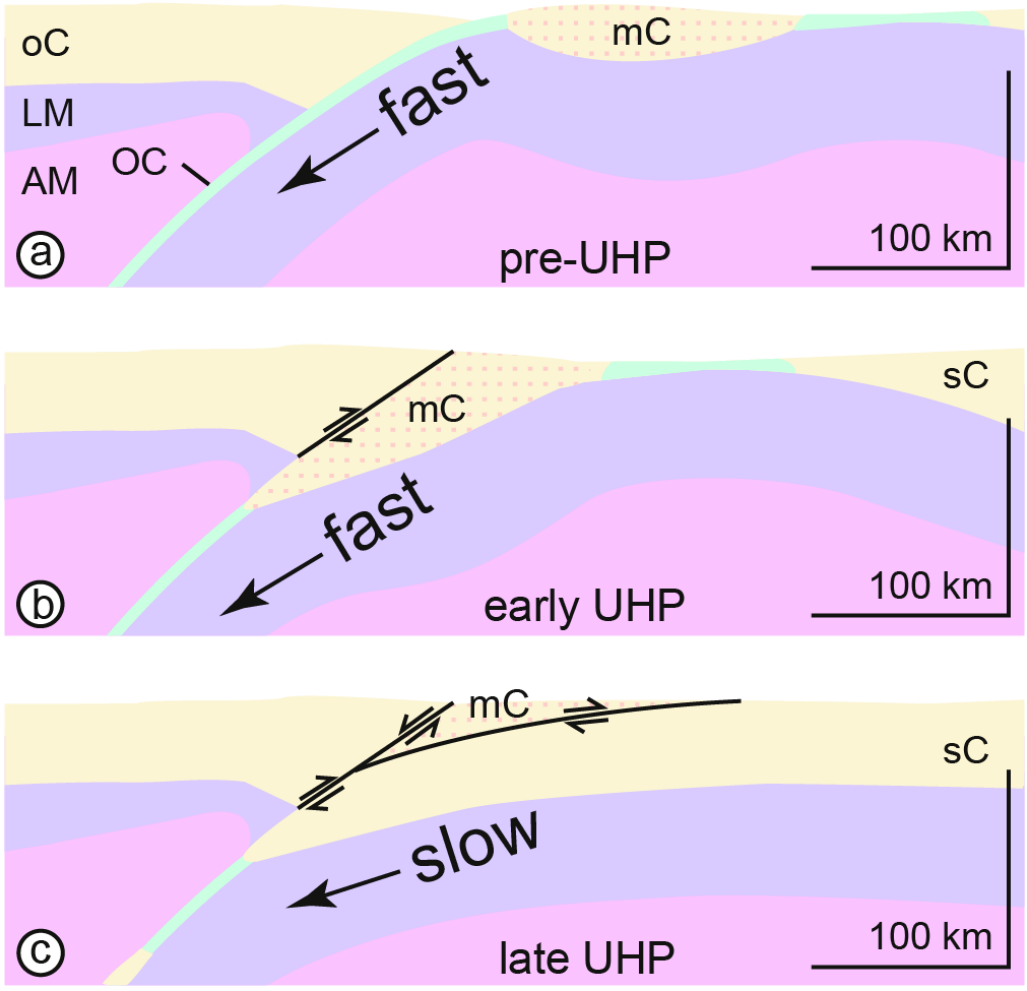

Figure 1.5: Two differing types of UHP terrane formation, small terrane (e.g. microcontinent) enters subduction zone at (b) while with continued orogeny continental plate enters at (c). oC = overriding continent; sC = subducted continent; OC = oceanic crust; LM = lithospheric mantle; AM = asthenospheric mantle. Modified from Kylander-Clark et al. (2012)

EXHUMATION MECHANSIMS FOR WESTERN GNEISS REGION

The Scandinavian Caledonides are widely accepted to represent an example of the eduction model of exhumation, with subducted continental crust exhumed by "reversing" out of the subduction zone (e.g. Andersen et al., 1991; Brueckner & Van Roermund, 2004; Duretz et al., 2012; Hacker et al., 2013). The acceptance of the eduction model is underpinned by three primary datasets: (1) A continuous metamorphic field gradient from amphibolite facies in the east to eclogite then UHP eclogite in the west (Hacker et al., 2010; Young, Hacker, Andersen, & Corfu, 2007). (2) The smooth and continuous transition from older $^{40}Ar/^{39}Ar$ white mica dates in the east to younger dates in the west (Walsh, Hacker, Gans, Wong, & Andersen, 2013;

Young, Hacker, Andersen, & Gans, 2011). (3) Apparent lack of large-scale shear zones segmenting the WGC. This, coupled with late stage extension, resulted in the formation of large-scale extensional detachments within the lower crust (e.g. Nordfjord-Sogn detachment; Hacker et al., 2003a), although alternative models have been proposed. Cutts, Smit, Kooijman, and Schmitt (2019a); Walsh and Hacker (2004) propose that a crustal stacking model may be more appropriate for the WGC, which is inferred to have exhumed under relatively flat slab conditions, although the lack of any basal thrust is problematic, along with the transect of Cutts et al. (2019a) being sub-perpendicular to the $^{40}Ar/^{39}Ar$ age contours of Walsh et al. (2013) and shear fabrics of Johnston, Hacker, and Ducea (2007b). Structural data (Young, 2017) indicates that two blocks of upper Baltic crust delaminated during Scandian subduction and stalled at different crustal levels before being exhumed. Thus, despite apparently consistent *P–T* conditions across the WGC, the structure may be more fragmented than a simple eduction model implies.

Ductile flow within metamorphic core complexes has also been inferred to have aided exhumation and juxtaposition of parts of the WGC (e.g.; Wiest, Osmundsen, Jacobs, & Fossen, 2019). The Nordfjord–Sogn detachment is one such structure and represents a large-scale Caledonian brittle-ductile extensional detachment that extends for ~100 km in western Norway (Eide, Torsvik, & Andersen, 1997; Norton, 1987). Movement within the Nordfjord–Sogn detachment zone at c. 400 Ma is inferred to have played an integral part in the exhumation of rocks within southwestern Norway during the waning stages of the Scandian Phase of the Caledonian Orogeny (Eide et al., 1997; Hacker et al., 2003a; Johnston, Hacker, & Andersen, 2007a; Norton, 1987).

AIMS & OBJECTIVES

The main aim of this thesis is to produce a pressure–temperature–time (*P–T–t)* history for rocks above and below the Nordfjord–Sogn detachment zone, assessing the influence of this structure on the exhumation of the surrounding rocks. These constraints can then be incorporated into a tectonic model for the evolution of the region, which can be compared with existing regional structural, metamorphic and geochronological data and tectonic models for the Scandinavian Caledonides and the Caledonian Orogeny. A key component of this thesis will be the application of internally-consistent phase equilibrium modelling (*P–T* pseudosections) to evaluate the *P–T* conditions and paths experienced by rocks of the WGC and overlying Hyllestad Complex. Previously only one study of the WGC (Martin & Duchêne, 2015) have taken this approach and the internally consistent results generated through the application of this technique has the potential to robustly identify gaps on breaks in the thermobarometric record of the WGC.

This broader aim is divided into several small objectives. The chapters that satisfy these objectives are in (*parentheses*).

1. Investigate the *P–T–t* record of eclogites bodies that occur in the southern portion of the WGC, within the footwall of the Nordfjord–Sogn detachment zone *(Chapter 2)*.
2. Investigate the aluminous schists that crop out within the hanging wall of the Nordfjord–Sogn detachment zone, examining their temporal, pressure, thermal and structural history in an attempt to observe the effect of the detachment on the surrounding rocks. *(Chapter 3)*.
3. Investigate role the Nordfjord–Sogn detachment plays in the exhumation of these rocks (C*hapters 2, 3 & 4*).

THESIS STRUCTURE

This thesis opens with an introduction that addresses the rationale and objectives for this study along with additional background information and ends with a conclusion that summarises the major outcomes of the research. A separate literature review is not presented, as individual chapters along with the introduction incorporate the relevant background information and place the research within a wider context. Chapters are presented in a logical order to account for the spatial and temporal evolution of the Nordfjord–Sogn detachment.

Chapter 1, Introduction

This chapter outlines the geological framework in which high and ultra-high-pressure rocks exists in. A brief summary of the geology of the WGC and its broader context within the Scandinavian Caledonides is also included.

Chapter 2, Constraining the onset of eclogite facies metamorphism in the southern Western Gneiss Complex, Norway

This chapter aims to produce *P–T–t c*onstraints on prograde and peak eclogite facies metamorphism on an understudied segment of the south-western WGC that sits within the footwall of the Nordfjord–Sogn detachment.

Chapter 3, Deviations from the norm: A case for deformation enhanced heating during exhumation of the Western Gneiss Complex, Norway.

This chapter aims to investigate the exhumation history of rocks within the hanging wall of the Nordfjord–Sogn detachment, placing constraints on their pressure and thermal history as well as temporal and spatial relationship to the Nordfjord–Sogn detachment.

Chapter 4, Thesis conclusions

This chapter integrates work from within Chapter 2 and Chapter 3 to propose a *P–T–t* history for rocks surrounding the Nordfjord–Sogn detachment.

2. CONDITIONS OF ECLOGITE FACIES METAMORPHISM IN THE SOUTHERN WESTERN GNEISS COMPLEX, NORWAY

1. | INTRODUCTION

Unravelling the timing and conditions of prograde and peak metamorphism within the (ultra)high-pressure Western Gneiss Complex (WGC) has been a goal of many studies dating back to the 1970's, which advanced some of the first tectonic models attempting to explain the complex tectonostratigraphy of the Caledonides (Bockelie & Nystuen, 1985; Gee, 1975, 1980; Hossack, Garton, & Nickelsen, 1985; Roberts & Gee, 1985; Stephens & Gee, 1985). The development of isotopic techniques, including Sm–Nd geochronology of garnet, allowed the first temporal constraints on the timing of peak metamorphism within the Caledonides (Griffin & Brueckner, 1980; Mearns, 1986; Mørk & Mearns, 1986). The identification of coesite within clinopyroxene bearing eclogites by Smith (1984) and microdiamond within the quartzofeldspathic gneiss by Dobrzhinetskaya et al. (1995) resulted in the recognition that large volumes of crust can be subducted and returned from depths exceeding 100 km (Andersen et al., 1991; Hacker et al., 2010). Since then, and due to its size, relative coherence during subduction and exhumation, good exposure and natural beauty, a significant number of studies have been undertaken in the region. Thus the WGC is considered a type-locality for investigating the processes associated with deep subduction and exhumation of continental crust.

Most previous studies have focused on the UHP domains in the northern WGC and (SE) back along the paleo-subduction direction of Baltica (Andersen et al., 1991; Carswell, van Roermund, & Wiggers de Vries, 2006; Cutts & Smit, 2018; DesOrmeau et al., 2015; Engvik & Andersen, 2000; Hacker et al., 2010; Hacker et al., 2015; Kylander-Clark et al., 2009; Kylander-Clark et al., 2008; Labrousse et al., 2004; Mørk & Mearns, 1986; Young, 2017). By contrast, the southwestern part of the terrane has received relatively little attention, probably due to the lack of UHP rocks (Young, 2017). In the northern WGC the principal constraints on peak *P–T* conditions during the Scandian phase of Caledonian orogenesis are derived mainly from conventional thermobarometry, including garnet–clinopyroxene Mg–Fe exchange thermometry and jadeite–diopside and phengite barometry (Carswell, Brueckner, Cuthbert, Mehta, & O'Brien, 2003a; Cuthbert, Carswell, Krogh-Ravna, & Wain, 2000; Cutts et al., 2019b; Krogh Ravna & Terry, 2004; Root et al., 2005). There is a scarcity of phase equilibrium studies from the entire WGC, with only two studies to-date (Martin & Duchêne, 2015; Peterman, Hacker, & Baxter, 2009) presenting phase equilibria work, though neither focus on constraining peak conditions of metamorphism.

The earliest constraints on the timing of eclogite facies metamorphism in the northern WGC are from Sm–Nd garnet geochronology (c. 430–410 Ma; e.g. Griffin & Brueckner, 1980; Jamtveit, Carswell, & Mearns, 1991; Mearns, 1986; Mørk & Mearns, 1986). More recently

Lu–Hf (c. 420–405 Ma; Cutts & Smit, 2018; Martin et al., 2010) or coupled Lu–Hf & Sm–Nd garnet geochronology has been applied (c. 419–410 Ma & c. 402–384 Ma; Kylander-Clark et al., 2009; Kylander-Clark et al., 2007). Aditionally a large quantity of TIMS U–Pb zircon data from within eclogites (c. 420–400 Ma; Carswell, Tucker, O'Brien, & Krogh, 2003b; Krogh, Kamo, Robinson, Terry, & Kwok, 2011; Root et al., 2005; Young et al., 2007) aditionally constraining the timing of U(HP) metamorphism. LA–ICP–MS U–Pb monazite (e.g. Holder, Hacker, Kylander-Clark, & Cottle, 2015) also provides aditional contraints on the U(HP) peak.

By contrast, in the southwestern region of the Western Gneiss Complex such thermobarometry data is sparse, with only a few instances of conventional thermobarometers being applied (e.g. Engvik & Andersen, 2000; Hacker et al., 2003a; Johnston et al., 2007b; Labrousse et al., 2004). As with the northern WGC there is a lack of multi-outcrop scale phase equilibria modelling studies, with just one to to-date on an eclogite body at Vårdalsneset (Martin & Duchêne, 2015) that focused on the conditions of rehydration rather than constraining peak *P–T*.

This study aims to derive constraints on the *P–T* conditions through the application of phase equilibria modelling. In addition, garnet Lu–Hf geochronology from a selection of the modelled rocks will be collected. The integration of these datasets will be a first-order test of the model of a continuous pressure and thermal gradient existing across the Western Gneiss Complex (Andersen et al., 1991; Carswell et al., 2006; Cuthbert et al., 2000; Hacker et al., 2010). In addition, the *P–T* conditions experienced by the eclogite bodies constrain the conditions of experienced by the footwall of the Nordfjord–Sogn detachment zone and will be combined with the datasets in Chapter 3 to investigate the evolution of the NSDZ.

2. | REGIONAL GEOLOGY

2.1 | Geology of the southern WGC

The rocks of the southern WGC are dominated by amphibolite facies quartzo-feldspathic gneisses (Figure 2.1; Engvik & Andersen, 2000; Engvik, Austrheim, & Erambert, 2001; Foreman, Andersen, & Wheeler, 2005), derived from rocks of Gothian (c. 1750–1500 Ma; Austrheim, Corfu, Bryhni, & Andersen, 2003; Skår, 2000; Skår & Pedersen, 2003) and Sveconorwegian (c. 1140–960 Ma; Bingen, Andersson, Soderlund, & Moller, 2008a; Bingen, Nordgulen, & Viola, 2008b; Skår, 2000) origin. Gothian protoliths represent a wide variety of compositions with felsic, intermediate, mafic and ultramafic plutonic rocks and minor amounts of various supracrustal rock, forming over 80% of current WGC exposure (Austrheim et al., 2003; Bryhni, 1989; Skår, 2000; Skår & Pedersen, 2003). The remaining 20% of the WGC consists of rocks of a Sveconorwegian protolith, limited in occurrence to only the southern portion (Tucker, Krogh, & Råheim, 1990), consisting of predominantly intermediate to felsic small dykes to large syn–post kinematic intrusions (Skår, 2000; Skår & Pedersen, 2003).

Fabrics preserved within the quartzo-feldspathic gneisses are predominantly Sveconorwegian in age, with up to four deformation phases found within the Sognfjord region (Skår & Pedersen, 2003).

Within the volumetrically dominant quartzo-feldspathic gneisses eclogite occur as pods/lenses or large bodies range in sizes from cm's to km's making up less than c. 1 vol.% (Root et al., 2005) formed through deep subduction (> 70 km) during Scandian metamorphism (430–400 Ma; Gee, 1975; Roberts & Gee, 1985). Unlike the eclogite bodies of the northern WGC, no evidence of UHP metamorphism has been found south of the Nordfjord UHP domain.

Overlying the WGC are a series of allochthonous nappes, emplaced along major crustal structures (e.g. Jotun Main Basal Thrust) onto the Baltican basement during Baltic–Laurentian collision. These nappes are of mixed provenance, consisting of crustal material with Laurentian affinity (Uppermost Allochthon); outboard oceanic terranes (Upper Allochthon); portions of the overriding Laurentian plate along with the remnants of the hyperextended Baltican-continental margin (Middle and Lower Allochthons; Andersen & Andresen, 1994; Milnes et al., 1997; Roberts, 2003; Roberts & Gee, 1985; Tucker et al., 2004).

Estimates of peak *P–T* conditions within the southern segment of the WGC are relatively sparse. These range from 677 ± 21˚C at 16 ± 2 kbar, and 691 ± 20˚C 15 ± 1.5 kbar (Engvik & Andersen, 2000) to 615 ± 22˚C 22.7 kbar as a via the garnet-clinopyroxene Mg-Fe exchange thermometer, phengite barometer and jadeite–diopside exchange barometer. A very small number of *P–T* estimates obtained by phase equilibria modelling exist, with just one study from the Vårdalsneset body, returning 590–720 °C, 15–25 kbar (Martin & Duchêne, 2015). Limited Lu–Hf garnet geochronology exists within the southern WGC, ages from the Vollstein eclogite body (sample K5622A2) of Kylander-Clark et al. (2009) return ages of 410 ± 3.1 Ma while garnet–whole-rock isochrons from the Vårdalsneset body (samples NOG12 & NOG13) of Martin et al. (2010) return ages of 409 ± 12 Ma & 403 ± 13 Ma respectively.

Eclogites display varying degrees of retrogression and amphibolite facies overprinting (Engvik & Andersen, 2000; Engvik et al., 2001; Foreman et al., 2005; Milnes et al., 1997; Walsh et al., 2007). Overprinting varies from minor deformation to near-complete destruction of early Scandian fabrics, replaced with E and W plunging lineations, with N and S dipping foliations folded isoclinally around E and W plunging hinges (Root et al., 2005; Wiest et al., 2019; Young, 2017). Various geochronometers record this overprinting including; U–Pb monazite (410–390 Ma; Hacker et al., 2015; Holder et al., 2015); U–Pb titanite (405–385 Ma; Kylander-Clark et al., 2008; Spencer et al., 2013); U–Pb rutile (400–375 Ma; Butler et al., 2018; Cutts et al., 2019a; Kylander-Clark et al., 2008). Local scale retrogression of eclogite along fluid infiltrated shear zones (Martin & Duchêne, 2015), along with heavily mylonised or tectonic

eclogite within bodies proximal to the Nordfjord–Sogn detachment zone are also associated with this amphibolite facies overprinting.

Separating the para-autochthonous Western Gneiss Complex from the overlying allochthons and Devonian supradetachment basins is the Nordfjord–Sogn detachment zone (Figure 2.1), large-scale extensional brittle-ductile shear zone, over 100 km in length, end-Caledonian in age and preserves greenschist-amphibolite facies overprinting and assemblages (Eide et al., 1997; Labrousse et al., 2004; Norton, 1986, 1987). Surrounding the detachment surface is a 3–5 km thick highly deformed layer of brittle-ductile mylonites (Andersen & Andresen, 1994; Andersen & Jamtveit, 1990; Hacker et al., 2003a).

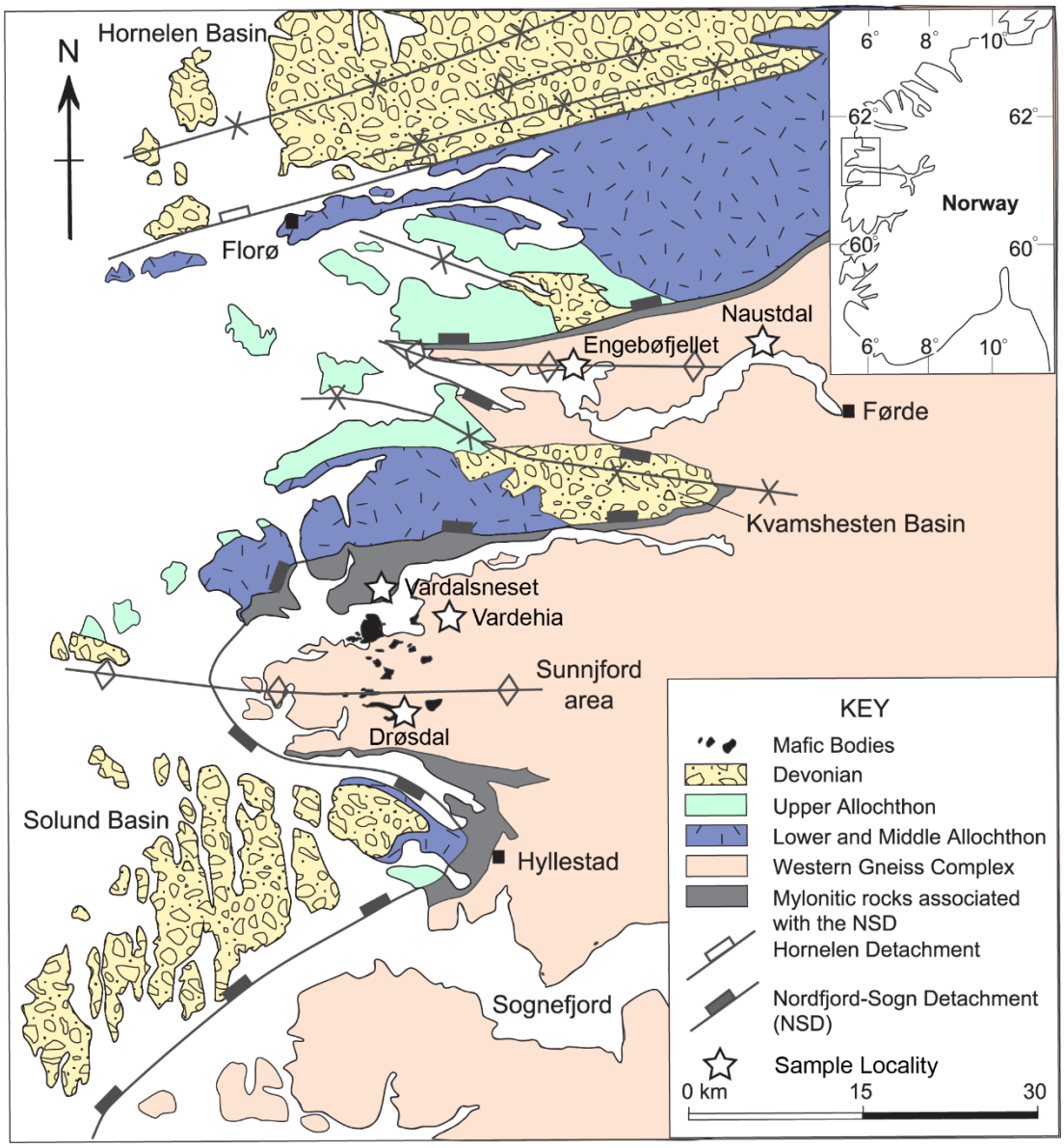

Figure 2.1: Simplified geological map of the Dalsfjorden and Førdefjorden area. Stars indicate sampled localities of this study. Modified from Foreman et al. (2005)

2.2 | Tectonic and metamorphic events

The Western Gneiss Complex (WGC) experienced the Sveconorweigian orogeny, a pervasive deformational and metamorphic event at c. 1140–960 Ma, (Bingen et al., 2008a; Bingen et al., 2008b; Roberts & Gee, 1985). The imprint of this event defines the majority of outcrop scale features within the southern WGC (Roberts, 2003). Despite the dominance of the Sveconorwegian fabric, the present tectonostratigraphy of the Scandinavian Caledonides was imposed during the 430–400 Ma Scandian Orogeny during the collision and subsequent under thrusting of Baltica beneath Laurentia (Gee, 1975; Roberts & Gee, 1985). See Roberts (2003) and refs. therein for a detailed discussion of pre-Scandian Caledonian events. The absence of magmatism with oceanic affinity within the Caledonides after c. 430 Ma suggests that continent-continent collision initiated around this time, with the consumption of the Iapetus Ocean (Andersen & Jamtveit, 1990; Corfu et al., 2006; Slagstad & Kirkland, 2018; Torsvik & Cocks, 2005).

During collision nappe stacks consisting of; crustal material with Laurentian provenance (Uppermost Allochthon); outboard oceanic terranes (Upper Allochthon); portions of the overriding Laurentian plate along with the remnants of the hyperextended Baltican-continental margin (Middle and Lower Allochthons) were thrust on to the gneisses of the WGC that form the basement of the Baltica (Andersen & Andresen, 1994; Milnes et al., 1997; Roberts, 2003; Roberts & Gee, 1985; Tucker et al., 2004). The emplacement occurred along major crustal structures (e.g. Jotun Main Basal Thrust) onto the Precambrian crystalline basement and is thought to have been terminated by c. 415 Ma (Andersen & Andresen, 1994; Milnes et al., 1997; Roberts, 2003; Roberts & Gee, 1985; Tucker et al., 2004).

As collision was ongoing the continued subduction of the Baltican margin, dominated by the crustal lithologies that comprise the WGC were buried to depths of 80–120 km. These extreme depths reached by some Baltic segments, led to the development of UHP assemblages that include coesite-bearing eclogites (Smith, 1984), along with rare microdiamond within the volumetrically dominant quartzofeldspathic gneisses (Dobrzhinetskaya et al., 1995). Geochronology from the deeply subducted rocks suggest that this occurred at around 410 to 400 Ma (Hacker et al., 2010; Krogh et al., 2011; Kylander-Clark et al., 2008; Terry, Robinson, Hamilton, & Jercinovic, 2000). Compilation of regional thermometry and barometry has been interpreted to reflect continuous pressure temperature gradient present across Western Gneiss Complex, indicative of the coherent nature of the Western Gneiss Complex during subduction and subsequent exhumation that experienced some N-S compressional warping (Andersen et al., 1991; Carswell et al., 2006; Cuthbert et al., 2000; Hacker et al., 2010).

Following deep burial, the WGC was rapidly exhumed along with the development of a series of large-scale crustal shear zones e.g., Nordfjord–Sogn Detachment (Hacker et al., 2003a; Johnston et al., 2007a; Root et al., 2005) to mid-crustal levels. Residence at this level and the addition of fluids led to the development of a widespread amphibolite facies overprint. (Cuthbert et al., 2000; Engvik & Andersen, 2000; Johnston et al., 2007a; Johnston et al., 2007b; Martin & Duchêne, 2015). Recent work by Cutts et al. (2019a) suggest a two stage exhumation model may be appropriate with the WGC reaching near flat slab conditions.

3. | METHODS

3.1 | Sample preparation for LA-ICP-MS & garnet geochronology

Representative samples of approximately 1000g were disintegrated by SELFRAG high voltage electrodynamic disaggregation at the John de Laeter Centre, Curtin University. Disintegrated samples were then fed through a multi-pass routine using a Franz Electromagnetic Separator to produce different magnetic fractions, primarily to separate garnet from the less magnetic sample volume consisting of predominantly omphacite, phengite and quartz. Clean, (relatively) inclusion and fracture free garnet was hand-picked from the separate that contained all garnet to avoid magnetic biasing and mounted in epoxy, taking care to orient elongated grains parallel to the mount surface. Garnet grains were then carefully ground to expose their geometric cores and subsequently polished prior to analysis.

3.2 | Whole rock geochemistry for phase equilibria modelling

Samples for whole rock geochemistry were cut from rock directly adjacent to thin section blocks to provide the best representation of thin section composition. The bulk major element compositions of the samples were measured by x-ray fluorescence (XRF) at Franklin and Marshall College, Pennsylvania using a PANalytical 2404 X-ray fluorescence vacuum spectrometer by fusing 0.4000g of sample with 3.6000g of lithium tetraborate. Major oxides; SiO_2, Al_2O_3, CaO, K_2O, P_2O_5, TiO_2, total iron (Fe_2O_3T), MnO, Na_2O and MgO along with selected trace elements were measured by XRF. FeO/Fe_2O_3 was measured by titration, while H_2O was measured through loss on ignition (LOI) by heating the sample to 900–950˚C for 60 minutes. **Error! Reference source not found.** shows whole rock oxide of each sample expressed as wt%.

3.3 | EMPA analysis

Electron microprobe analysis was conducted to determine quantitative mineral compositions and obtain elemental maps for Fe, Al, Ca, Mg and Mn of garnet at Adelaide Microscopy, University of Adelaide using a Cameca SXFive Electron Microprobe equipped with 5 tuneable wavelength-dispersive spectrometers running Probe for EPMA software. A 15 KeV acceleration voltage, 20 nA beam current with 2 μm defocused beam size was used for each

mineral composition analysis, at an average of 90 seconds per analysis. The following suite of elements was acquired: Cl, Ca, K, Ba, F, Ti, P, Na, Si, Mg, Al, Fe, Mn, Cr, Zn, and Ni, oxygen was calculated by stoichiometry, assuming that all Fe was Fe^{2+}. Calibration was to a wide range of synthetic and natural standards within Probe for EPMA software, with the software used to convert CPS to wt%. A full list of natural and synthetic standards used for data standardisation and more detailed methodology is presented in Appendix B. Elemental maps were acquired with a 15 KeV acceleration voltage, 200 nA beam current with a defocused beam size varying (2–5 μm) between samples. Data is presented in Supplementary Data 1.

3.4 | Laser Ablation inductively coupled plasma mass spectrometry (LA–ICP–MS)

Trace-element geochemistry to characterise the REE zoning prior to garnet geochronology was obtained by LA-ICPMS within the GeoHistory Facility, John de Laeter Centre, Curtin University using a Resonetics S-155-LR 193nm ArF excimer laser ablation system coupled to an Agilent 8900 triple quadrupole ICPMS. The following elements ^{29}Si, ^{31}P, ^{43}Ca, ^{45}Sc, ^{49}Ti, ^{51}V, ^{52}Cr, ^{85}Rb, ^{88}Sr, ^{89}Y, ^{91}Zr, ^{139}La, ^{140}Ce, ^{141}Pr, ^{146}Nd, ^{147}Sm, ^{153}Eu, ^{157}Gd, ^{159}Tb, ^{163}Dy, ^{165}Ho, ^{166}Er, ^{169}Tm, ^{173}Yb, ^{175}Lu, ^{178}Hf, ^{232}Th, ^{238}U, each element was monitored for 0.35 seconds on the Agilent 8900 QQQ.

Analyses were conducted with a laser repetition rate of 5 hz with a spot size of 50 μm at 26% attenuation, leading to a fluence of ~2 J/cm^2. The following sequence of: two cleaning pulses, a long initial background collection of 30 s, followed by 10 s ablation, and 15 s of washout time was repeated for each analysis. Laser gas flow of 320 ml/min He, and 1.2 ml/min N were used with argon gas flow of ~1 L/min for the Agilent 8900 QQQ.

Analysis of garnet were conducted using 50 μm spots in a traverse from rim to rim, using a 55–60 μm centre-centre spacing between spots. Analyses per garnet ranged from n=13 to n=48 dependant on grain size.

Standards; NIST610, NIST612 and NIST614 (Jochum et al., 2011), BHVO, BCR (Jochum, Willbold, Raczek, Stoll, & Herwig, 2005) and TIG (Govindaraju, 1994) were inserted into the analysis run at 22 spot intervals. Standardisation of garnet time resolved series data within Iolite software (Paton, Hellstrom, Paul, Woodhead, & Hergt, 2011) using the TraceElements_SI DRS (Paton et al., 2011) was conducted by standardising against NIST610, using a value of 17 wt% for silica obtained via EMPA (see 3.3). QC of data was conducted by treating NIST612 as an unknown and standardising against NIST610, with all values for NIST612 falling within accepted error. Data is presented in Supplementary Data 2.

3.5 | Garnet geochronology

Lu–Hf garnet geochronology was conducted at the Radiogenic Isotope and Geochronology Laboratory at Washington State University, USA. Clean, inclusion and fracture free garnet was picked after SELFRAG processing (see 3.1) and separated into four 250 mg aliquots per-sample. Whole rock fractions (sans garnet) were powdered by hand using agate mill, with two 250 mg aliquots separated per sample.

Garnet aliquots and one fraction of whole rock powder (whole-rock-Savillex) were dissolved using HF/HNO_3 in Savilex beakers sealed and placed on a hotplate set at 120˚C for 24hrs, with this short time and low temperature selected to avoid the dissolution of zircon. One fraction of whole rock powder per-sample (whole-rock-bomb) was placed in a Teflon vessel with ~5 mL of 29M HF and 14M HNO_3 (10:1 by volume) and placed in a Parr-type bomb and heated to 150˚C for 7 days to ensure full dissolution of all phases.

After this samples were dried down and treated with mix of H_3BO_3 and 6M HCl and heated at 120˚C in open Savillex beakers to convert from fluoride to chloride complexes for ion exchange chromatography. All samples were then placed into Teflon vessels with ~5 mL HCl which were subsequently sealed and loaded into Parr-type bombs and heated to 150˚C for 24 hrs to ensure complete dissolution and conversion to chloride complexes. Samples were then transferred into Savillex beakers and spiked with ^{176}Lu–^{180}Hf tracers then sealed and heated at 120°C for 24–48 hr to achieve spike-sample equilibration. Detailed discussion regarding the methods dissolution, spiking and ion exchange chromatography can be found in Cheng, King, Nakamura, Vervoort, and Zhou (2008); Vervoort and Blichert-Toft (1999); Vervoort and Patchett (1996).

Element separates from ion exchange chromatography were dissolved in 2% HNO_3 prior to analysis. Analysis was conducted using Thermo-Finnigan Neptune multi-collector ICP-MS in the Radiogenic Isotope and Geochronology Laboratory, Washington State University. Mass bias corrections were applied using exponential law, using the values of $^{179}Hf/^{177}Hf = 0.7325$. After mass bias correction the session was normalised against the reference standard JMC-475 ($^{176}Hf/^{177}Hf = 0.282160$; Vervoort and Blichert-Toft, The methods of correction for Yb–Lu used are outlined in Vervoort, Patchett, Söderlund, and Baker (2004), with this and other data reduction conducted using a series of in-house spreadsheets.

3.6 | Phase Equilibria Modelling

Calculations were undertaken using THERMOCALC 3.45i (Powell & Holland, 1988) in the NaO–CaO–K_2O–FeO–MgO–Al_2O_3–SiO_2–H_2O–TiO_2–O (NCKFMASHTO) system using DS6.3, modified version of the Holland and Powell (2011) dataset. a-X models used are as follows: garnet, muscovite, paragonite (White, Powell, & Johnson, 2014b); epidote (Holland

& Powell, 2011); omphacite, hornblende, glaucophane, melt (Green et al., 2016). H_2O was set in excess, with O set as 1/10 FeOT. Whole pseudosections were contoured within TCInvestigator 2.0 (Pearce, White, & Gazley, 2015) using THERMOCALC 3.45i in NCKFMASHTO system, using DS6.3 with a-X models as above.

4. | SAMPLE DESCRIPTIONS

Samples were chosen from across the southern WGC while considering a number of factors. Proximity to the Nordfjord–Sogn Detachment (NSDZ) was a primary consideration, to aid in providing constraints on conditions in the footwall of the NSDZ with ideal samples displaying relatively little to no retrogression as to preserve prograde processes. Sample locations are presented in Appendix A.

4.1 | WGC18-008

Sample WGC18-008 is a coarse-grained eclogite from within an un-retrogressed section of the Drøsdal eclogite body, away from obvious late-stage shear-zones and retrogression.

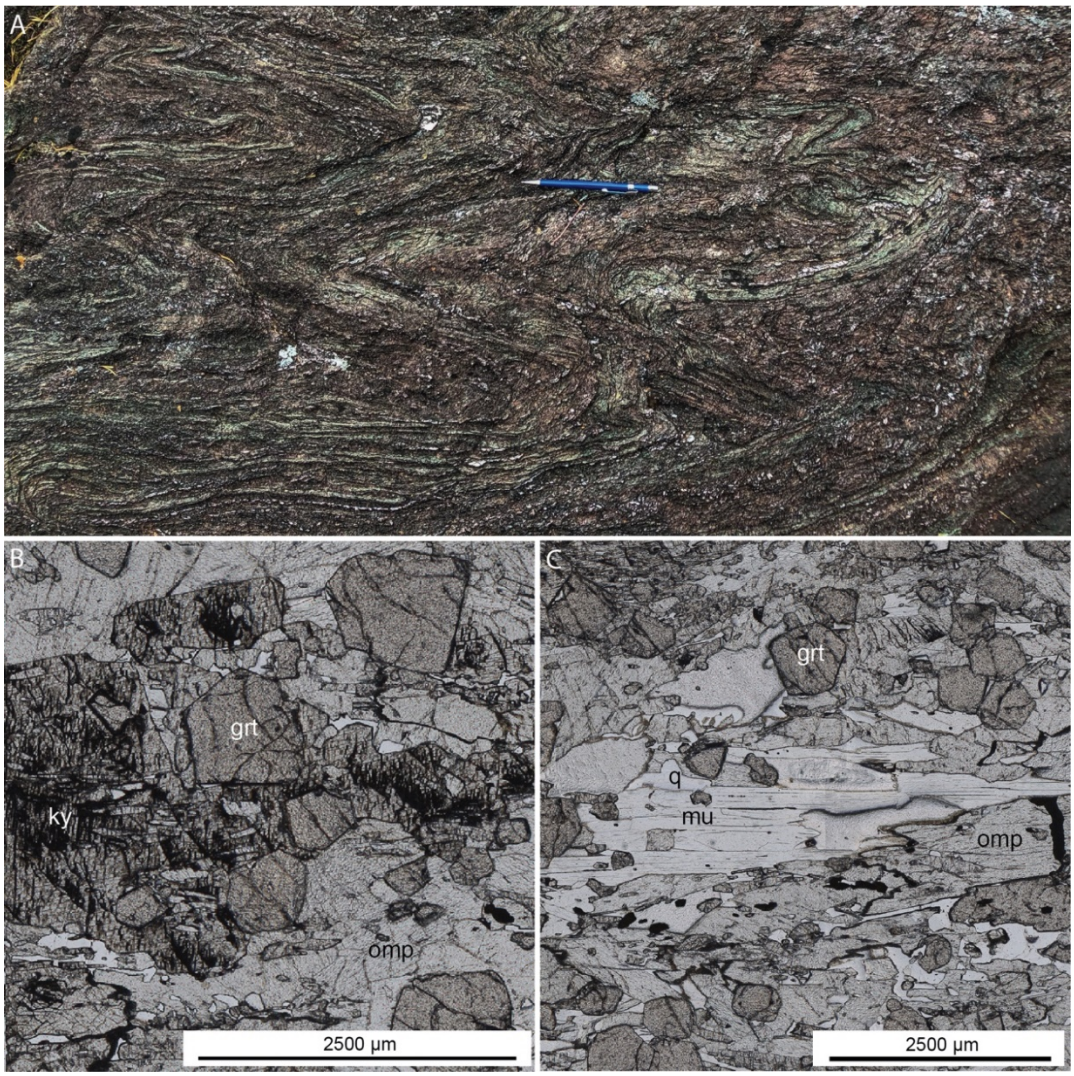

Figure 2.2: A) Field photography of highly folded, but un-retrogressed Drosdal eclogite; B) Photomicrograph of coarse euhedral garnet within kyanite and omphacite; C) Photomicrograph of aligned coarse muscovite and omphacite. Abbreviations are: grt–garnet, omp–omphacite, ky–kyanite, mu–muscovite, q–quartz & symp–symplectite.

Anhedral to subhedral grains of omphacite range between <100 µm blocky grains to 6–7 mm in size, form the bulk of the sample volume. Garnet occurs as small to medium subhedral to euhedral porphyroblasts ranging from 200–2500 µm. Nearly all garnet grains display a fractured appearance with some containing chlorite in these fractures along with small inclusions. Kyanite occurs as subhedral to euhedral porphyroblasts across the sample, ranging from large 5 mm tabular porphyroblasts to small 200–300 µm porphyroblasts with the majority containing inclusions of omphacite and phengite. Kyanite original grain boundaries no longer apparent, with grain boundaries obscured by symplectites hornblende and growth of other minerals. Most kyanite grains also contain fractures that have been infilled by symplectites of hornblende. Phengite in the sample occurs as bladed grains ranging from <100 µm to 2–3mm

in length, predominantly associated with omphacite. Quartz occurs in low abundance in <20–100 μm anhedral grains in the predominantly omphacite matrix. Rutile forms small elongate grains <20–100 μm. Omphacite, muscovite and kyanite form an elongate fabric across the sample, with rutile aligned within.

4.2 | WGC18-011

Sample WGC18-011 is another coarse-grained eclogite from the Drøsdal body, from a near identical position to sample WGC18-008.

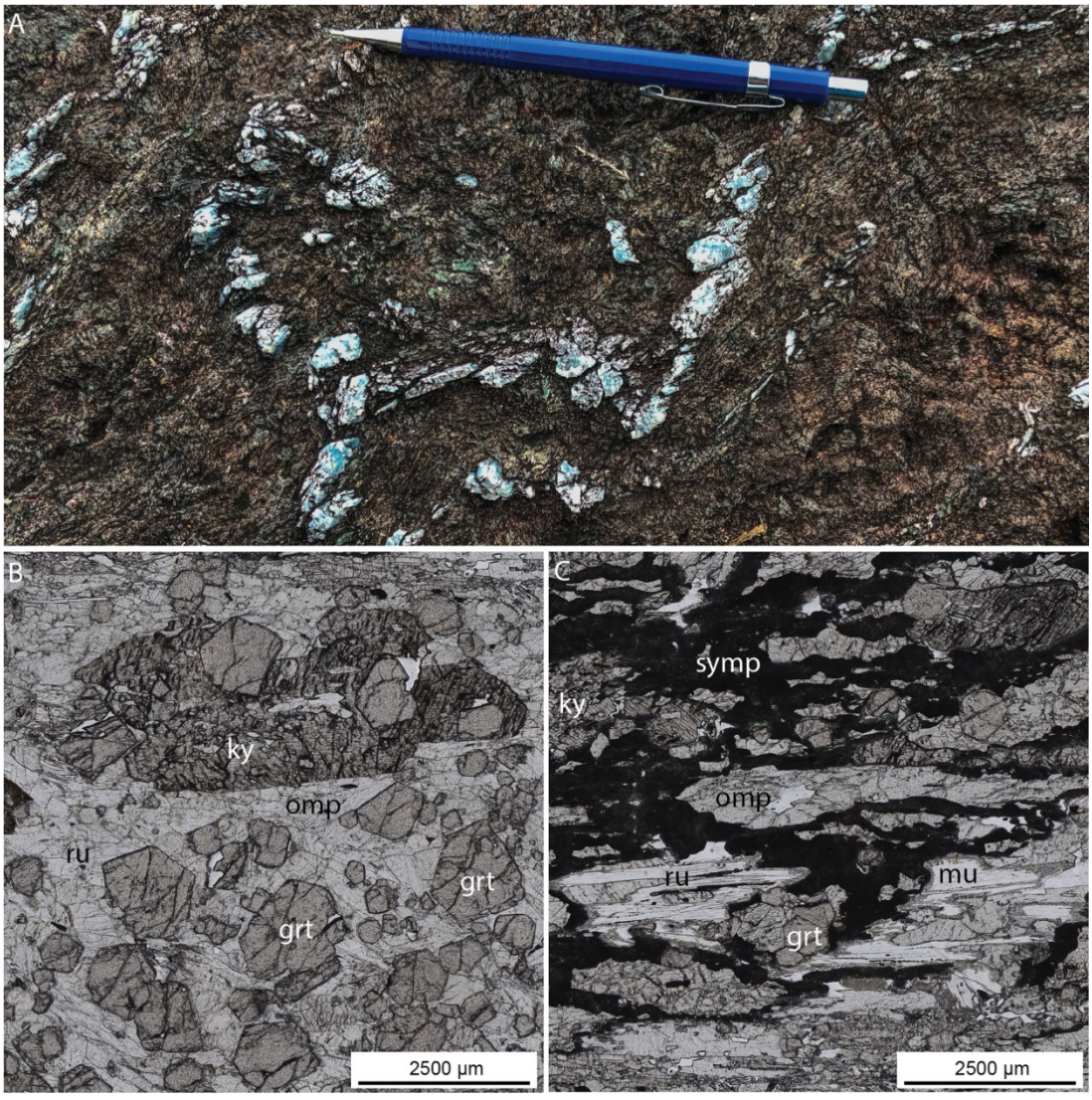

Figure 2.3: A) Field photography of deformed, un-retrogressed Drosdal eclogite, with coarse grained kyanite porphyroblasts aligned within the fabric; B) Photomicrograph of euhedral–subhedral garnet within kyanite and omphacite; C) Photomicrograph of omphacite converted to symplectite, concentrated around abundant muscovite grains. Abbreviations are: grt–garnet, omp–omphacite, ky–kyanite, mu–muscovite, q–quartz & symp–symplectite.

Omphacite forms the majority of non porphyroblastic growth with the sample, occurring as predominantly anhedral, elongate grains, 50– 5000 μm in size. Garnet occurs as small–medium

subhedral to euhedral porphyroblasts, 100–2000 μm in size. Nearly all garnet displays a fractured appearance with some containing a small number of inclusions, garnet proximal to symplectite veining display chlorite rims. Porphyroblasts of subhedral–euhedral elongate–blocky kyanite range from <1000–6000 μm, exhibiting a poikioblastic texture with inclusions of omphacite, phengite and minor quartz and garnet. Original grain boundary occlusion and replacement along fractures occur heavily around and within larger porphyroblasts, with smaller porphyroblasts remaining relatively un-altered. Phengite ranges from small bundles of needle like grains to larger bladed grains. Quartz occurs as small anhedral grains sporadically throughout the sample with no preferred orientation present. Rutile is apparent throughout the sample occurring as stringy grains ranging between <20–100 μm. Omphacite, phengite and kyanite form an elongate fabric across the sample, with rutile trails aligned within.

4.3 | WGC18-016

Sample WGC18-016 is a very coarse-grained eclogite from Vardehia (Figure 2.4).

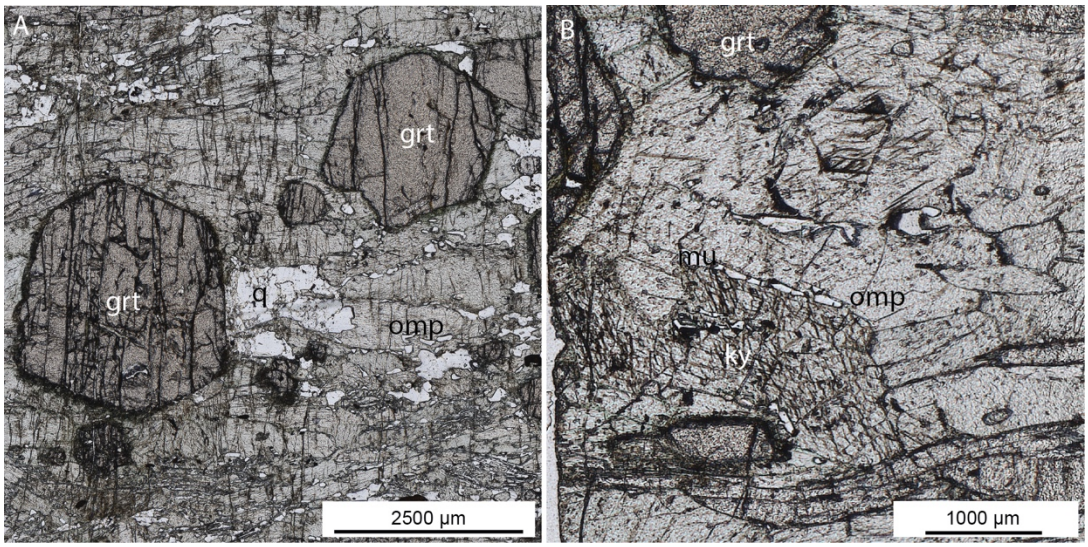

Figure 2.4: A) Photomicrograph of coarse garnet porphyroblasts, also shown are abundant sub-parallel fractures cross-cutting sample perpendicular to foliation; B) Photomicrograph of low abundance kyanite, within omphacite matrix. Abbreviations are: grt–garnet, omp–omphacite, ky–kyanite, mu–muscovite & q–quartz

Sample groundmass consists of coarse subhedral to anhedral omphacite ranging from <250–4000 μm in size. Very coarse euhedral garnet porphyroblasts, 500–4000 μm occur within the groundmass with omphacite-quartz groundmass loosely wrapping around. Minor anhedral blocky kyanite occurs randomly within the sample 200–500 μm, with significantly altered primary grain boundaries and abundant inclusions of quartz and rutile. Small anhedral quartz grains occur within omphacite groundmass and as inclusions in garnet. Omphacite, kyanite and quartz define a fabric within the sample, wrapping garnet porphyroblasts. Widespread,

near parallel fractures crosscut all phases perpendicular to omphacite defined foliation, infilling these fractures within garnet are minor chlorite and quartz.

4.4 | WGC18-022

Sample WGC18-022 is very coarse-grained eclogite from Vårdalsneset taken from (Figure 2.5).

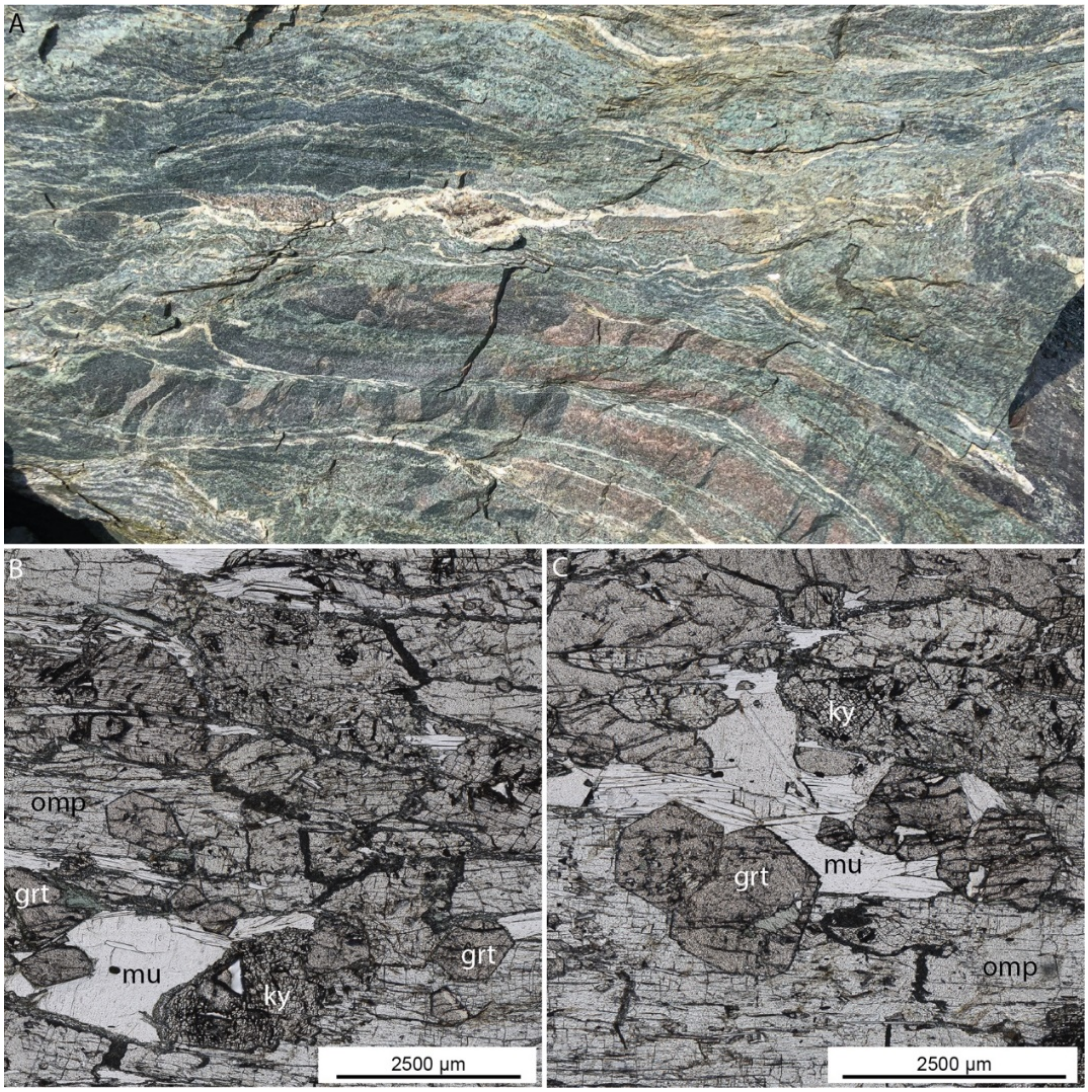

Figure 2.5: A) Field photography of Vardalsneset eclogite; B) Photomicrograph of coarse omphacite interlocked with garnet and kyanite C) Photomicrograph of coarse omphacite and coarse bladed muscovite. Abbreviations are: grt–garnet, omp–omphacite, ky–kyanite, mu–muscovite & q–quartz

Very coarse omphacite forms the majority of the ground mass, with elongate grains in excess of 6000 µm in length, with smaller blockier grains 2000–3000 µm. Euhedral, coarse grained garnet porphyroblasts 500–2500 µm in size occurs in lower modal abundance than other samples investigated by this study, while some finer (100–200 µm) occur dotted within the groundmass, with some occurring as inclusions within kyanite and omphacite. Coarse garnet

porphyroblasts are heavily fractured, with minor inclusions within larger grains while finer grains remain relatively unfractured. Coarse grained euhedral to subhedral kyanite porphyroblasts, 3000–7000 μm in size occur within the groundmass. Porphyroblasts are heavily fractured, with grain boundary corrosion and symplectite forming along these, a moderate volume of inclusions of omphacite, quartz, phengite and rutile are present within most grains. Coarse, elongate bladed phengite occurs as bladed clusters within the omphacite groundmass with blades predominantly 1000–2500 μm in length. Omphacite, kyanite and phengite define a foliation across the sample, slightly wrapping garnet porphyroblasts.

4.5 | WGC18-027

Sample WGC18-027 is a fine-grained, massive eclogite from the town of Naustdal (Figure 2.6).

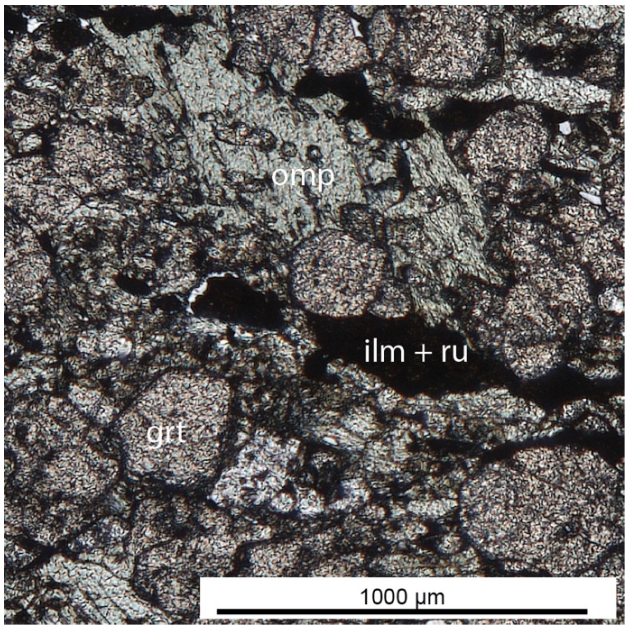

Figure 2.6: No field photograph available, very fine grained interlocked omphacite with equally fine-grained garnet within the matrix

The sample has a massive overall texture with interlocking garnet and omphacite grains with higher modal percentage garnet than omphacite. Garnet grains are predominantly subhedral in habit ranging 100–500 μm. Omphacite interlocked between the garnet grains are anhedral, with a similar size (100–500 μm) to garnet, with minor symplectisation occurs around some omphacite grain boundaries. Phengite occur within the interlocked garnet-omphacite matrix with phengite as sporadic small needles 100–200 μm. Quartz occurs as a range of anhedral habits, infilling between the interlocked matrix ranging from 100–1000 μm in size. Minor rutile grains with overgrown magnetite/hematite grains exist as elongate to stringy textures intergrown within the garnet and omphacite matrix.

4.6 | WGC18-029

Sample WCG18-029 is a fine-grained eclogite from Engebøfjellet (Figure 2.7), on a field scale it displays well defined red and green banding with veins of quartz indispersed.

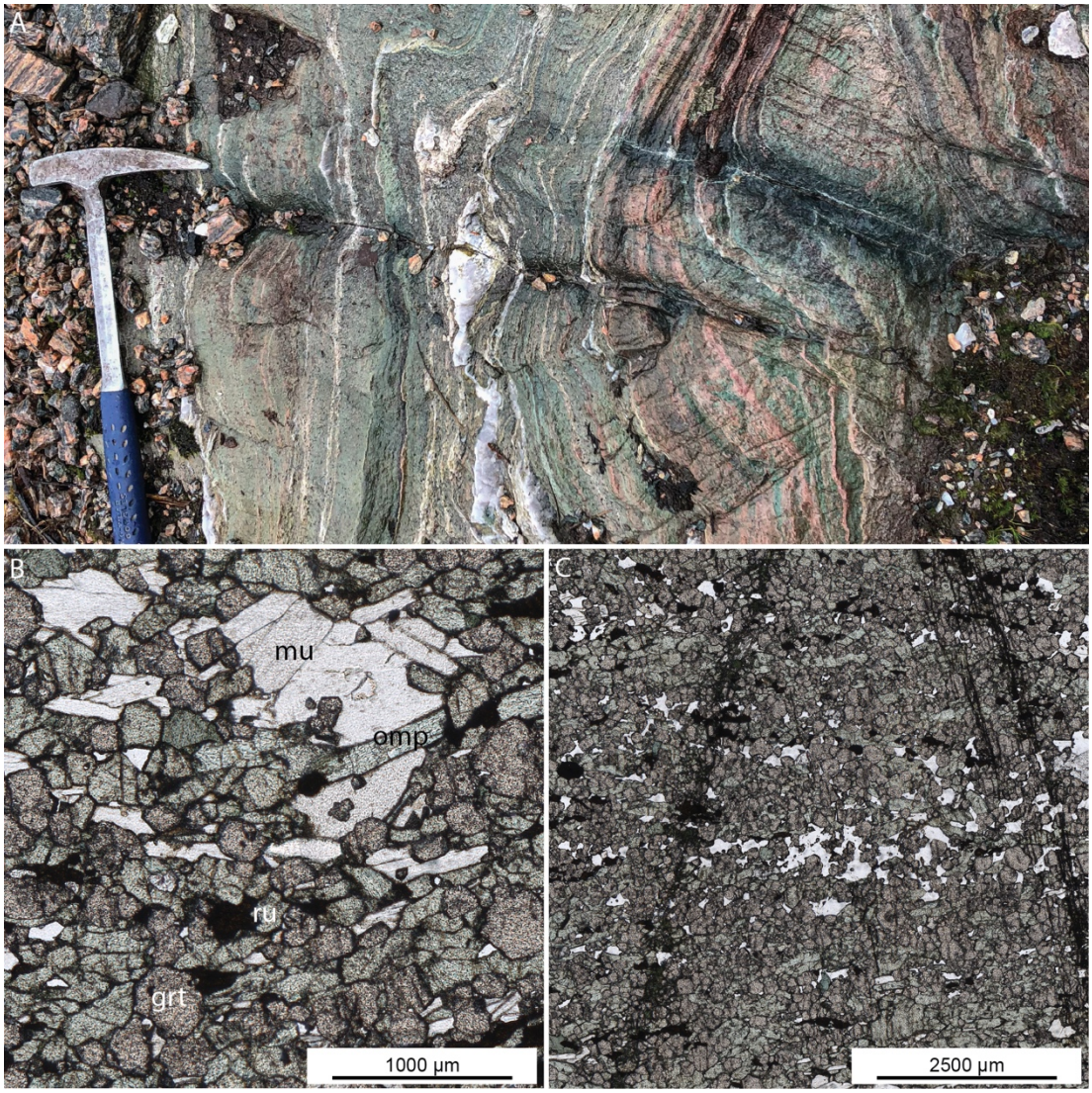

Figure 2.7: A) Field photography of Engebøfjellet eclogite, fine, sub-parallel fractures truncating the fabric can be seen running left to light; B) Photomicrograph of very fine grained omphacite interlocked with garnet and in dispersed muscovite C) Photomicrograph of fractures outlined in A, sympectisation can be seen away from the fracture. Abbreviations are: grt–garnet, omp–omphacite, mu–muscovite, q–quartz & ru–rutile

The sample consists of interlocked garnet and omphacite grains with a higher modal percentage of omphacite. Garnet grains are predominantly anhedral to subhedral in habit ranging 100–400 µm, with minor inclusions of quartz and opaque material occurring in larger grains. Omphacite interlocked between the garnet grains are subhedral forming tabulate habits, 200–1000 µm long with minor symplectisation occurring around some grain boundaries. Phengite occur within the interlocked garnet-omphacite matrix as sporadic small flecks 100–

400 μm, with some larger blades up to 1000 μm. Quartz occurs as a range of anhedral habits, infilling between the interlocked matrix ranging from 100–1000 μm in size. Minor rutile grains with overgrown magnetite/hematite exist as elongate to stringy textures intergrown within the garnet and omphacite matrix. Late stage near parallel fractures crosscut the sample with sympectisation occurring around garnet and omphacite ~500 μm either side of the fractures.

5. | MINERAL CHEMISTRY

5.1 | Major element chemistry

Garnet endmember compositions from sample WGC18-008 range from $grs_{19.7}$ (grs_x=Ca/Fe+Ca+Mg+Mn) $alm_{43.9}$ (alm_x=Fe/Fe+Ca+Mg+Mn) $prp_{35.8}$ (prp_x=Mg/ Fe+Ca+Mg+Mn) $spss_{0.6}$ ($spss_x$=Mn/Fe+Ca+Mg+Mn) at the rim to $grs_{26.3}$ $alm_{58.2}$ $prp_{11.4}$ $spss_{4.1}$ at the core. WGC18-016 range from $grs_{24.1}$ $alm_{53.8}$ $prp_{21.8}$ $spss_{0.3}$ at the rim to $grs_{27.1}$ $alm_{58.4}$ $prp_{12.9}$ $spss_{2.2}$ at the core. WGC18-022 range from $grs_{20.8}$ $alm_{49.2}$ $prp_{29.0}$ $spss_{1.}$ at the rim to $grs_{22.2}$ $alm_{55.2}$ $prp_{18.2}$ $spss_{4.4}$ at the core. WGC18-027 range from $grs_{22.4}$ $alm_{58.4}$ $prp_{16.3}$ $spss_{0.1}$ at the rim to $grs_{22.7}$ $alm_{58.8}$ $prp_{17.5}$ $spss_{1.0}$ at the core. WGC18-029 range from $grs_{19.4}$ $alm_{63.0}$ $prp_{16.5}$ $spss_{1.1}$ at the rim to $grs_{29.8}$ $alm_{56.9}$ $prp_{11.5}$ $spss_{1.8}$ at the core.

Larger porphyroblasts from samples WGC18-008 and WGC18-016 display Mn enriched, Mg depleted cores diffusing to the grain rim (Figure 2.8; Figure 2.9A; B), characteristic of prograde zoning. Smaller porphyroblasts from samples WGC18-022, WGC18-027 and WGC18-029 (Figure 2.8; Figure 2.9C; D; E) do not display the same degree of zoning with their endmember profiles relatively flat across the grains.

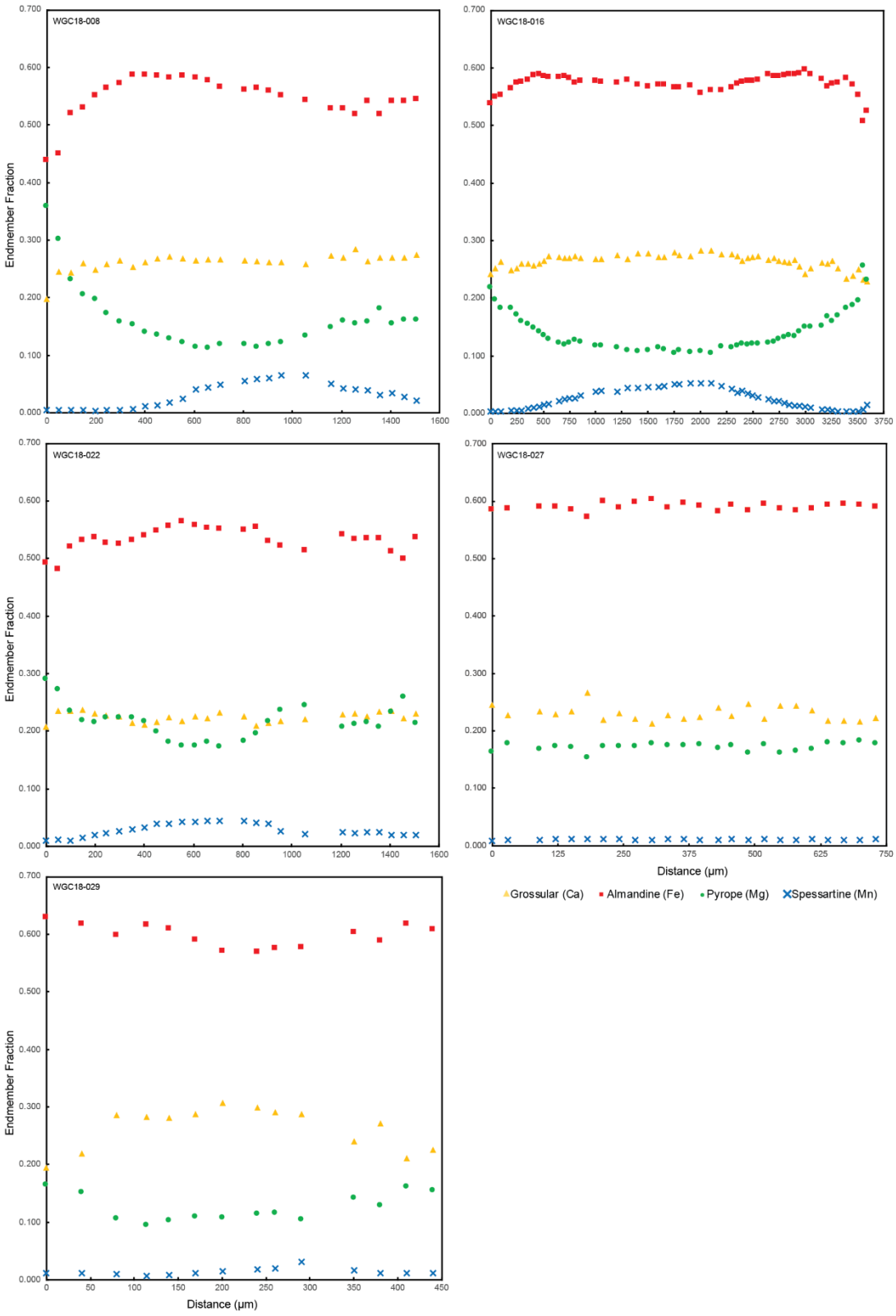

Figure 2.8: Garnet endmember traverses by EMPA from samples WCG18-008, WGC18-016, WGC18-022, WGC18-029 and WGC18-029.

Samples with larger porphyroblasts (WGC18-008 and WGC18-016) display distinct resorption rims in Fe, Ca, Mg and Mn varying in width from 200–300 μm. Slightly finer garnet

porphyroblasts from sample WGC18-016 has resorption rims apparent in Fe, Ca, Mg and Mn, but at a lesser elevated abundance than compared to samples WGC18-008 and WGC18-016. Sample WGC18-027 does not display any evidence of resorption rims within grains mapped, though grains within this sample are more anhedral and may not represent original grain boundaries. Sample WCG18-029 also displays resorption rims in Fe, Ca, Mg and Mn 100–300 μm wide, resorption rims in this sample make up a far greater proportion of the grain diameter than other examples in this study.

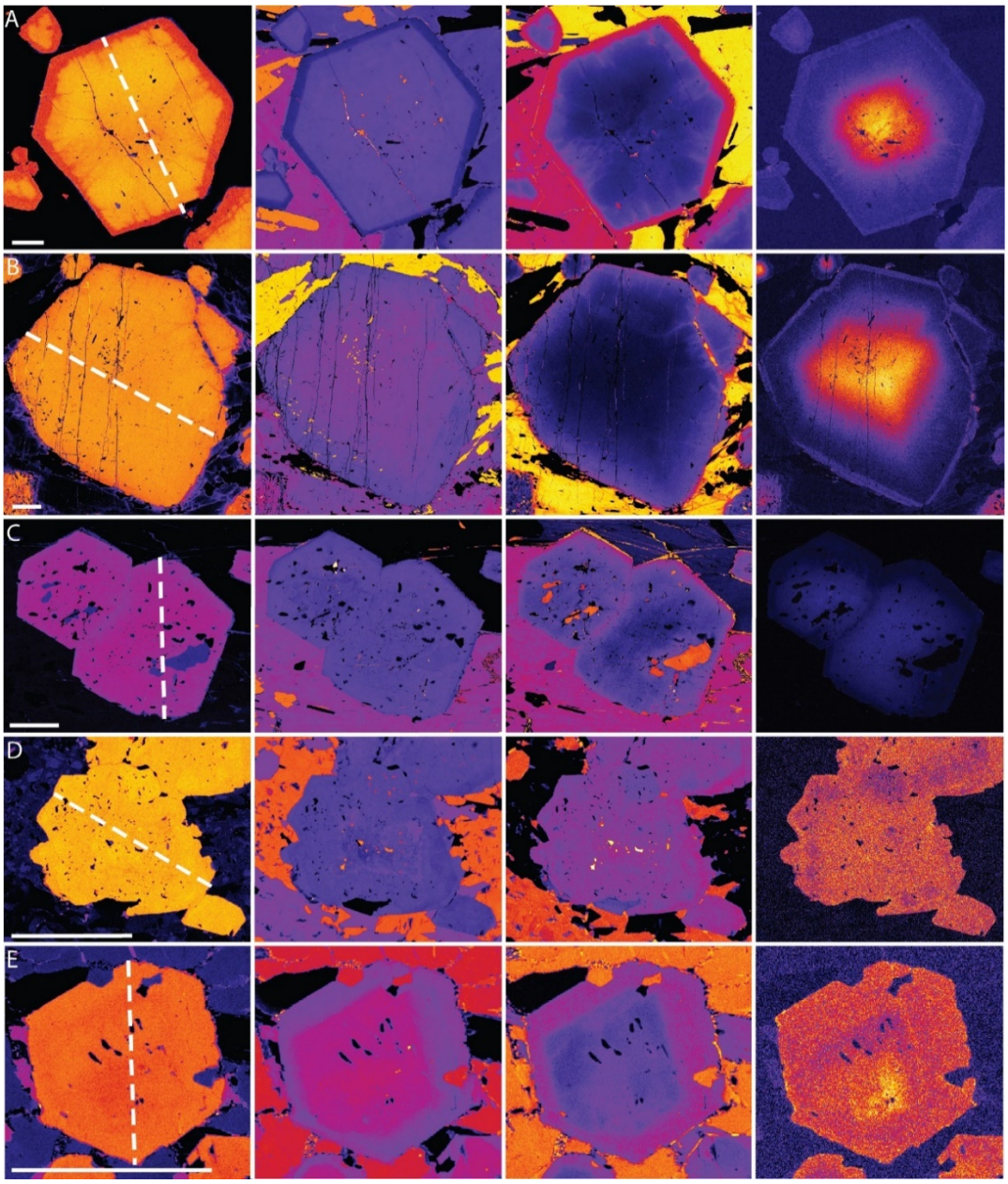

Figure 2.9: EMPA mapping of garnet, maps are non-quantitative, hot colours represent high concentration while cool colours represent low concentrations, colours are not comparable between images. A) Map of Fe, Ca, Mg & Mn (L-R) for garnet from sample WGC18-008; B) Map of Fe, Ca, Mg & Mn (L-R) for garnet from sample WGC18-016; C) Map of Fe, Ca, Mg & Mn (L-R) for garnet from sample WGC18-022; D) Map of Fe, Ca, Mg & Mn (L-R)

for garnet from sample WGC18-008 E) Map of Fe, Ca, Mg & Mn (L-R) for garnet from sample WGC18-029. Scale bar represents 500 μm in all images, dashed white line represents direction of EMPA and subsequent LA-ICP-MS traverse.

Omphacite composition between samples varies, when defined by the jadeite composition (jd_x=Na/Fe+Ca+Mg) the following mean values are measured: for sample WGC18-008 $Jd_{43.9}$, WGC18-016 $Jd_{9.6}$, WGC18-022 $Jd_{48.3}$, WGC18-027 $Jd_{52.1}$ and WGC18-029 $Jd_{38.7}$. Overall chromium content is low, with mol% chromium >1% or near/below LOD in some cases. Titanium also records similar trends across all samples, with mol% chromium >1% or near/below LOD/.

White mica within these samples is phengitic in composition, containing appreciable amounts of Mg. Within sample WGC18-008 the phengite contains 8.81 mol% Mg, this is similar to samples WGC18-022, WGC18-027 and WGC18-029 which contain on average 8.37 mol% Mg, 7.26 mol% Mg and 8.50 mol% Mg respectively. Some Na is also present, 2.9 mol% Na, 2.95 mol% Na, 2.71 mol% Na and 0.8 mol% Na respectively across samples WGC18-008, WGC18-022, WGC18-027 and WGC18-029.

5.2 | Trace element geochemistry

LREE elements (lighter than europium) not presented due to near or below LOD for LA-ICP-MS analysis. The overall abundance of M/HREE is low (>0–4 ppm) in all samples except for WGC18-029 which displays relatively greater abundance of M/HREE with peak abundance of Yb and Lu in the order of 85–95 ppm. All garnets analysed display HREE enriched core, with overall core enrichment by a factor of 2–4 times compared to rim abundances. MREE remain relatively consistent across the porphyroblasts analysed, with minor trends mirroring HREE towards the centre of some porphyroblasts. Samples WGC18-016, WGC18-022, WGC18-027 and WGC18-029 display HREE enrichment in rim with the thickness of this enriched zone corresponds to major element enrichment seen in Figure 2.9, MREE enrichment is low if not absent in these resorption rims.

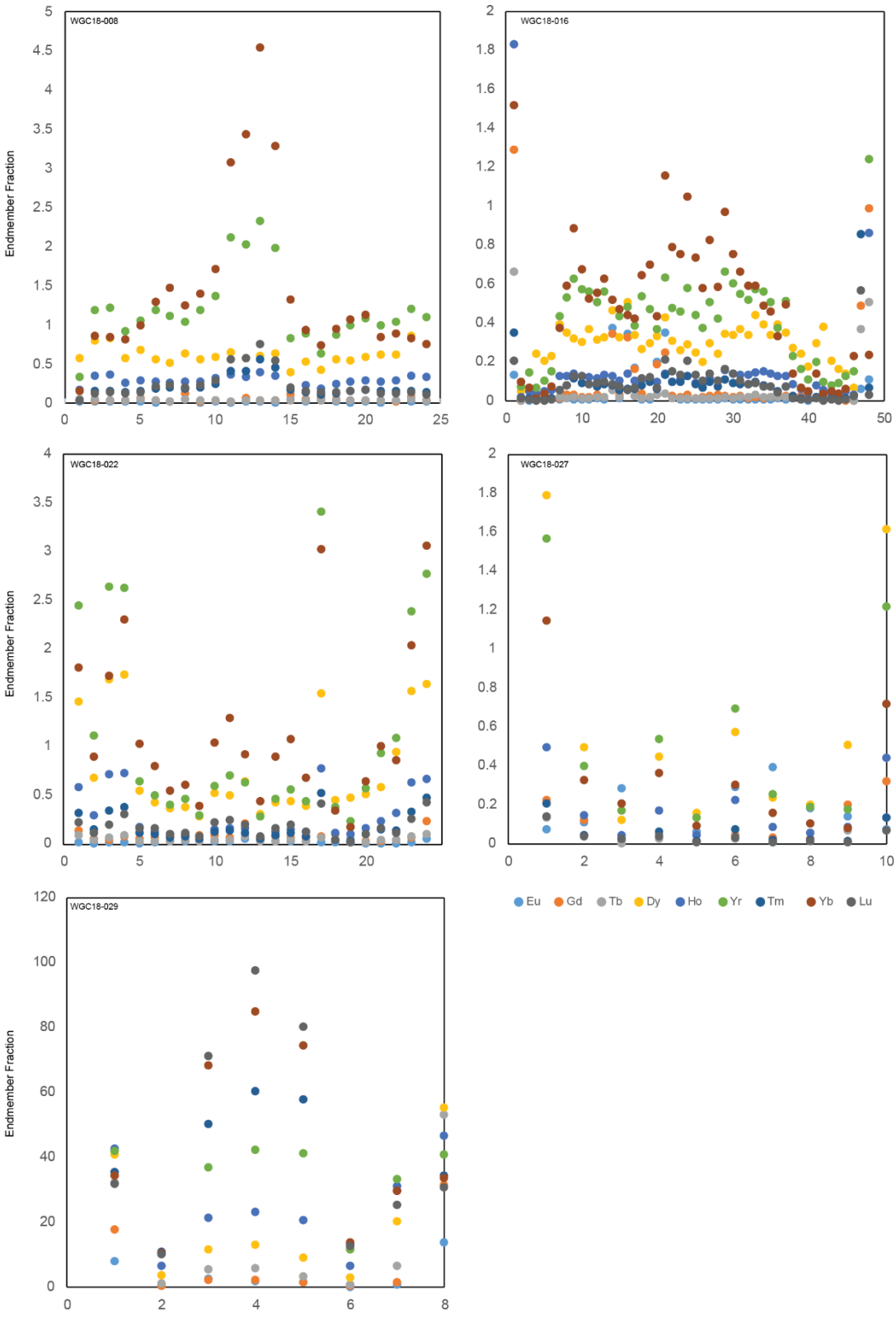

Figure 2.10: MREE/HREE abundances across garnet porphyroblasts by LA-ICP-MS from samples WCG18-008, WGC18-016, WGC18-022, WGC18-029 and WGC18-029.

6. | PHASE EQUILIBRIA MODELLING

Six eclogite samples were selected from five different eclogite bodies from within the Dalsfjorden and Førdefjorden area (Figure 2.1). Samples were chosen due to their proximity to the Nordfjord–Sogn detachment, representing some of the most south-easterly surface expression of eclogite within the Western Gneiss Complex, a variety of grain size and mineralogy was also chosen for these purposes. Modelled bulk rock compositions in the NCKFMASHTO system for each of these samples are shown in Table 2.1, see 3.2 for acquisition methodology.

Sample	**WGC18-008**	**WGC18-011**	**WGC18-016**	**WGC18-022**	**WGC18-027**	**WGC18-029**
TiO_2	0.34	0.15	0.03	0.11	3.09	2.87
SiO_2	47.33	46.85	44.96	52.53	45.04	47.74
Al_2O_3	12.94	10.32	8.92	11.81	10.11	8.17
CaO	11.00	9.76	12.36	9.93	11.06	11.17
MgO	12.58	17.03	16.50	9.58	8.01	8.07
FeOT	7.24	7.25	8.37	3.97	15.96	13.96
O	0.36	0.36	0.42	0.20	0.80	0.70
K_2O	0.41	0.16	0.05	0.32	0.07	0.15
Na_2O	2.47	2.37	1.36	6.36	3.17	2.89
H_2O	5.18	5.60	6.89	5.11	2.47	4.07

Table 2.1: Bulk rock compositions used for phase equilibria modelling in the NCKFMASHTO system

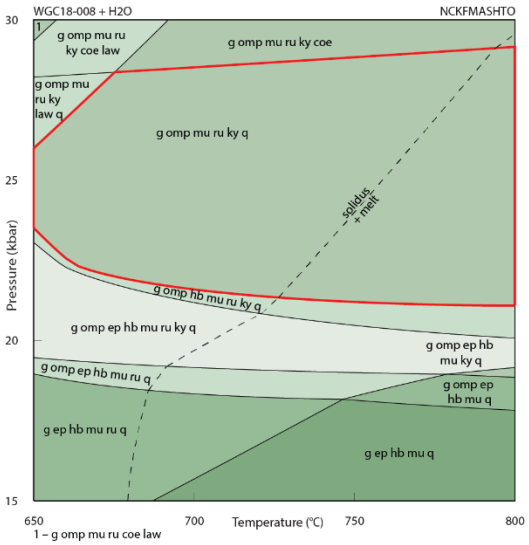
WGC18-008 + H2O
NCKFMASHTO
g omp mu ru ky coe law
g omp mu ru ky coe
g omp mu ru ky law q
g omp mu ru ky q
solidus + melt
g omp hb mu ru ky q
g omp ep hb mu ru ky q
g omp ep hb mu ky q
g omp ep hb mu ru q
g omp ep hb mu q
g ep hb mu ru q
g ep hb mu q
Pressure (kbar)
Temperature (°C)
1 – g omp mu ru coe law

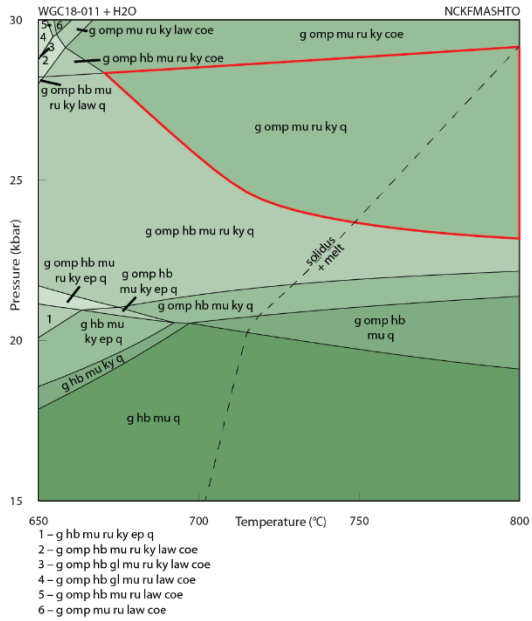
WGC18-011 + H2O
NCKFMASHTO
g omp mu ru ky law coe
g omp mu ru ky coe
g omp hb mu ru ky coe
g omp hb mu ru ky law q
g omp mu ru ky q
g omp hb mu ru ky q
g omp hb mu ru ky ep q
g omp hb mu ky ep q
g omp hb mu ky q
solidus + melt
g hb mu ky ep q
g omp hb mu q
g hb mu ky q
g hb mu q
Pressure (kbar)
Temperature (°C)
1 – g hb mu ru ky ep q
2 – g omp hb mu ru ky law coe
3 – g omp hb gl mu ru ky law coe
4 – g omp hb gl mu ru law coe
5 – g omp hb mu ru law coe
6 – g omp mu ru law coe

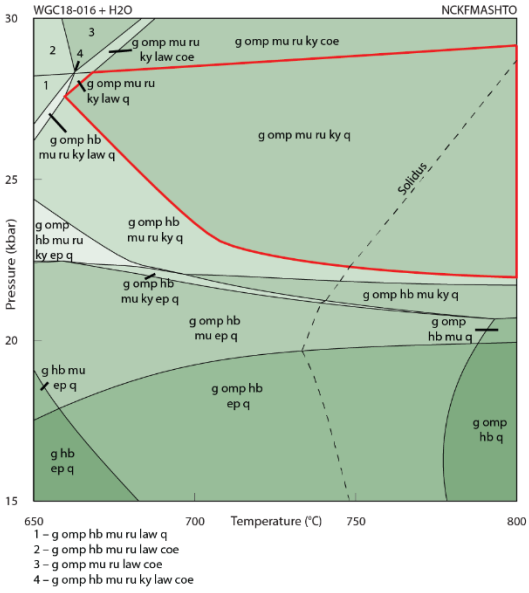
WGC18-016 + H2O
NCKFMASHTO
g omp mu ru ky law coe
g omp mu ru ky coe
g omp mu ru ky law q
g omp hb mu ru ky law q
g omp mu ru ky q
Solidus
g omp hb mu ru ky q
g omp hb mu ru ky ep q
g omp hb mu ky ep q
g omp hb mu ky q
g omp hb mu ep q
g omp hb mu q
g hb mu ep q
g omp hb ep q
g omp hb q
g hb ep q
Pressure (kbar)
Temperature (°C)
1 – g omp hb mu ru law q
2 – g omp hb mu ru law coe
3 – g omp mu ru law coe
4 – g omp hb mu ru ky law coe

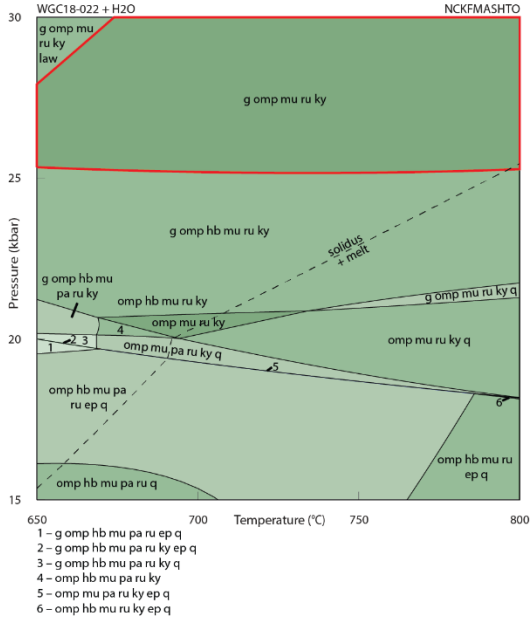
WGC18-022 + H2O
NCKFMASHTO
g omp mu ru ky law
g omp mu ru ky
g omp hb mu ru ky
solidus + melt
g omp hb mu pa ru ky
omp hb mu ru ky
g omp mu ru ky q
omp mu ru ky
omp mu ru ky q
omp mu pa ru ky q
omp hb mu pa ru ep q
omp hb mu ru ep q
omp hb mu pa ru q
Pressure (kbar)
Temperature (°C)
1 – g omp hb mu pa ru ep q
2 – g omp hb mu pa ru ky ep q
3 – g omp hb mu pa ru ky q
4 – omp hb mu pa ru ky
5 – omp mu pa ru ky ep q
6 – omp hb mu ru ky ep q

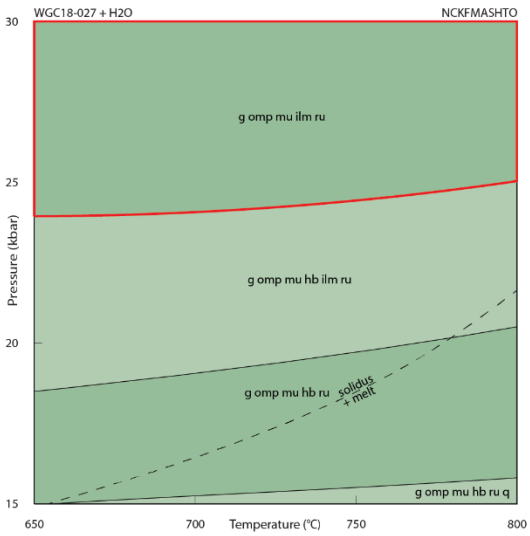
WGC18-027 + H2O
NCKFMASHTO
g omp mu ilm ru
g omp mu hb ilm ru
g omp mu hb ru
solidus + melt
g omp mu hb ru q
Pressure (kbar)
Temperature (°C)

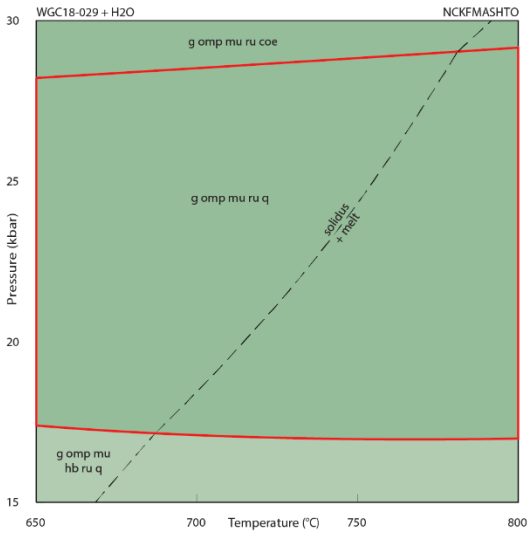
WGC18-029 + H2O
NCKFMASHTO
g omp mu ru coe
g omp mu ru q
solidus + melt
g omp mu hb ru q
Pressure (kbar)
Temperature (°C)

Figure 2.11: Pseudosections of samples WGC18-008, WGC18-011, WGC18-016, WGC18-022, WGC18-027 & WGC18-029 in the NCKFMASTO system, compositions modelled are given in Table 2.1. Abbreviations are as follows: grt–garnet, omp–omphacite, ky–kyanite, hb–hornblende, ep–epidote mu–muscovite, pa–paragonite, law–lawsonite, q–quartz, coe–coesite, ru–rutile, ilm–ilmenite.

For coarse grained samples WGC18-008, WGC18-011, WGC18-016 peak assemblages predicted by the models are identical, consisting of garnet–omphacite–kyanite–muscovite–quartz–rutile, while coarse grained WGC18-022 lacks quartz. While for fine grained samples the peak field for sample WHC18-027 is garnet–omphacite–muscovite–ilmenite–rutile and for sample WGC18-029 is garnet–omphacite–muscovite–rutile–quartz (Figure 2.9). These peak assemblages constrain the samples to the following peak conditions: WGC18-008, 650–800˚C at 22–28 kbar; WGC18-011, 670–800˚C at 24–28 kbar; WGC18-016, 660–800˚C at 23–28 kbar; WGC18-022 at >25 kbar; WGC18-027 at >24 kbar and WGC18-029 at <650–780 ˚C 18–28 kbar (Figure 2.9).

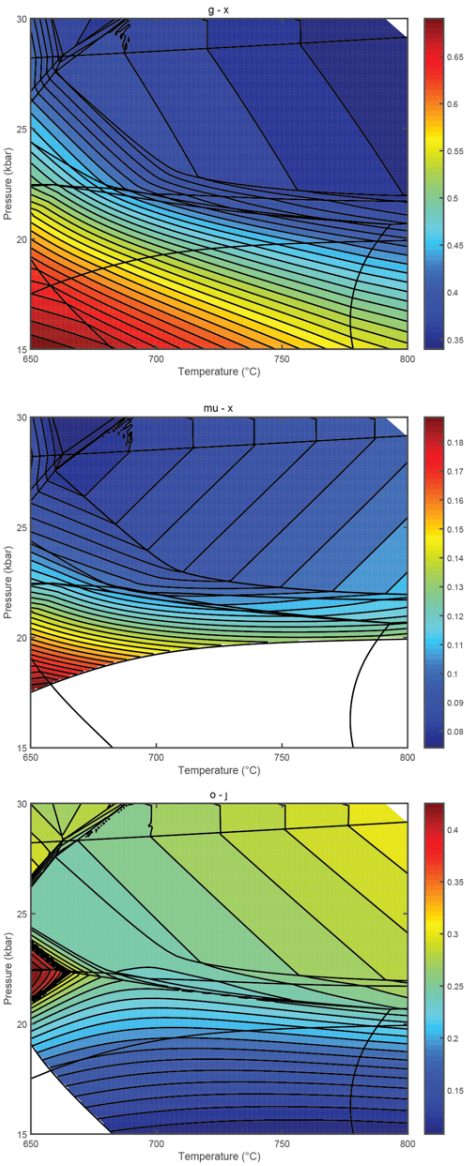

Figure 2.12: Isopleths for g -x, mu -x and o -j from sample WGC18-016 calculated within TCInvestigator 2.0. g-x is defined as Fe(X-site)/(Fe(X-site)+Mg(X-site)); mu-x is defined as Fe(M2A-site)/(Fe(M2A-site -site)+Mg(M2A-site -site)) and o-j is defined as (Na(M2c-site) + xNa(M2n-site))/2; see White et al., (2014) for further information.

Addition of contoured peak fields is of limited usefulness in further constraining peak conditions within each sample due to only small variances in mineral composition occurring across a wide range of conditions within the peak field (Figure 2.12).

7. | LU–HF GARNET GEOCHRONOLOGY

Two coarse grained eclogite samples; from Drøsdal (WGC18-008) and Vardehia (WGC18-016) returned ages of 437 ± 34 Ma (MSWD = 374) and 513 ± 110 Ma (MSWD = 1578) respectively. One medium–fine grained eclogite from Vardalsneset (WGC18-022) returned an age of 421 ± 24 Ma (MSWD = 236). Two fine grained eclogites; from Naustdal (WGC18-027) and Engebøfjellet (WGC18-029) returned ages of 449 ± 80 Ma (MSWD = 2008) and 428 ± 34 Ma (MSWD = 200) respectively. Isochron ages were calculated using Isoplot 3.75 (Ludwig, 2003) with the ^{176}Lu decay constant of 1.865×10^{-11} yr^{-1} (Scherer, Münker, & Mezger, 2001) for three or four analyses of garnet and one or two of whole rock leachate per isochron, see 3.5 for further details.

Sample	^{176}Lu/^{177}Hf	2σ (abs)	^{176}Hf/^{177}Hf	2σ (abs)	Age
WGC18-008-G1	1.375290	0.006876	0.294228	0.000018	
WGC18-008-G2	1.301579	0.006508	0.293295	0.000019	
WGC18-008-G3	1.270109	0.006351	0.293434	0.000018	
WGC18-008-G4	1.290550	0.006453	0.293783	0.000024	
WGC18-008-WRS	0.010468	0.000052	0.282853	0.000015	437 ± 34
WGC18-016 G5	1.038692	0.005193	0.291557	0.000030	
WGC18-016-G1	0.957631	0.004788	0.291827	0.000035	
WGC18-016-G2	0.960702	0.004804	0.293511	0.000022	
WGC18-016-G4	1.027146	0.005136	0.291675	0.000022	
WGC18-016-WRB	0.008030	0.000040	0.283153	0.000016	
WGC18-016-WRS	0.013449	0.000067	0.283115	0.000015	513 ± 110
WGC18-022 G5	0.802483	0.004012	0.288856	0.000017	
WGC18-022-G3	1.980604	0.009903	0.298281	0.000016	
WGC18-022-G4	2.265002	0.011325	0.300390	0.000018	
WGC18-022-WRB	0.011070	0.000055	0.282744	0.000015	
WGC18-022-WRS	0.030033	0.000150	0.282707	0.000016	421 ± 24
WAC18-027 G5	0.463556	0.002318	0.286576	0.000017	
WGC18-027-G1	1.074643	0.005373	0.292128	0.000018	
WGC18-027-G2	1.218397	0.006092	0.293160	0.000018	

WGC18-027-G3	1.462626	0.007313	0.293966	0.000018	
WGC18-027-G4	1.219437	0.006097	0.295490	0.000017	
WGC18-027-WRB	0.005990	0.000030	0.283471	0.000015	
WGC18-027-WRS	0.010170	0.000051	0.283495	0.000015	449 ± 80
WAC18-029 G5	0.346055	0.001730	0.285491	0.000015	
WGC18-029-G1	1.333205	0.006666	0.293199	0.000017	
WGC18-029-G2	0.948445	0.004742	0.289883	0.000016	
WGC18-029-G3	1.299156	0.006496	0.293312	0.000017	
WGC18-029-G4	1.446518	0.007233	0.294010	0.000017	
WGC18-029-WRB	0.012971	0.000065	0.282521	0.000014	
WGC18-029-WRS	0.058327	0.000292	0.283107	0.000015	428 ± 34

Table 2.2: Summary of Lu–Hf analyses conducted by ID-MCP-MS.

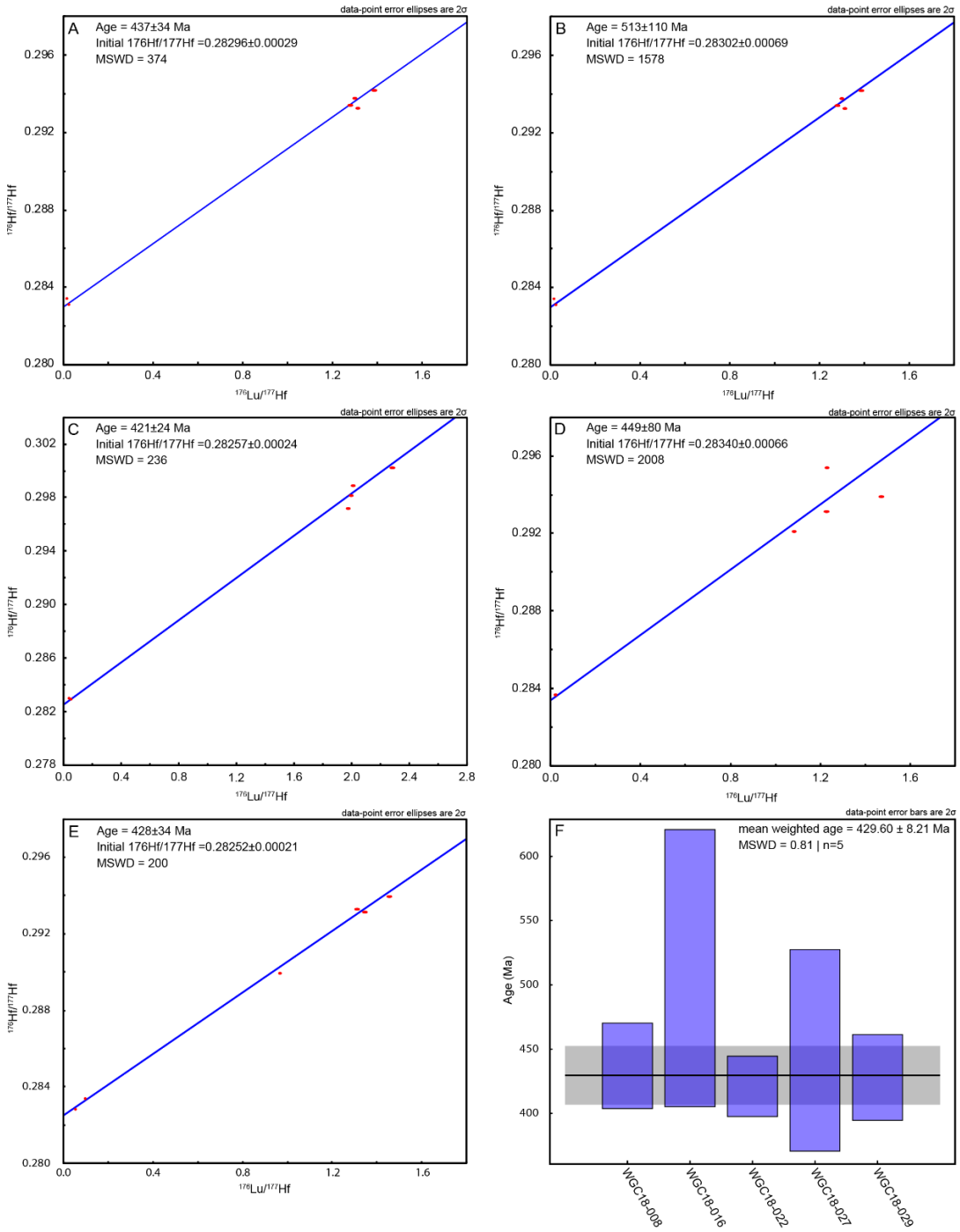

Figure 2.13: Lu-Hf garnet isochrons for Table 3.3 below, samples as follows. A) WGC18-008; B) WGC18-016; C) WGC18-022; D) WGC18-027 & E) WGC18-029. F) Weighted mean plot of all samples to illustrate error ranges

Samples WGC18-0016 and WGC18-27 present particularly large errors (see Figure 2.13F), with all samples exhibiting spread away from the isochron see 8.3 for further discussion regarding errors and high MSWD.

8. | DISCUSSION

8.1 | *P–T* conditions

Precisely constraining the peak conditions of eclogite formation has long proven difficult for a multitude of reasons, with those presented in this study no different. The bulk of data from the Western Gneiss Complex comes in the form of the conventional garnet-clinopyroxene Mg-Fe exchange thermometer and the jadeite-diopside exchange barometer. Conventional thermometers such as these have large errors (often ± 50˚C), with early formulations of this thermometer having potentially understated or overstated temperatures in the order of 50–100˚C (Nakamura, 2009). Other useful barometers such as Si in phengite fail at pressures greater than 16–22 kbar, or only produce minimum values due to eclogites lacking the required assemblage (Massonne & Schreyer, 1987).

Low variance assemblages, along with low variation in mineral compositions within fields makes contouring difficult to aid in the establishment of more precise *P–T* estimate/s via phase equilibria modelling. The Green et al. (2016) melt model aX relationships within the DS 6.3 dataset (Holland & Powell, 2011) is only calibrated to 13 kbar, far lower than the maximum of 30 kbar modelled within this study. As a result, modelling of melting was not carried out past the solidus due to the likelihood of spurious results, but as the eclogites are sub-solidus this is irrelevant for establishing peak *P–T* conditions. Sample WGC18-016 contains muscovite across the pseudosection (Figure 2.11), despite none being present within the rock (Figure 2.4). It may be noted that the clinopyroxene model included in the Green et al. (2016) aX relationships within the DS 6.3 dataset does not contain modelling for K within its structure. Thus, the introduction of K into the whole rock composition from omphacite may lead to the incorrect introduction of muscovite into the pseudosection, with omphacite of this sample containing 1–1.5 wt% K. The lack of K within the omphacite models may also increase the modal percentage of muscovite in other samples if omphacite contains appreciable K.

The overlapping nature of these pseudosections places southern eclogites at 670–780˚C and 24–28 kbar during the peak of the Caledonian Orogeny. Previous *P–T* estimates from the southern Western Gneiss complex are sporadic, with no previous data existing for eclogites with the Drøsdal (WGC18-008 & WGC18-011), Vardhia (WGC18-016) Naustdal, (WGC18-027) or Engebofjellet (WGC18-029) eclogite bodies. Eclogites occurring at Vårdalsneset (WGC18-022) have produced some previously published data (e.g. Engvik & Andersen, 2000; Labrousse et al., 2004; Martin & Duchêne, 2015). *P–T* estimates range from 677 ± 21˚C at 16 ± 2 kbar, and 691 ± 20˚C 15 ± 1.5 kbar (Engvik & Andersen, 2000) to 615 ± 22˚C 22.7 kbar as a via the garnet-clinopyroxene Mg–Fe exchange thermometer, phengite barometer and jadeite-diopside exchange barometer. While the addition of phase equilibria modelling to this

earlier data returns *P–T* estimates of 590–720 °C, 15–25 kbar (Martin & Duchêne, 2015). Upper pressure estimates from Martin and Duchêne (2015) are constrained to less than 25 kbar, with the authors noting that no coesite is present thus pressures must be less than this when in reality the α-quartz to coesite transition occurs higher at pressures in the range of 28–29 kbar (Chao, Shoemaker, & Madsen, 1960; Chopin, 1984; Coes, 1953; Smith, 1984) thus their maximum pressure estimates are not valid. While disregarding the stated peak pressure of 25 kbar for Vårdalsneset, both the individual pressure estimate of > 25 kbar (no temperature estimate) and the combined set of 670–780˚C and 24–28 kbar are in broad agreeance with the previous workers.

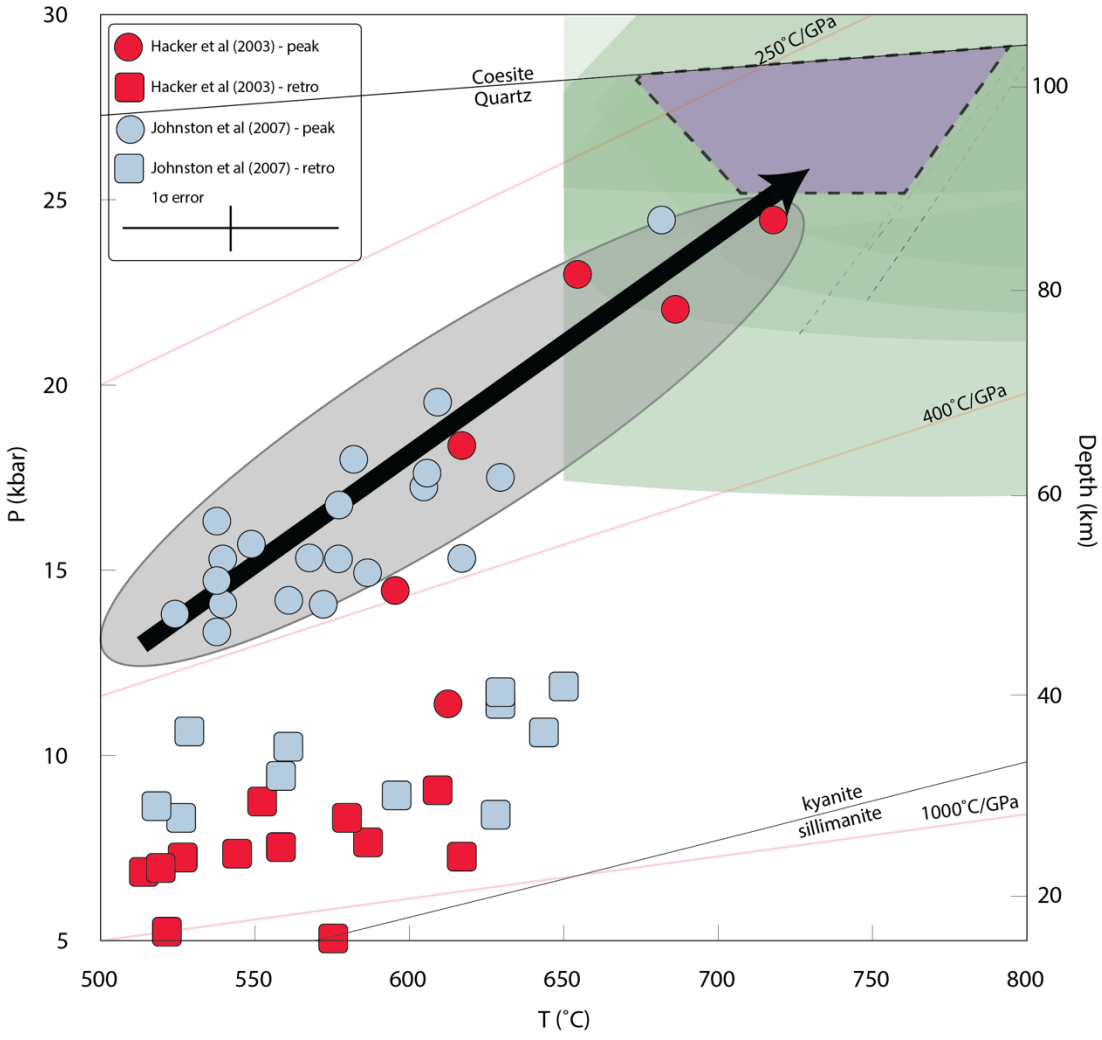

Figure 2.14: Summary of P–T information obtained by this study. Overlapping peak fields from samples WGC18-008, WGC18-011, WGC18-016, WGC18-022, WGC18-027 & WGC18-029 constrain peak conditions (purple box) reached for a large section of the southern Western Gneiss Complex. Peak and retrograde assemblages surrounding the Nordfjord–Sogn detachment taken from Hacker et al. (2003) & Johnston et al. (2007) with Western Gneiss Complex geotherm (grey bubble) approximated from this.

From data presented above it can be seen that individual pseudosections and associated models have some issues in precisely constraining *P–T* conditions within eclogitic rocks. In response to this, this study considered a variety of bulk compositions from multiple sample localities and combined their peak field distribution within *P–T* space using overlapping minor variances from sample to sample to obtain a more refined estimate of the peak conditions across a wider area.

The *P–T* conditions of the multiple eclogite bodies analysed within this study also fall along the trend of the bulk of analysed *P–T* values along southern Nordfjord–Sogn Detachment (e.g. Engvik & Andersen, 2000; Hacker et al., 2003a; Johnston et al., 2007b; Labrousse et al., 2004; Martin & Duchêne, 2015). The alignment of these *P–T* estimates are consistent with the model of a laterally continuous *P–T* gradients across Western Gneiss Complex (e.g. Hacker et al., 2010).

8.2 | Timing

Age ranges (2SE) of this study are as near as large or larger than length Scandian phase of Caledonian (~30 Ma) as such very little weight can be placed on these in precisely constraining the timing of the initiation of garnet growth within these eclogite bodies. Figure 2.13F highlights the large range of ages that these samples returned, as such we can with confidence assign their growth event to the Scandian phase of the Caledonian Orogeny but we do not ascribe any further value to them, see 8.3 for further discussion on errors and data validity.

Only a handful of Lu–Hf ages exist within the southern extent of the Western Gneiss Complex, with the majority of ages concentrated around the three UHP domains further to the north. Lu–Hf garnet–cpx–whole-rock isochrons from the Vollstein eclogite body (sample K5622A2) of Kylander-Clark et al. (2009) return ages of 410 ± 3.1 Ma while garnet–whole-rock isochrons from the Vårdalsneset body (samples NOG12 & NOG13) of Martin et al. (2010) return ages of 409 ± 12 Ma & 403 ± 13 Ma respectively. Error ranges of ages obtained by this study all fall within these previously analysed examples in the southern Western Gneiss Complex.

8.3 | Geochronology issues

High errors and MSWD in those ages of this study represent a low confidence on the precision of the ages produced. The high MSWD represent a scatter that exceeds that predicted by analytical uncertainties, thus a geological explanation could plausibly explain the spread of datapoints away from a single line along the isochron.

Various minerals including zircon, xenotime, zoisite, apatite, allanite among others are all known sequesters of REE elements in varying concentrations and such the accidental

dissolution on a micro–nanoscale of these may impart some effect on the initial garnet $^{176}Lu/^{177}Hf$ and $^{176}Hf/^{177}Hf$ ratios.

Methodology in the dissolution of mineral fractions (e.g. garnet) prior to chromatography as well as analytical procedures are designed to minimise the chance of inclusions being dissolved, see detailed discussion in Cheng et al. (2008) Vervoort and Blichert-Toft (1999); Vervoort and Patchett (1996), though other workers have suggested that microleaching may occur on a scale to effect results (Connelly, 2006). Methodologies have been suggested to further minimise the potential of this inclusion effect; e.g. annealing zircon (Connelly, 2006), selective H_2SO_4 leaching to avoid phosphate phases (Anczkiewicz, Platt, Thirlwall, & Wakabayashi, 2004; Anczkiewicz, Thirlwall, Vance, Mueller, & Villa, 2003). A detailed review on the effects of inclusions with the Lu–Hf system is presented within Scherer, Cameron, and Blichert-Toft (2000), though a discussion and examples within the context of this study are presented here forth. The exact effects are difficult to quantify without pure experimental data for each potential instance, but some generalisations and assessments can be made.

8.3.1 | Zircon

The presence of micro–nanoscale inclusions of zircon within garnet can prove problematic for geochronology within the Lu–Hf isotopic system (Connelly, 2006). Primarily this issue is centred around zircon containing large quantities of hafnium, on average 0.5–2% with up to 4% at the extreme (Hoskin & Schaltegger, 2003) with Hf a HFSE easily substituting for Zr in which it shares a nearly identical geochemistry (Kinny & Maas, 2003). The potential effect of incorporating some of this zircon held hafnium into the Lu–Hf garnet analyses and lead to the production of erroneously younger ages, trending towards less radioactive (Scherer et al., 2000). Variables in attempting to quantify this effect include initial zircon and garnet $^{176}Lu/^{177}Hf$ and $^{176}Hf/^{177}Hf$ isotopic rations, homogeneity of these ratios, initial concentrations of Hf and Lu within both zircon and garnet, ratio of volume zircon to volume of garnet fraction dissolved.

An oblate spheroidal zircon with the following parameters was chosen for this experiment; a = 20µm b & c = 15 µm with Hf concentration of 1% (10,000 ppm) and initial $^{176}Hf/^{177}Hf$ ratio of 0.2822, approximated from a CHUR composition at ~1000 Ma, with a potential source from magmatism related to the c. 1140-960 Ma Sveconorweigian orogeny (Bingen et al., 2008a; Bingen et al., 2008b; Roberts & Gee, 1985), though zircon with cores related to earlier c. 1700–1550 Gothian orogeny (Åhäll & Gower, 1997; Larson, 1996; Skår, 2000) may lower this initial $^{176}Hf/^{177}Hf$ ratio if considering a CHUR evolution. The $^{176}Lu/^{177}Hf$ ratio zircon is usually <0.0005, with this allowing the preservation of the initial $^{176}Hf/^{177}Hf$ ratio, due to

negligible addition via the ^{176}Lu to ^{176}Hf decay series (Kinny & Maas, 2003), as such absolute ^{176}Lu is treated as zero by this example.

A sample of garnet with a mass of 150 mg, similar to those used within this study chosen for this calculation, using a simplified density of ρ=4 g/cm^3 for garnet (with natural ranges 3.8–4.1 g/cm^3), equating to ~37.5mL of material. Garnet in this example represents an idealised sample from those of this study, with an initial $^{176}Hf/^{177}Hf$ ratio of 0.298 and $^{176}Lu/^{177}Hf$ ratio of 1.0. Using an approximated garnet composition of 0.5 ppm ^{177}Hf equates to 18750 ng of both ^{176}Lu and ^{177}Hf, with 4304 ng of ^{176}Hf using the above ratio, with the caveat that no other source of Lu or Hf is present for the sake of simplicity. This zircon contains approximately 251.327 ng of Hf, with this broken down into 196.013 ng of ^{177}Hf and 55.314 of ^{176}Hf, again with the caveat that no other source of Hf is present.

The resulting incorporation of the zircon into the dissolved garnet fraction prior to chromatography produces the following trends within $^{176}Lu/^{177}Hf$ + $^{176}Hf/^{177}Hf$ space, for zircon $^{176}Hf/^{177}Hf$ ratios less than garnet the shift is negative, for $^{176}Lu/^{177}Hf$ ratios the addition of zircon will always produce a negative shift due to near-zero zircon Lu content. Variations within initial $^{176}Lu/^{177}Hf$ and $^{176}Hf/^{177}Hf$ ratios of the zircon and garnet are also important in regard to both the magnitude and direction of the vector change. To quantify this change by mass for these example conditions, the addition of every 100 µg of zircon dissolved a negative shift in the order of 1.815x10^{-7} units in $^{176}Hf/^{177}Hf$ space and 1.149x10^{-5} units in $^{176}Lu/^{177}Hf$ space, as this relationship is linear it can be extrapolated to any mass of dissolution.

The above illustrates even the dissolution of a single, relatively low Hf content zircon can wreak havoc in obtaining the “correct” $^{176}Lu/^{177}Hf$ and $^{176}Hf/^{177}Hf$ ratios for a population of garnet.

8.3.2 | Epidote group

Epidote group members such as allanite and zoisite often contain abundant REE, within Allanite and related minerals REE are a structural constituents (Gieré & Sorensen, 2004). Trivalent REE are accommodated in the A sites, with the incorporation of REE^{3+} commonly charge balanced by a divalent cation (Fe^{2+}, Mn^{2+} Mg) substituted for a trivalent one in the M sites (Dollase, 1971).

Allanite is related to epidote via coupled substitution;

$$REE^{3+} + Fe^{2+} \leftrightarrow Ca^{2+} + Fe^{3+}$$

And to clinozoisite via;

$$REE^{3+} + Fe^{2+} \leftrightarrow Ca^{2+} + Al^{3+}$$

Allanite mostly favours LREE–MREE, with enrichment in the order of 50000–20000 (La to Yb chondrite normalised) found within allanite of the Dora Maira, Western Alps (Gieré & Sorensen, 2004). Chondrite-normalized REE values from an allanite bearing blueschist from New Caledonia again represent a high enrichment in LREE with 60,000 from La to Nd, decreasing smoothly without an Eu anomaly, to ~50 for Lu (Spandler, Hermann, Arculus, & Mavrogenes, 2003). Epidote group members strongly fractionate LREE from HREE with the later partitioning into garnet and zircon if present in the rock (Gieré & Sorensen, 2004; Tribuzio, Messiga, Vannucci, & Bottazzi, 1996). Though it may be noted that REE patterns for all REE epidote members are not identical, but overall trend of decreasing enrichment with increasing atomic mass is present, see Gieré and Sorensen (2004) for data and more in-depth discussion.

As a result, epidote group phases likely pose an issue for Sm–Nd systematics due to their high enrichment of LREE but are unlikely to pose an issue for Lu–Hf systematics due to their very low enrichment and concentration of HREE. Due to this and epidote group minerals are not predicted within our peak fields the accidental dissolution of epidote group members is unlikely to have been the cause of the garnet datapoint spread within the analysis of this study.

8.3.3 | Phosphate phases

Phosphate phases such as xenotime, apatite and monazite are common accessory minerals within metamorphic rocks, containing appreciable quantities of REE elements.

Monazite preferentially uptakes LREE elements (Engi, 2017; Hacker, Kylander-Clark, & Holder, 2019), thus is likely to uptake negligible Lu or Hf with its presence or accidental dissolution unlikely to affect the results of Lu–Hf systematics but are likely pose an issue for Sm–Nd systematics due to their high enrichment of LREE. Apatite is a known reservoir of Lu, containing serval thousand ppm REE overall with high Lu/Hf ratios (Engi, 2017). Exsolution of apatite has also been observed surrounding ruptured inclusions within garnet in UHP rocks (Axler & Ague, 2015; Haggerty, Fung, & Burt, 1994), particularly with high P and Ti bearing garnet.

A pair of samples from this study, WGC18-027 and WGC18-029 both contain large proportions of P_2O_5, 0.62 wt% and 0.17 wt% respectively. WGC18-027 in particular displays a particularly large spread of ($^{176}Lu/^{177}Hf$)/($^{176}Hf/^{177}Hf$) ratios for garnet points with WGC18-029 exhibiting a slightly lesser degree of spread. This higher proportion of P_2O_5 may be as a result of micro to nanoscale inclusions of a phosphate phase within the garnet.

The incorporation of apatite again shows potential to affect Lu/Hf ratios to a degree that would increase the spread away from an isochron, compromising the accuracy of the data.

8.3.4 | Garnet resorption

Some garnet within samples WGC18-008, WGC18-016 and WGC18-029 all display evidence of resorption rims with elevated levels of Ca, Fe, Mg and Mn (Figure 2.8; Figure 2.9). For one sampled garnet from sample WGC18-016 analysed by LA–ICP–MS evidence of enrichment of Lu and other HREE is present, with the pattern seemingly showing affinity with Mn, another element in which garnet preferentially uptakes. A number of studies have recognised this preferential resorption of elements that exhibit a strong compatibly with garnet (e.g. Mn and Y) when released from rims, creating annuli on high concentrations as these elements back diffuse into the relic garnet e.g. Carlson (2002); Kelly, Carlson, and Connelly (2011); Kohn (2009); Kohn and Malloy (2004); Lanzirotti (1995); Pyle and Spear (1999). In this case it is believed that Lu and other HREE elements are acting in a similar fashion to the response of Mn and Y to rim breakdown (Kelly et al., 2011).

As a result of garnet rim breakdown Lu strongly re-partitions into the garnet rim due to its strong compatibly, with limited inward diffusion (Kelly et al., 2011). Hf displays to opposite trend to Lu after rim breakdown as it partitions into surrounding phases such as zircon as a result of its incompatibility with garnet and a strong degree of fractionation between the parent ^{176}Lu and the daughter ^{176}Hf (Kohn, 2009). Lu enrichment of these rims will alter the whole garnet isotopic ratio, producing erroneous trends through increasing absolute Lu present in the grain elevating the ^{176}Lu/^{177}Hf ratio (positive shift), with the ^{176}Hf/^{177}Hf ratio likely remaining consistent with Hf lost equally into surrounding phases. This enrichment of Lu and other HREE has also been observed in garnet surrounding a contact aureole by Kelly et al. (2011) with enrichment ratios in the order of 2–5 times the initial. Similar results are observed by Martin et al. (2010) within WGC eclogites, with enrichment of Lu in garnet and partitioning of Hf into other phases producing different combinations of ages based on different minerals selected for to plot an isochron.

A detailed review on the effect of this as well as modelling to attempt to reconstruct initial ratios via resorption modelling is presented in Kelly et al. (2011). Without examining a larger range of grains that were selected for dissolution and subsequent ion exchange chromatography and ICP–MS analysis the exact magnitude of effects is difficult to quantify due to grains seeming both exhibiting and not exhibiting this effect.

8.3.4 | Rutile

Rutile is another commonly occurring phase in eclogitic and other high-pressure rocks (Korneliussen & Foslie, 1985; J. Liou, Zhang, Ernst, Liu, & McLimans, 1998; Meinhold, 2010; Zack, Kronz, Foley, & Rivers, 2002; Zhenyu, Yuchuan, Denghong, Jue, & Jianxiong, 2005). It can contain appreciable Hf, typically <5 to 120 ppm though higher concentrations

can occur and much like zircon, rutile contains near zero quantities of Lu (Meinhold, 2010). As a result of its potential for high modal abundance in eclogitic samples along with significant Hf concentrations, many times that of garnet it may play a major role in altering the true $^{176}Lu/^{177}Hf$ ratio and $^{176}Hf/^{177}Hf$ ratio in the garnet aliquots if inadvertently dissolved.

Rutile is a dominant carrier of HFSE (Foley, Barth, & Jenner, 2000; Kalfoun, Ionov, & Merlet, 2002; Zack et al., 2002). It has been observed that in eclogite samples 1 modal-% of rutile may carry more than 90% of the whole-rock content for Ti, Nb, Sb, Ta and W and considerable amounts (5–45% of the whole-rock content) of V, Cr, Mo and Sn (Rudnick, Barth, Horn, & McDonough, 2000; Zack et al., 2002). This is problematic due to the isobaric interference between W and ^{176}Hf within the mass spectrometer. If appreciable qualities of rutile via inclusions are dissolved this may alter the "true" $^{176}Hf/^{177}Hf$ value, creating a spread if different quantities of rutile in different aliquots undergo dissolution.

9. | CONCLUSION

Understudied eclogite pods within the southern section of the Western Gneiss Complex reached *P–T* conditions of 670–780˚C and 24–28 kbar during the peak of Caledonian metamorphism, equating to reaching depths of 85–100 km. These samples represent conditions within the footwall of the Nordfjord–Sogn Detachment. *P–T* conditions of the studied bodies also fall along the trend of the bulk of analysed *P–T* values along southern Nordfjord–Sogn Detachment (Engvik & Andersen, 2000; Hacker et al., 2003a; Johnston et al., 2007b; Labrousse et al., 2004). The alignment of these values further validates the idea of relatively homogenous subduction and exhumation of the Western Gneiss Complex, in keeping with similar *P–T* gradients found within the UHP domains and along the paleo-subduction path further to the north.

The difficulties of obtaining precise *P–T* data for eclogites is again highlighted within this study, with large peak fields and very low mineral compositional variance. The further development and application of raman spectroscopy based thermobarometry ("thermoba-raman-try") e.g. Angel, Mazzucchelli, Alvaro, Nimis, and Nestola (2014); Angel, Nimis, Mazzucchelli, Alvaro, and Nestola (2015); Kohn (2014); Mazzucchelli et al. (2018), may aid in the rapid collection of precise datasets allowing for a multi-method approach in constraining the conditions of formation.

Lu–Hf ages obtained by this study do not provide any significant improvement or produce any additional information to those (Lu–Hf ages) previously produced by other workers, (Carswell et al., 2003a; Cutts & Smit, 2018; Griffin & Brueckner, 1980; Hacker et al., 2010; Jamtveit et

al., 1991; Martin et al., 2010; Mearns, 1986; Mørk & Mearns, 1986) with the ages of this study sitting within broad agreeance.

There are a number of potential reasons for the high MSWD and spread in garnet points, with a review on inclusion related effects presented above, illustrating the massive potential for the nano–microscale inclusion effect especially with initially low REE concentration garnets such as those of this study. Further work, e.g. TEM and/or Atom Probe is required to assess distribution of REE in garnet to provide a better understanding on a fundamental level on how these elements distribute and potential implications for geochronology. Investigating the intergrowth of nano–micro scale inclusions of accessory and REE bearing phases within minerals selected for dissolution and chromatography would also be pertinent.

3. DEVIATIONS FROM THE NORM: A CASE FOR DEFORMATION-ENHANCED HEATING DURING EXHUMATION OF THE WESTERN GNEISS COMPLEX, NORWAY.

1. | INTRODUCTION

Low angle normal faults and shear zones (or extensional detachments) are a long-recognised component in the exhumation of material from the core of orogenic belts during the waning stages of an orogen (Crittenden, Coney, & Davis, 1980; Lister & Davis, 1989). Extensional detachments are also proposed as a way to accommodate the exhumation of high pressure (HP) and ultrahigh-pressure (UHP) rocks from subduction zones as part of a larger orogenic system, e.g. the ~1800 km Scandinavian Caledonides (Andersen, 1998; Fossen & Dunlap, 1998; Johnston et al., 2007a) and The Alps (Campani, Herman, & Mancktelow, 2010; Froitzheim & Eberli, 1990; Ratschbacher, Frisch, Neubauer, Schmid, & Neugebauer, 1989; Reddy, Wheeler, & Cliff, 1999). These extensional detachments are unlikely to be entirely brittle structures due to their depths of propagation and high temperatures decreasing crystal-plasticity (Scholz, 1988; Sibson, 1977; Stipp, Stünitz, Heilbronner, & Schmid, 2002). Instead they are likely to form large brittle-ductile shear zones with large degrees of movement in the lower to mid-crust (Fossen & Cavalcante, 2017).

Shear-localisation in these instances can be rapid, with strain localisation taking place in as little as 1 Myr, with a dormant weak zone existing for upwards of 100 Myr (Bercovici & Ricard, 2012; Fossen & Cavalcante, 2017), making it possible to rapidly move material and increase heat production within and around these shear zones (Brun & Cobbold, 1980; Duprat-Oualid & Yamato, 2017; Mako & Caddick, 2018). The heat produced in these situations through mechanical work, moving terrane sized volumes of rock can greatly exceed heat produced through radiogenic heat production, greatly increasing the thermal budget of the system and elevating geothermal gradients (Mako & Caddick, 2018; Nabelek, Whittington, & Hofmeister, 2010). This increased heat production may also lead to an inverted metamorphic field gradient (Anczkiewicz, Chakraborty, Dasgupta, Mukhopadhyay, & Kołtonik, 2014; Duprat-Oualid & Yamato, 2017; Duprat-Oualid, Yamato, & Pitra, 2013; Molnar & England, 1990). Thus shear heating is commonly invoked as a mechanism to produce large amounts of heat within orogenic systems, in a variety of tectonic settings (England & Molnar, 1993).

The application of geodynamic modelling to a wide variety of geological settings has allowed the testing of differing hypotheses; with attempts to explain the tectonic processes behind observations in the rock record (Beaumont et al., 2009; Burov et al., 2014b; Duretz et al., 2012; Gerya & Stöckhert, 2006; Sizova et al., 2012; Warren et al., 2008b). Modelling by a number of authors (Burg & Gerya, 2005; Grasemann & Mancktelow, 1993; Mako & Caddick, 2018; Nabelek et al., 2010; Platt, 2015; Souche, Medvedev, Andersen, & Dabrowski, 2013) suggest that mechanical heating may provide an additional and not insignificant heat source around these crustal shear zones. The results of these models suggest the additional heating may result

in temperature increases in the order of 30–120˚C (Duprat-Oualid & Yamato, 2017; Mako & Caddick, 2018; Platt, 2015; Schmalholz & Duretz, 2015; Souche et al., 2013), with these results depending on a number of factors including; strain rate, deviatoric stress, slip rate, thermal diffusivity, shear zone width and rock rheology (Clark, Fitzsimons, Healy, & Harley, 2011; Mako & Caddick, 2018; Nabelek et al., 2010; Platt, 2015)

The focus of this study, the Hyllestad Complex, consists of interlayered aluminous schists, amphibolites and gneisses of the Middle Allochthon (Tillung, 1999) or Upper Allochthon (Chauvet & Dallmeyer, 1992; Swensson & Andersen, 1991). These lie unconformably on the Western Gneiss Complex, separated by the Nordfjord–Sogn detachment, a large-scale extensional shear zone, Caledonian in age and over 100 km in length (Hacker et al., 2003a). The current architecture of the Caledonides (Figure 3.1) was developed during the c. 430–400 Ma Scandian Orogeny, part of the wider Caledonian Orogeny occurring as a result of the westwards underthrusting of Baltica beneath Laurentia (Gee, 1975; Roberts, 2003; Roberts & Gee, 1985). The activation of Nordfjord–Sogn detachment zone is inferred to have played an integral role in the exhumation of the rocks of the Western Gneiss Complex from (ultra)high-pressures during the termination of the Scandian Orogeny (Eide et al., 1997; Johnston et al., 2007a; Norton, 1987). The proximity of the Hyllestad Complex to the NSD make them the ideal candidates to investigate whether evidence of shear heating can be observed/recorded by metamorphic assemblages.

In this study we undertake a multi-faceted approach, including integrated petrochronology (Engi, Lanari, & Kohn, 2017; Kylander-Clark, 2017), phase diagrams for equilibrium bulk rock compositions (*P-T* pseudosections; (Powell & Holland, 2008) assessing the *P–T–t–d* evolution of the rocks and place them within the already well-defined thermal framework for the Caledonian Orogen in western Norway (Cutts & Smit, 2018; Cutts et al., 2019a; Hacker et al., 2010; Hacker & Gans, 2005; Roberts, 2003; Walsh et al., 2013; Young, 2017)

2. | GEOLOGICAL SETTING

2.1 | Tectonic and metamorphic events

The tectonostratigraphy of the Scandinavian Caledonides predominately formed during the c. 430–400 Ma Scandian Orogeny, as part of the wider Caledonian Orogeny (Gee, 1975; Roberts & Gee, 1985), though some pre-Scandian phases events are preserved, see Roberts (2003). It occurred as a result of the westwards underthrusting of Baltica (Europe) beneath Laurentia (Greenland & North America), following the closure of the Iapetus Ocean (Gee, 1975; Roberts & Gee, 1985). The initiation of the continent-continent collision occurred as early as c. 430 Ma with the cessation of subduction and oceanic related magmatism (Andersen & Jamtveit, 1990; Corfu et al., 2006; Slagstad & Kirkland, 2018; Torsvik & Cocks, 2005) and continued

through 415–408 Ma in the Upper and Middle Allochthon (Fossen & Dunlap, 1998; Hacker & Gans, 2005), reaching (U)HP depths (>80–120 km) in the Western Gneiss Complex ~410 to 400 Ma (Hacker et al., 2010; Krogh et al., 2011; Kylander-Clark et al., 2008; Terry et al., 2000).

The collision resulted in the creation of allochthonous nappe stacks via intense shortening, thrusting exotic (Uppermost Allochthon), outboard oceanic terranes (Upper Allochthon) and portions of the overriding Laurentian plate along with outboard Baltic-continental material (Middle and Lower Allochthons) along major thrusts (e.g. Jotun Main Basal Thrust) onto the Baltic hinterland of Precambrian crystalline rocks . Deeper Baltic segments reached UHP conditions forming coesite within eclogites and rare microdiamond in surrounding gneiss (Dobrzhinetskaya et al., 1995; Smith, 1984). A continuous increase in the peak *P–T* conditions extends westwards across the Western Gneiss Complex, indicative of the coherent nature of the subduction and subsequent exhumation of the Western Gneiss Complex (Andersen et al., 1991; Carswell et al., 2006; Cuthbert et al., 2000; Hacker et al., 2010).

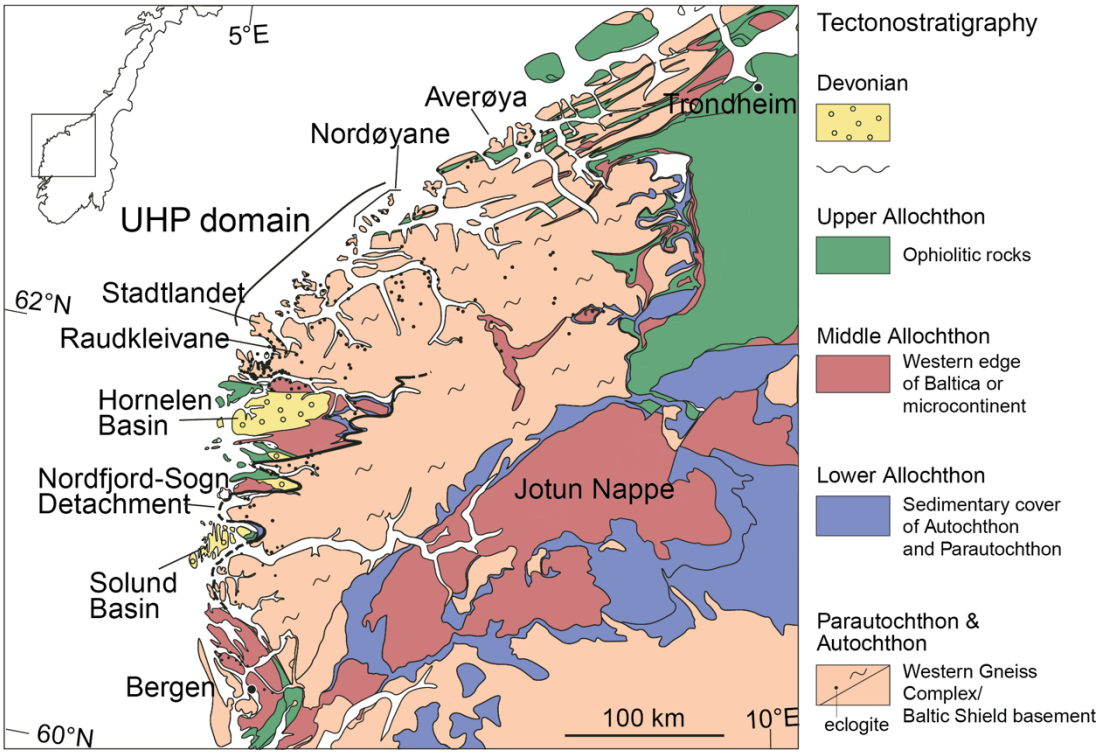

Figure 3.1: Teconostratigraphy of SW Norway, eclogite occurrences indicated by dot. Modified from (Walsh et al., 2007)

Extensional tectonics at the end of the Scandian Orogeny are inferred to have played a key role in the exhumation of the Western Gneiss Complex and overlying allochthons and nappes (Andersen, 1998; Roberts, 2003), with a rapid change from convergence to divergence over a period of ~4–6 Ma (Fossen & Dunlap, 1998). Extension commenced as early as c. 410 Ma at

higher structural levels, with major extension occurring c. 405 to 400 Ma (Hacker et al., 2003a; Roberts, 2003). This resulted in rapid denudation and exhumation of these (U)HP rocks (Andersen, 1998; Fossen, 1992; Tucker et al., 2004). Initial reverse movement along the main basal thrust occurred (Mode-I in Fossen, 1992) with subsequent late extension (Mode-II) accommodated through top W movement along SE trending detachments (Fossen, 1992; Hacker et al., 2003a; Johnston et al., 2007b). Extension was also key in developing the current structure of the Scandinavian Caledonides with large detachment faults (eg. Nordfjord–Sogn, Hornelen etc.), juxtaposing stratigraphy with radically differing *P–T* histories (Hacker et al., 2003a; Johnston et al., 2007a; Johnston et al., 2007b), along with creating space for the deposition of Devonian-Carboniferous sediments in supradetachment basins (Andersen, 1998; Norton, 1987; Young et al., 2011).

2.2 | Solund–Hyllestad area geology

The Solund–Hyllestad area contains a mix of Devonian sediments of the Solund Basin, the allochthonous Hyllestad Complex separated at the base from para-autochthonous Western Gneiss Complex by the Nordfjord–Sogn detachment (Figure 3.2).

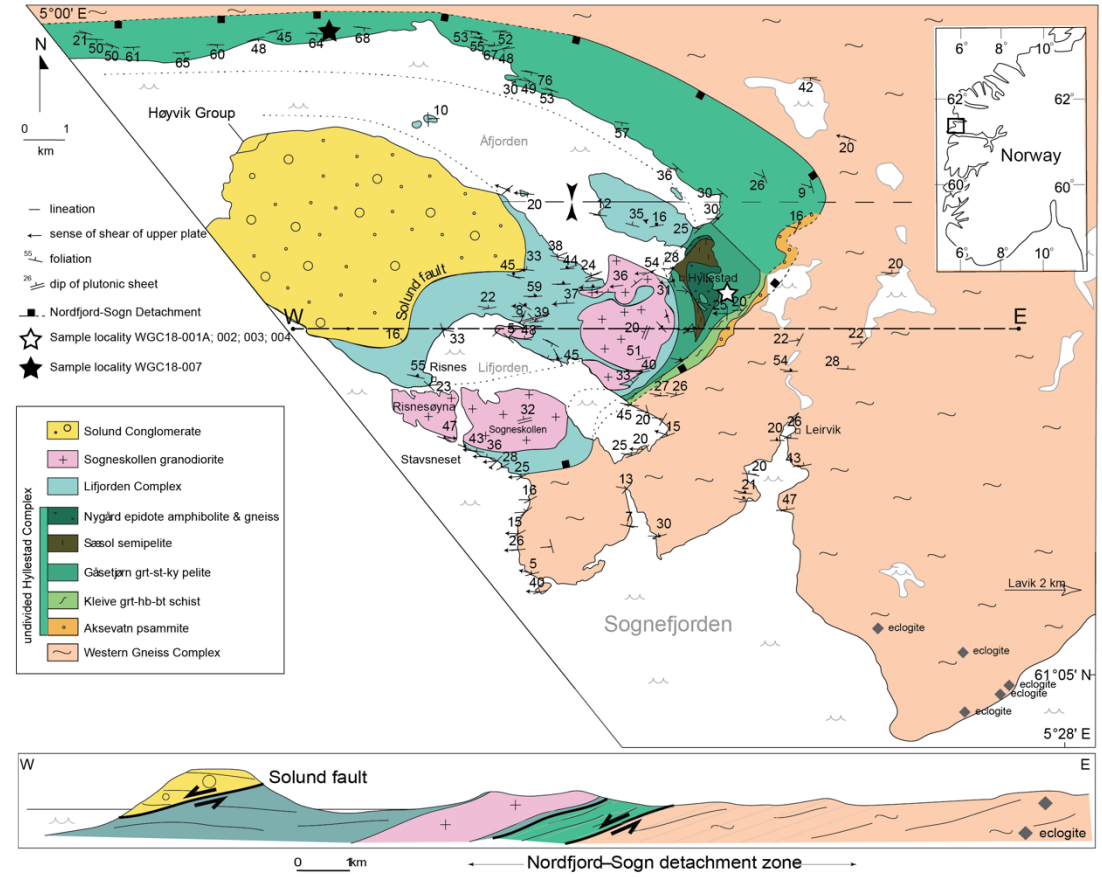

Figure 3.2: Hyllestad area geology, modified from Hacker et al. (2003)

The Solund conglomerate of the Solund Basin is up to 6km thick and consists of predominantly proximally sourced Devonian age conglomerates and sandstones unconformably overlying the

Lifjorden Complex, truncated at the base by the west dipping Solund Fault (Hacker et al., 2003a; Hossack, 1984; Nilsen, 1968). The c. 434 Ma Sogneskollen granodiorite intrudes into the Lifjorden Complex as a 300 m thick sheet dipping 20˚ west (Hacker et al., 2003a; Skjerlie, Pedersen, Wennberg, & De La Rosa, 2000). The Hyllestad Complex lies unconformably on top of the Western Gneiss Complex, separated by the Nordfjord–Sogn detachment (Hacker et al., 2003a). The Hyllestad Complex is subdivided into the Aksevatn psammite, Kleive mafic schist, Gåsetjørn pelite, Sæsol semipelite and the Nygård amphibolite (Hacker et al., 2003a; Tillung, 1999). It has been correlated to either; the Lower Allochthon (Chauvet, Kienast, Pinardon, & Brunel, 1992; Swensson & Andersen, 1991) or the Høyvik Group of the Middle Allochthon (Tillung, 1999), both of which display highly aluminous pelites. In the Hyllestad area, the Western Gneiss Complex is a mix of granitic to gabbroic orthogneiss with minor mafic lenses of eclogite (Hacker et al., 2003a) that occur as variably sized pods and lenses of mafic material (Engvik, Austrheim, & Andersen, 2000; Walsh et al., 2007).

2.3 | Nordfjord–Sogn detachment

The Nordfjord–Sogn detachment zone is a large-scale extensional brittle-ductile shear zone, over 100 km in length, Caledonian in age and preserves greenschist-amphibolite facies overprinting and assemblages (Eide et al., 1997; Labrousse et al., 2004; Norton, 1986, 1987). Within the Hyllestad area it separates the Hyllestad Complex in the hanging wall from the Western Gneiss Complex in the footwall (Hacker et al., 2003a). A 3–5 km thick layer of brittle-ductile mylonites deform the area surrounding the detachment (Andersen & Andresen, 1994; Andersen & Jamtveit, 1990; Hacker et al., 2003a)

3. | METHODS AND ANALYTICAL TECHNIQUES

3.1 | Whole rock compositions

Samples sent for whole rock geochemistry were cut from rock directly adjacent to thin section blocks to provide the best approximation of thin section composition. The bulk major element compositions of the samples were measured by x-ray fluorescence (XRF) at Franklin and Marshall College, Pennsylvania using a PANalytical 2404 X-ray fluorescence vacuum spectrometer by fusing 0.4000g of sample with 3.4000g of lithium tetraborate. Major oxides; SiO_2, Al_2O_3, CaO, K_2O, P_2O_5, TiO_2, total iron (Fe_2O_3T), MnO, Na_2O and MgO along with selected trace elements were measured by XRF. FeO/Fe_2O_3 was measured by titration, while H_2O was measured through loss on ignition (LOI) by heating the sample to 900–950˚C for 60 minutes.

3.2 | EMPA

Electron microprobe analysis was conducted to determine quantitative mineral compositions and obtain elemental maps at Adelaide Microscopy, University of Adelaide using a Cameca

SXFive Electron Microprobe equipped with 5 tuneable wavelength-dispersive spectrometers running Probe for EPMA software. A 15 KeV acceleration voltage, 20 nA beam current with 2 μm defocused beam size was used for each mineral composition analysis, at an average of 90 seconds per analysis. The following suite of elements was acquired: Cl, Ca, K, Ba, F, Ti, P, Na, Si, Mg, Al, Fe, Mn, Cr, Zn, and Ni, oxygen was calculated by stoichiometry, assuming that all Fe was Fe^{2+}. Calibration was to a wide range of synthetic and natural standards within Probe for EPMA software, with the software used to convert CPS to wt%. A full list of natural and synthetic standards used for data standardisation and more detailed methodology is presented in Appendix B. Elemental maps were acquired with a 15 KeV acceleration voltage, 200 nA beam current with a 2–5 μm defocused beam size varying between samples. Data is presented in Supplementary Data 1.

3.3 | Phase equilibria modelling

Pseudosections were calculated using whole rock compositions obtained by XRF to determine the pressure-temperature evolution of the samples. Calculations were undertaken using THERMOCALC 3.40i (Powell & Holland, 1988), for samples WGC18-002, WGC18-003 and WGC18-004 in the MnO–NaO–CaO–K_2O–FeO–MgO–Al_2O_3–SiO_2–H_2O–TiO_2–O (MnNCKFMASHTO) system, using DS6.3, a modified version of the Holland and Powell (2011) dataset. The a-X models used are as follows: garnet, biotite, staurolite, chlorite, chloritoid, ilmenite (White et al., 2014b); muscovite, paragonite (White, Powell, Holland, Johnson, & Green, 2014a); plagioclase (Holland & Powell, 2003); diopside (Green et al., 2016). H_2O was set in excess, and the measured FeO was obtained by titration. Peak fields were determined through petrological analysis of samples. Mineral abbreviations used follow the standard of Whitney and Evans (2010).

Whole pseudosections were contoured within TCInvestigator 2.0 (Pearce et al., 2015) using THERMOCALC 3.40i in MnNCKFMASHTO system, using DS6.3 with a-X models as above. Si-in-phengite contours for peak fields were contoured using THERMOCALC 3.40i, using the relationship of: Si average-per-formular-unit Si(a.p.f.u) = 3 + (1 – y(mu)), with y(mu) the XAlM2a site fraction, the margarite c(mu) component was ignored as Ca is negligible in these samples and high pressure rocks with Si-in-phengite proven to be an effective barometer at high pressures < 22 kbar (Massonne & Schreyer, 1987).

3.4 | Laser Ablation inductively coupled plasma mass spectrometry (LA–ICP–MS)

Analysis of accessory minerals were conducted by either *In-situ* by Split Stream LA–(MC)–ICP–MS or by LA–ICP–MS at the GeoHistory Facility of the John de Laeter Centre, Curtin University. Analytical spot locations were identified through TIMA phase maps and optical microscopy.

3.4.1 Monazite

Instrumentation in the GeoHistory Facility consisted of an ASI RESOlution M-50A-LR, incorporating a Compex 193nm Ar-F excimer laser attached to a Agilent 8900 triple quadrupole. Monazite analyses were conducted at a laser repetition rate of 6 Hz with a 10 μm at 26% beam attenuation leading to a fluence of ~2 J/cm2. The following sequence of: two cleaning pulses, a long initial background collection of 40 s, followed by 40 s of ablation, and 15 s of washout time was repeated for each analysis. Laser gas flow of 320 ml/min He, and 1.2 ml/min N were used with mass spec argon gas flow of ~1 l/min on the Agilent 8900 QQQ.

Monazite standards; 44069; 424.9 ± 0.4 Ma (Aleinikoff et al., 2006), India (505 ± 5 Ma; Korhonen, Saw, Clark, Brown, & Bhattacharya, 2011; Taylor et al., 2014), Stern (Stern & Berman, 2001), Trebilcock (272 ± 2 Ma; Tomascak, Krogstad, & Walker, 1996) and VK1 (Fletcher, McNaughton, Davis, & Rasmussen, 2010) were inserted into the run, bracketing every 22 unknowns. Time resolved series data was processed in Iolite software (Paton et al., 2011; Paton et al., 2010), with U–Pb data reduced using the U_Pb_Geochronology4 data reduction scheme following Paton et al. (2011). Monazite U–Pb age calculation was standardised against the standard 44069, while India, Stern, Trebilcock and VK1 were treated as secondary standards for the purpose of QC. Data is presented in Supplementary Data 3.

3.4.2 Rutile

The same laser instrumentation as above was used but instead was attached in Split Stream (LASS) mode (Kylander-Clark, Hacker, & Cottle, 2013) to a Nu-Plasma2 HR multi-collector ICP and Agilent 8900 triple quadrupole ICP to enable simultaneous in situ U–Pb and trace element collection. The Nu-Plasma2 was set up to collect U, Th, Pb and Hg peaks using high sensitivity ion counters. The Agilent 8900 quadrupole was set up to monitor trace elements for 0.03 s; ^{24}Mg, ^{27}Al, ^{28}Si, ^{44}Ca, ^{45}Sc, ^{49}Ti, ^{51}V, ^{52}Cr. ^{57}Fe, ^{60}Ni, ^{63}Cu, ^{66}Zn ^{88}Sr, ^{89}Y, ^{90}Zr, ^{93}Nb, ^{95}Mo, ^{118}Sn, ^{121}Sb, ^{178}Hf, ^{181}Ta, ^{182}W, ^{204}Pb, ^{206}Pb, ^{207}Pb,^{208}Pb, ^{232}Th, ^{238}U.

Rutile analyses were conducted at a laser repetition rate of 4 Hz at a 50 μm spot size, and at a 26% beam attenuation leading to a fluence of ~2 J/cm^2. The following sequence of: two cleaning pulses, a long initial background collection of 40 s, followed by 35 s of ablation, and 15 s of washout time was repeated for each analysis. Laser gas flow of 320 ml/min He, and 1.2 ml/min N were used with matched mass spec argon gas flow of ~1 l/min on both the Nu Plasma II and Agilent 8900 QQQ. Rutile age standards: R10, R19, and secondary standards N15, BCR, BHVO and TIG were inserted into the run, bracketing every 15 unknowns

Time resolved series data was processed in Iolite software, U–Pb data for rutile was reduced using the U_Pb_Geochronology4 data reduction scheme following Paton et al. (2011). Rutile

U–Pb calculation was standardised against the standard R10, with R19 used as a secondary age standard to assess accuracy of U–Pb analysis, with calculated values of R19 falling within the acceptable limits of the published value. Rutile trace element calibration was conducted against the internal reference isotope ^{47}Ti, by standardising against the known stoichiometric ratio of titanium (59.94 wt%) within the unknowns against the standards R10 and BHVO using the TraceElements_SI DRS within Iolite. Data is presented in Supplementary Data 4.

3.4.3 Zr-in-Rutile Thermometry

Zirconium content within rutile was obtained from data collected by the Agilent 8900 quadrupole (Supplementary Data 4), see 3.4.2 for collection methodology. The temperature calculation was based the calibration of Tomkins, Powell, and Ellis (2007), with pressure values for the calculation obtained from peak fields within *P–T* pseudosections.

4. | SAMPLE DESCRIPTIONS

Samples come from a series of low roadside outcrops in the Hyllestad area, proximal to the Nordfjord–Sogn detachment. These were chosen due to their proximity to the detachment along with the presence of metamorphic and accessory minerals that would allow for phase equilibria modelling and geochronology.

4.1 | Sample WGC18-001A

Garnet occurs as large subhedral porphyroblasts, ranging 2500–8000 μm in size, partially replaced along fractures and the margins by chlorite with inclusion rich cores of quartz, minor rutile and ilmenite. Garnet porphyroblasts have well-defined strain shadows of recrystallised quartz and chlorite, with chlorite forming as elongate to fibrous grains around grain boundaries and infilling cracks, strain caps occur within the quartz-muscovite-chlorite fabric. Kyanite containing inclusions of quartz occurs as elongate porphyroblasts wrapped by the muscovite fabric, with grains ranging from 200–2000 μm in size, fine fibrous sillimanite replaces kyanite boundaries. Chloritoid occurs as large 2000–3000 μm anhedral porphyroblasts to small blocky euhedral grains <200 μm. Large porphyroblasts are corroded with rim replacement occurring within the quartz-muscovite fabric, small porphyroblasts exhibit little replacement and occur aligned within the quartz-muscovite fabric. Muscovite, paragonite and quartz form the dominant fabric within the sample, muscovite occurs as foliated masses with intergrown paragonite or bunches of medium–fine grains and anhedral quartz grains <20–500 μm defining a foliation throughout the section. Rutile and ilmenite occur as elongate–bladed grains predominately aligned within the foliated muscovite–quartz matrix, with ilmenite commonly overgrowing rutile. Rutile grains range in size from <20 μm overgrowths up to 400 μm singular

grains, ilmenite grains are usually larger ranging from <20–800 μm. Monazite grains range in size <20–300 μm aligned within the muscovite-quartz fabric.

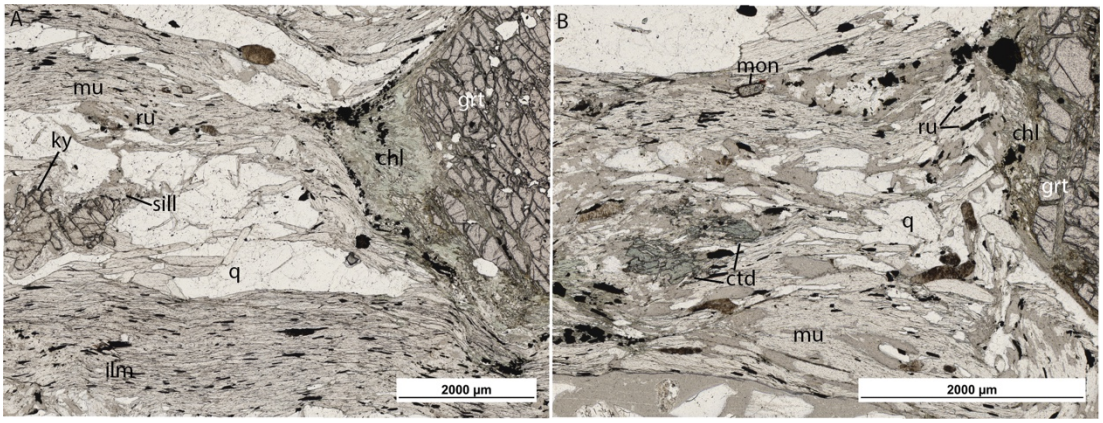

Figure 3.3: Sample WGC18-001A; A) Large garnet porphyroblast heavily fractured with chlorite growing around and within strain shadow, kyanite porphyroblast with rim polymorphed by fine grained sillimanite; B) Chlorite surrounding garnet porphyroblast, chloritoid grains exhibiting signs of breakdown, large elongate monazite grains aligned within sample fabric.

4.2 | Sample WGC18-002

Garnet occurs as large subhedral porphyroblasts, ranging in size between 2500–7000 μm, larger porphyroblasts display boundary replacement by quartz along with quartz inclusions, smaller porphyroblast display a more well-formed habit. Garnet porphyroblasts have well-defined strain shadows of recrystallised quartz and chlorite, with chlorite forming as elongate to fibrous reaction textures around grain boundaries and infilling cracks and strain caps surround the porphyroblast. Kyanite predominantly occurs as subhedral porphyroblasts, ranging in size and appearance, elongate to stubby-blocky grains (4000–8000 μm) and blocky shaped grains (500–1000 μm) oriented within the fabric. Some larger porphyroblasts exhibit a poikioblastic texture with inclusions of quartz and rutile/ilmenite, along with quartz recrystallisation textures around grain boundaries. Very fine fibrous sillimanite occurs around the margins of kyanite, polymorphing kyanite. Staurolite occurs from subhedral, well formed (200–300 μm) to anhedral poorly formed (200–2000 μm), blobby-stringy habits with cracking and pitting. The majority of staurolite occurs as porphyroblasts aligned within the quartz-muscovite-paragonite fabric, with a small number of well-formed subhedral porphyroblasts included within garnet rims. Minor chloritoid exists as small euhedral blocky grains aligned within the matrix of the sample, grain sizes range between 100–200 μm. The sample matrix consists of quartz and muscovite–paragonite grains preserving a foliation wrapping the large garnet and kyanite porphyroblasts, fine-scale anastomosing shear bands occurring in areas of fine, bladed muscovite and paragonite. Muscovite occurs as fibrous-needle like grains in alignment across the sample with intergrown blades of paragonite, forming sporadic bands

1000–2000 µm, undulating around quartz layers 2000-3000 µm. Ilmenite and rutile occur in an aligned with the fabric, with rutile often overgrowing larger ilmenite grains forming rims. Monazite occurs aligned within the foliated muscovite-quartz fabric of the sample or in textural association with garnet, ranging from 20–300 µm in size.

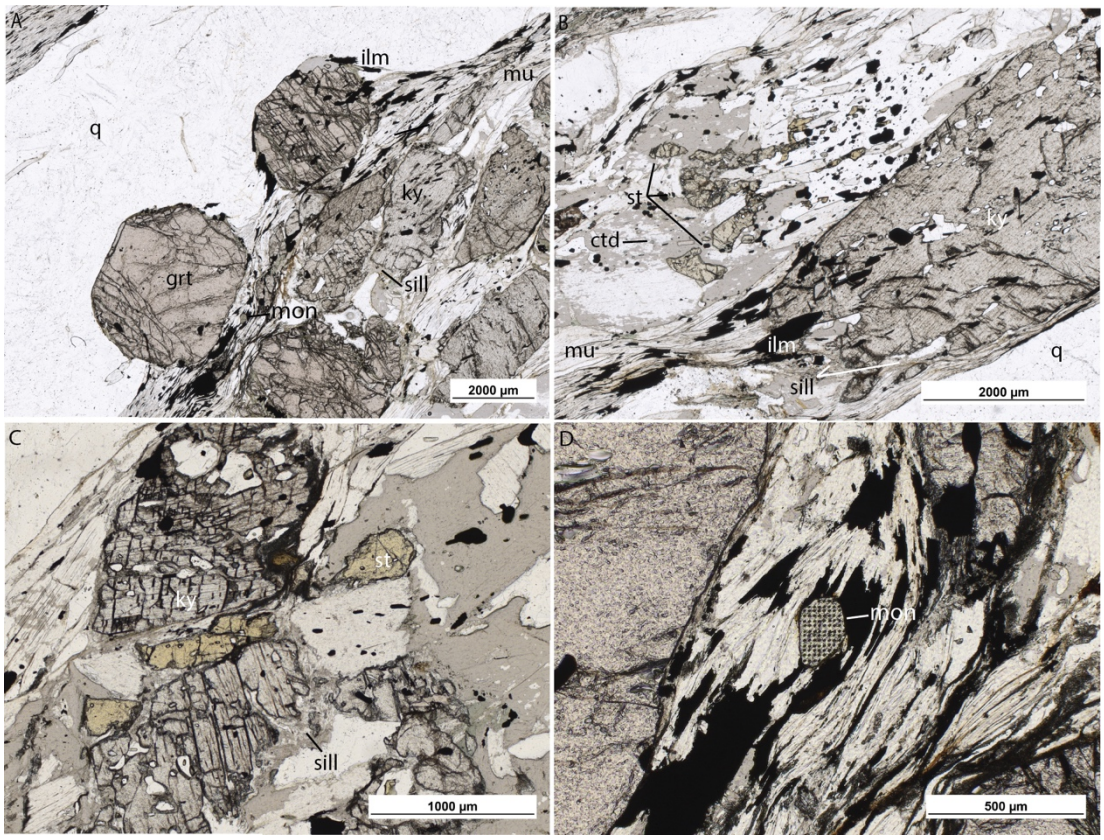

Figure 3.4: Sample WGC18-002; A) Large garnet and staurolite porphyroblast within aligned quartz-muscovite-paragonite fabric; B) Blebby staurolite grains, with fine chloritoid grains exhibiting signs of breakdown, kyanite porphyroblast rim polymorphed by fine grained sillimanite; C) Large staurolite grains surrounding kyanite porphyroblast with rim polymorphed by fine grained sillimanite; D) Large monazite within quartz-muscovite-paragonite fabric.

4.3 | Sample WGC18-003

Garnet forms large subhedral porphyroblasts, between 1000–5000 µm in size, larger porphyroblasts contain inclusion rich cores of quartz, with minor muscovite, rutile, ilmenite and monazite throughout. Inclusions within the core display minor alignment of quartz at orientations oblique to the primary foliation, with the outer of the core preserving a syn-tectonic fabric, truncated by the (near) inclusion-less outer rim. Strain caps and shadows form around these porphyroblasts, with strain shadows containing quartz along with aligned fine-grained chlorite as a reaction texture. Kyanite occurs as 2000–5000 µm subhedral blocky-elongate porphyroblasts, displaying a poikioblastic texture of quartz, minor rutile and monazite. Grain boundaries display very fine fibrous sillimanite polymorphing kyanite.

Staurolite porphyroblasts, 100–400 µm in size, occur as both subhedral well-formed grains to anhedral and corroded grains Chloritoid occurs in low abundance as small blocky grains predominately within the aligned quartz-muscovite matrix. Quartz, muscovite and paragonite preserve a foliation wrapping the large garnet and kyanite porphyroblasts displaying minor banding. Muscovite ranges from larger flat sheet like grains to smaller needle-elongate grains, with intergrown paragonite of a similar texture, quartz ranges from fine <50 µm to large 1000 µm grains primarily occurring around garnet porphyroblasts. Rutile occurs ranging from large 300 µm blocky, irregular shaped grains to smaller 20–50 µm blocky to elongate to small stringy <20 µm grains. These occur primarily aligned within foliated fabric, several rutile grains exhibit ilmenite overgrowths, with both rutile and ilmenite exhibiting magnetite/hematite overgrowth. Monazite varies in size ranging from small <20 µm to large 300 µm grains, occurring within the inclusion rich garnet core, rim as well as aligned within the aligned quartz-muscovite fabric.

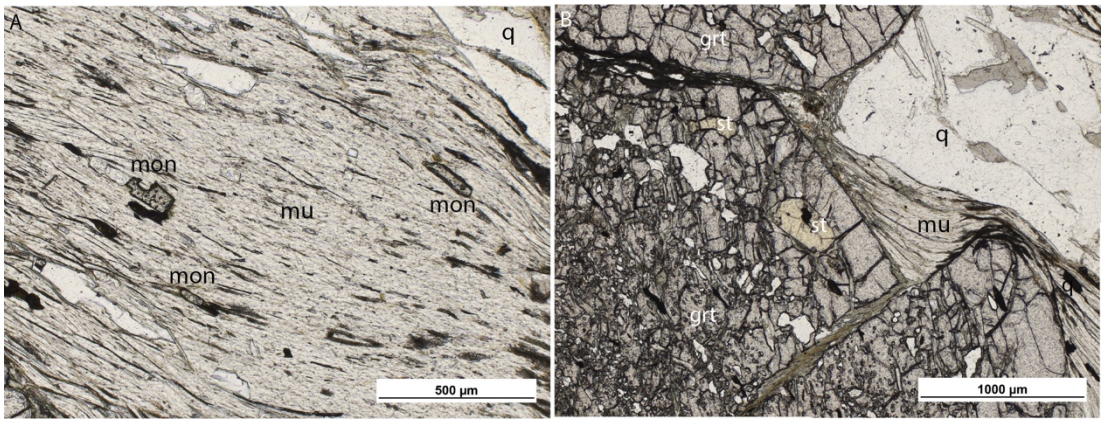

Figure 3.5: Sample WGC18-003; A) fine elongate monazite aligned within the quartz-muscovite-paragonite fabric; B) Staurolite inclusions within quartz inclusion heavy core of garnet, muscovite-paragonite fabric wrapping large garnet porphyroblasts.

4.4 | Sample WGC18-004

Garnet occurs as large subhedral porphyroblasts, 4000–10000 µm in size, heavily fractured containing abundant inclusions with rutile–magnetite/haematite trails curving in a syn-kinematic with the outer rim. Chlorite grows heavily within cracks and along grain boundaries as a reaction texture, as well within strain shadows alongside recrystalised quartz with some evidence of strain capping preserved within the fabric. Heavily fractured kyanite porphyroblasts 1000–4000 µm in size occur with minor alignment within the sample fabric, minor inclusions of quartz, muscovite and rutile are present. Porphyroblast boundaries are heavily corroded and damaged, with very fine hair-like sillimanite polymorphic replacement. Anhedral 500–1000 µm staurolite grains occur aligned within the matrix of the sample, with minor sympletic overgrowth along some boundaries. Hornblende occurs across the sample in

a large range of grain sizes and textures, large grains 4000–6000 µm form much of the foliated fabric. Very fine grained <100 µm hair-like blades intergrow within these larger grains as well as surrounding garnet, kyanite and staurolite porphyroblasts. Fine grained muscovite sheets, 100–1000 µm in size grow surrounding kyanite and garnet porphyroblasts, with a bladed texture intergrown with the matrix hornblende. Fine grained blebby–stringy rutile with magnetite/haematite overgrowths, 50–400 µm in size occur aligned as tracks within the fabric of the sample.

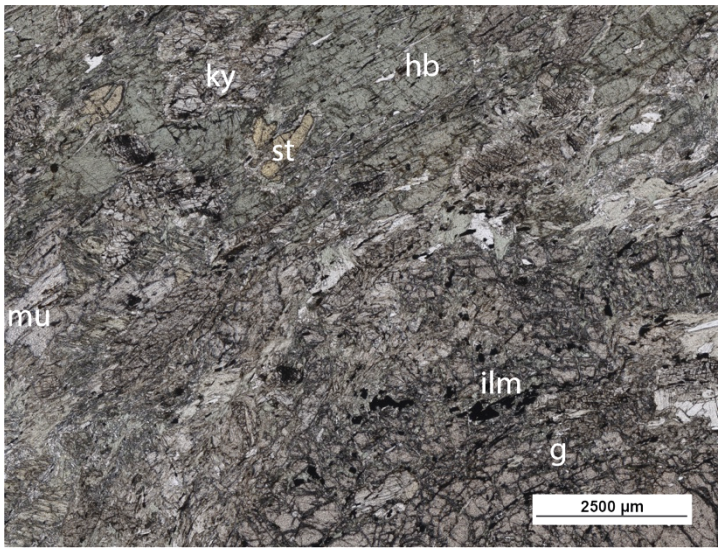

Figure 3.6: Sample WGC18-004; pervasive hornblende across sample, with muscovite, quartz and staurolite in groundmass. Large garnet porphyroblasts heavily cracked and altered.

4.5 | Sample WGC18-007

Garnet occurs as large subhedral porphyroblasts, 2000–5000 µm, with corroded and altered grain boundaries in conjunction with abundant fractures. Larger porphyroblasts contain an inclusion rich core of aligned muscovite and quartz grains, with some porphyroblasts containing inclusions of chloritoid within the rims. Chlorite grows primarily within the strain shadows of porphyroblasts, also the strain shadows also contain recrystallised quartz. In addition, chlorite also occurs along fractures penetrating to the garnet core. Garnet grains exhibits δ tails, with fine shear bands (<50 µm) defined by muscovite, sillimanite and biotite (Figure 3H). Anhedral kyanite porphyroblasts <3000 µm in length, with fragments <400 µm. Kyanite contain inclusions of aligned quartz, rutile and ilmenite. The margin of the kyanite grains are corroded and replaced by quartz, muscovite and chlorite. Fine-grained fibrous sillimanite networks polymorph the margins of some kyanite grains. Subhedral, blocky to elongate chloritoid porphyroblasts 200–800 µm occur oriented within the fabric predominantly occurring within the matrix or as inclusions within the rims of garnet porphyroblasts. Rutile occurs with ilmenite overgrowths alongside ilmenite grains aligned within the quartz-

muscovite fabric. Both rutile and ilmenite form aligned trails within both the matrix and as inclusions trails within kyanite.

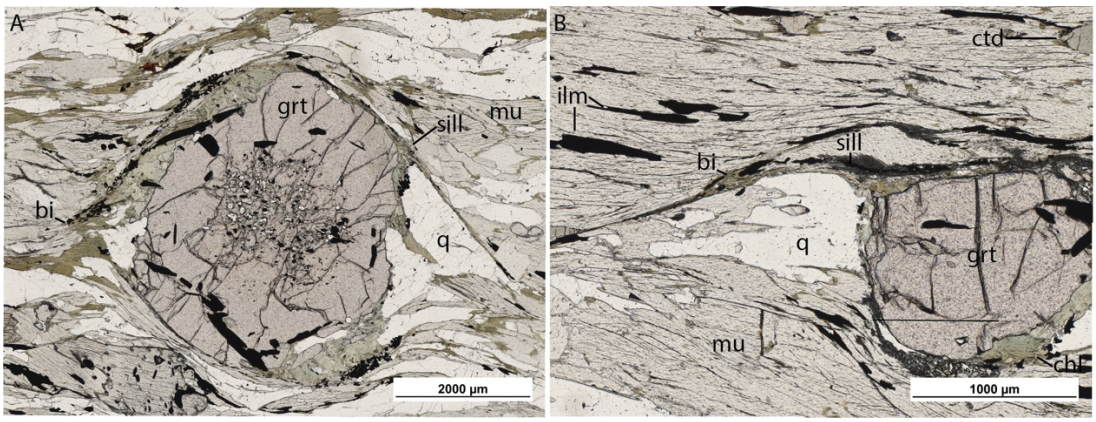

Figure 3.7: WGC18-007; A) Anastomosing rotational shear band surrounding garnet porphyroblast with quartz and chlorite infilling strain shadows, very fine sillimanite and biotite aligned within shear bands; B) Fine biotite and sillimanite growing within shear bands, mica fish developed around shear bands.

5. | MINERAL GEOCHEMISTRY

Garnet endmember compositions from sample WGC18-001A range from $grs_{0.35}$ (grs_x=Ca/Fe+Ca+Mg+Mn) $alm_{80.1}$ (alm_x=Fe/Fe+Ca+Mg+Mn) $prp_{16.3}$ (prp_x=Mg/Fe+Ca+Mg+Mn) $spss_{0.1}$ ($spss_x$=Mn/Fe+Ca+Mg+Mn) at the rim to $grs_{51.0}$ $alm_{82.8}$ $prp_{11.4}$ $spss_{0.9}$ at the core. Endmember compositions from sample WGC18-002 range from $grs_{0.35}$ $alm_{79.4}$ $prp_{16.5}$ $spss_{0.5}$ at the rim to $grs_{4.9}$ $alm_{71.1}$ $prp_{8.0}$ $spss_{15.9}$ at the core. Endmember compositions from sample WGC18-003 range from $grs_{5.1}$ $alm_{68.5}$ $prp_{26.1}$ $spss_{0.3}$ at the rim to $grs_{13.7}$ $alm_{70.4}$ $prp_{16.6}$ $spss_{4.4}$ at the core.

Garnet rim endmember compositions between all samples are similar, especially grossular, pyrope and spessartine, while almandine shows slightly more variance. Changes in endmember compositions WGC18-001A are more gradual and sloping, whereas WGC18-002 and WGC18-003 display more dramatic increases in endmembers transitioning from core to rim. Samples WGC18-002 and WGC18-003 display humps in their almandine content proximal to the porphyroblasts rim, core almandine compositions within the same samples are similar to their rim-edge composition. WGC18-002 contains highest spessartine core enrichment, 3–4 times greater than that of the other two samples. Subtle oscitations in grossular content within in WGC18-003 rims, with highest overall core composition.

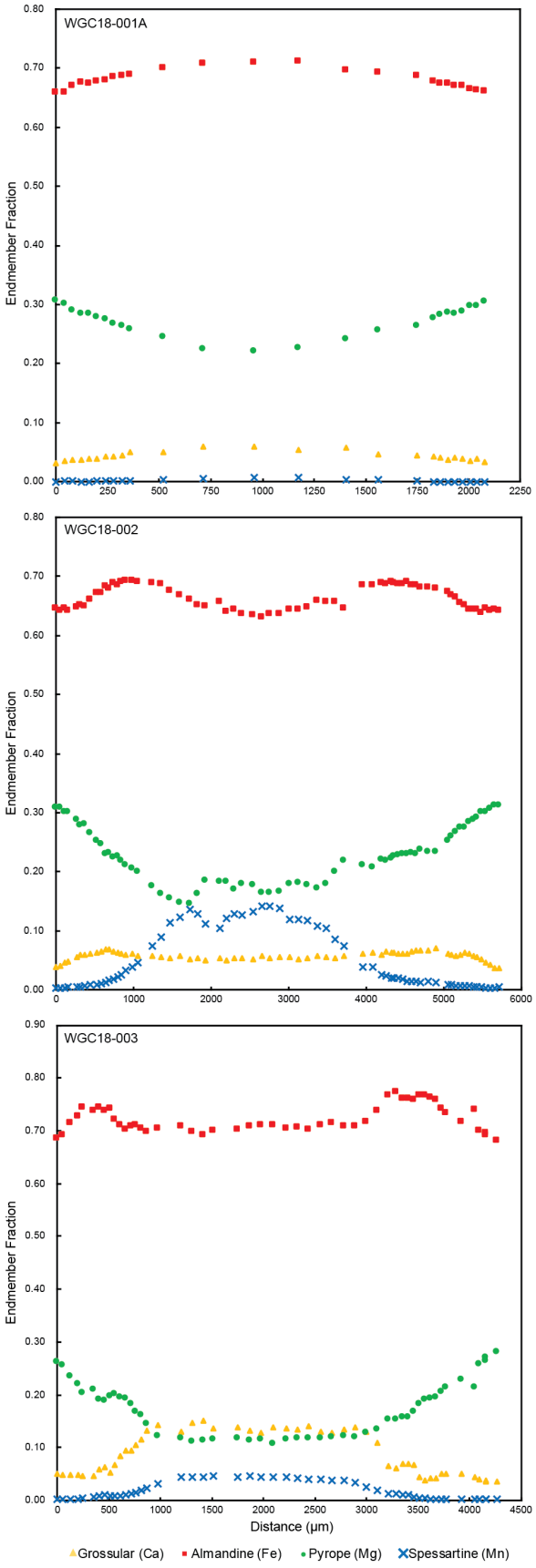

Figure 3.8: EMPA spot traverses of garnet porphyroblasts from samples WGC18-001A, WGC18-002 and WGC18-003. Porphyroblasts traversed the same as Figure 3.9 with location of traverses illustrated.

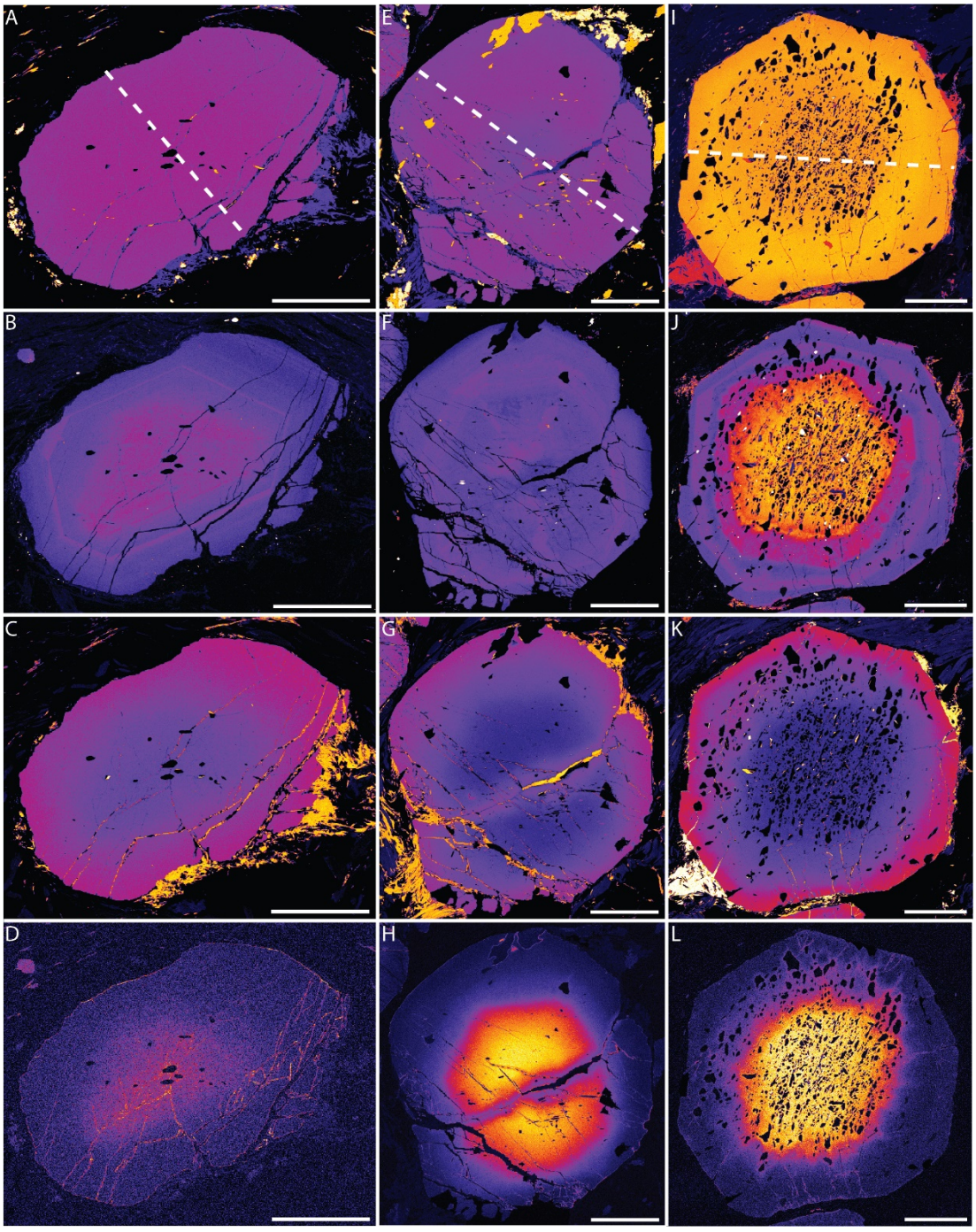

Figure 3.9: EMPA mapping of garnet, maps are non-quantitative, hot colours represent high concentration while cool colours represent low concentrations. A–D) Map of Fe, Ca, Mg & Mn respectively for garnet from sample WGC18-001A; E–H) Map of Fe, Ca, Mg & Mn respectively for garnet from sample WGC-002; I–L) Map of Fe, Ca, Mg & Mn respectively for garnet from sample WGC18-003. Scale bar represents 1000 μm in all images, dashed white line represents direction of EMPA traverse.

The core regions of multiple porphyroblasts display enriched Ca (Figure 3.9B; F; J) with characteristic prograde zoning of enriched depleted Mg (Figure 3.9C; G; K) and enriched Mn (Figure 3.9D; H; L). The boundary of the Ca and Mn enriched core areas correspond to the margin of the aligned inclusion rich core of the porphyroblasts (Figure 3.9J; L). Oscillatory

Ca zonation (Figure 3.9B; F; J) is present in several garnet porphyroblasts, varying from 50–800 µm in thickness.

Si-in-phengite ranges from 3.070 to 3.176 atoms-per-formula-unit (apfu) in sample WGC18-002, with a mean of 3.111 apfu. to 3.064 to 3.153 apfu. and mean of 3.108 apfu. in sample WGC18-003. Elemental mapping via EMPA shows the intergrowth of sodic paragonite within potassic muscovite. With paragonite represented by cool colours on a K map (Figure 3.10A) and represented by hot colours on a Na map (Figure 3.10B) taken of sample WGC18-003.

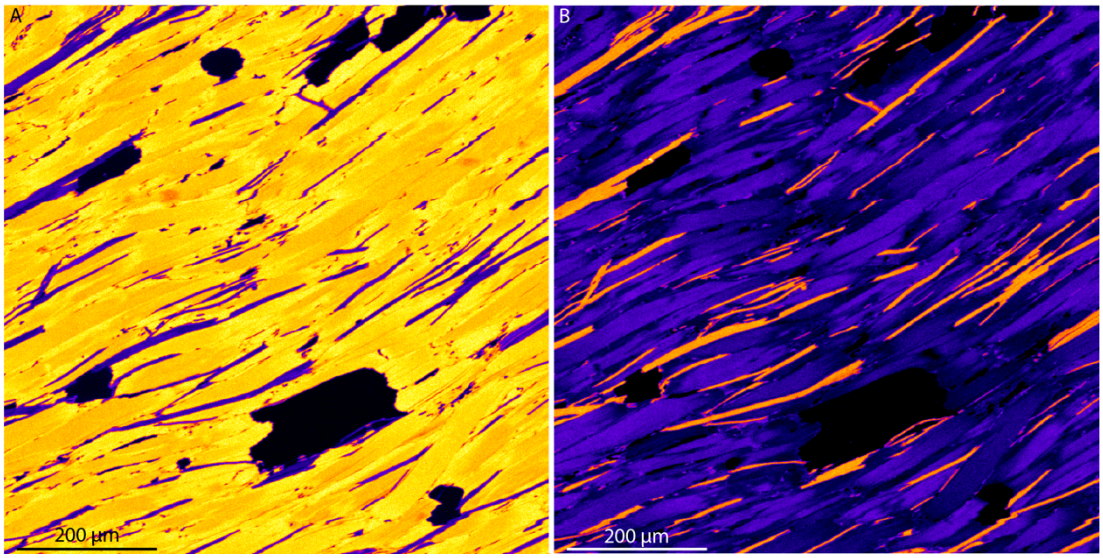

Figure 3.10: EMPA mapping of white mica for A) K and B) Na within sample WGC18-003, hot colours represent high concentration while cool colours represent low concentration. Paragonite represented by cool colours on K map and represented by hot colours on Na map.

Compositions of these micas range from 1.32–2.42 wt% Na_2O, with 7.32–8.76 wt% K_2O from sample WGC18-001A; 1.08–2.24 wt% Na_2O, 7.55–8.73 wt% K_2O from sample WGC18-002 and 1.42– 2.16 wt% Na_2O, with 7.34–8.68 wt% K_2O for sample WGC18-003.

Chloritoid within sample WGC18-002 contains (mean), 17.1 Mol% Fe, 7.92 Mol% Mg and 0.32 Mol% Mn. Staurolite within sample WGC19-002 contains (mean) 9.09 Mol% Fe of and of 1.34 Mol % Zn while staurolite within sample WGC19-003 contains (mean) 9.20 Mol% Fe and 1.78 Mol % Zn.

6. | PRESSURE–TEMPERATURE CONSTRAINTS

6.1 | Prograde

Modelled compositions of three samples are presented in Table 2. The prograde path of samples WGC18-002 and WGC18-003 starts with the chloritoid–rutile–ilmenite–muscovite–paragonite–quartz assemblage. Garnet growth subsequently occurs, likely with inclusion rich cores of rutile–ilmenite–muscovite–paragonite–quartz as well as sporadic small chloritoid inclusions. Staurolite growth begins as chloritoid de-stabilises, with large chloritoid porphyroblast exhibiting corroded boundary textures as a relic of this incomplete reaction. Further garnet growth also occurs, with small staurolite inclusions within rims. Further consumption of chloritoid may lead to kyanite growth.

Sample ID	**WGC18-002**	**WGC18-003**	**WGC18-004**
TiO_2	0.91	0.74	1.83
Cr_2O_3	0.02	0.01	0.01
SiO_2	55.56	60.41	44.52
Al_2O_3	21.51	17.13	15.21
CaO	0.43	0.85	5.64
MgO	2.70	3.33	10.53
FeO	8.90	8.07	9.76
MnO	0.19	0.16	0.13
O	0.44	0.40	0.48
K_2O	2.02	1.84	1.07
Na_2O	0.67	0.87	1.51

Table 3.1: Bulk rock compositions used for phase equilibria modelling in the MnNCKFMASHTO system

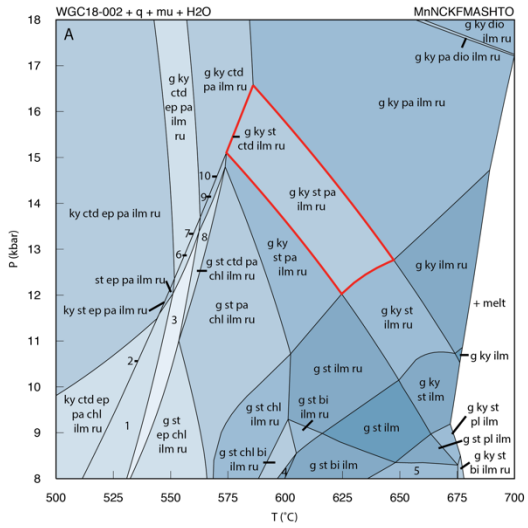

1 – st ctd ep pa chl ilm ru
2 – ky st ctd ep pa chl ilm ru
3 – g st ctd ep pa chl ilm ru
4 – g st chl bi ilm
5 – g st bi pl ilm
6 – g st ctd ep pa ilm ru
7 – g ky st ctd ep pa ilm ru
8 – g st ctd pa chl ilm ru
9 – g st pa chl ilm ru
10 – g ky st pa chl ilm ru

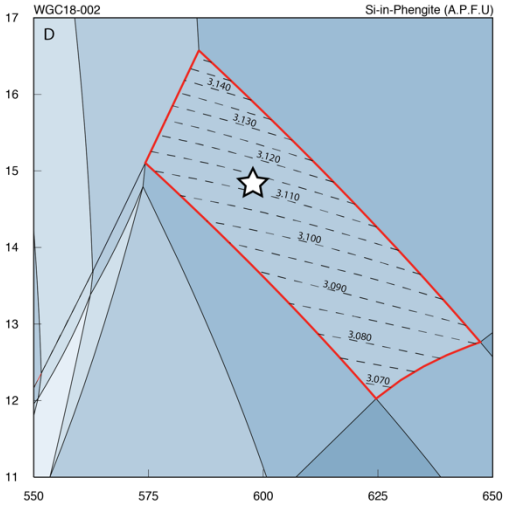

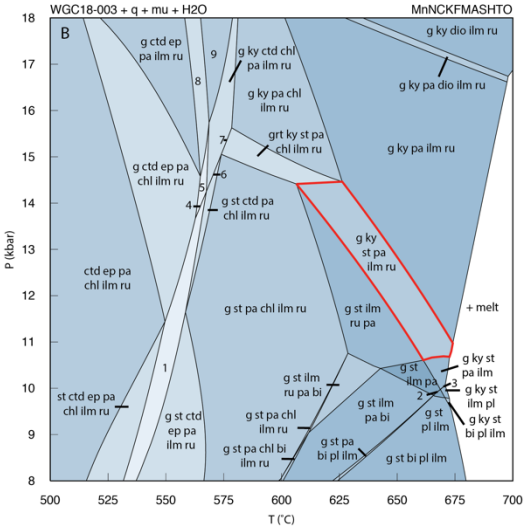

1 – g st ctd ep pa chl ilm ru
2 – g st pa pl ilm
3 – g ky st pa pl ilm
4 – g ky st ctd ep pa chl ilm ru
5 – g ky ctd ep pa chl ilm ru
6 – g ky st ep pa chl ilm ru
7 – g ky st ctd pa chl ilm ru
8 – g ky ctd ep pa ilm ru
9 – g ky ctd pa ilm ru

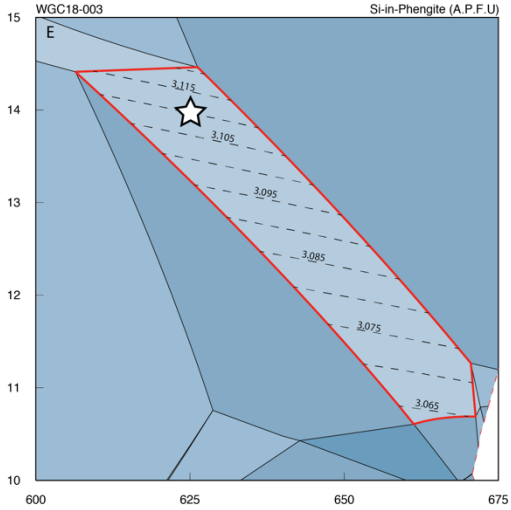

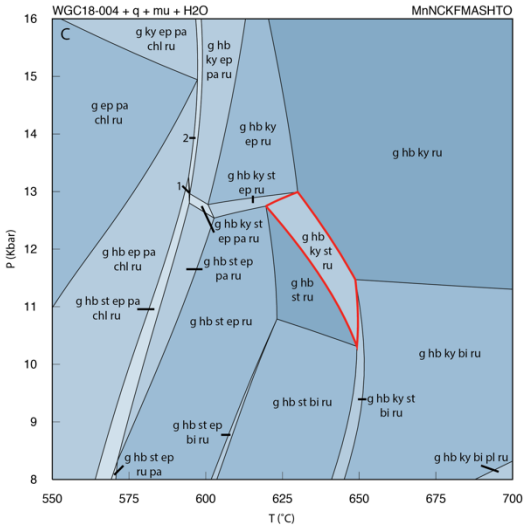

1 – g hb ky st ep pa chl ru
2 – g hb ky ep pa chl ru

Figure 3.11: Psuedosection of samples A) WGC18-002; B) WGC18-003 & C) WGC18-004 using the system MnNCKFMASHTO. g–garnet, ky–kyanite, st–staurolite, mu–muscovite, pa–paragonite, ep–epidote, bi–biotite, ctd–chloritoid, chl–chlorite, hb–hornblende ru–rutile, ilm–ilmenite, pl–plagioclase & dio–diopside. Peak assemblages outlined in red. D) & E); Contoured peak fields for Si-in-phengite (atoms-per-formula-unit) for sample WCG18-002 and WGC18-003 respectively, star represents mean Si-in-phengite a.p.f.u for each sample. See Table 3.1 for geochemical compositions modelled and Supplementary Data 1 for Si-in-phengite data

Sample WGC18-002 was found to have reached peak *P–T* conditions as defined by the garnet–kyanite–staurolite–muscovite–paragonite–rutile–ilmenite–quartz assemblage at pressures of 12–16 kbar and 575–650˚C (Figure 3.11A). Sample WGC18-003 was found to have reached peak *P–T* conditions as defined by the garnet–kyanite–staurolite–muscovite–paragonite–rutile–ilmenite–quartz assemblage at pressures of 11–16 kbar and 600–675˚C (Figure 3.11B). Sample WGC18-004 was found to have reached peak *P–T* conditions as defined by the garnet–kyanite–staurolite–hornblende–muscovite–rutile–quartz assemblage at pressures of 10–13 kbar and 625–650˚C (Figure 3.11C). Contouring of samples WGC18-002 and WGC18-003 within the peak fields for Si-in-phengite a.p.f.u. (see 3.11) places the mean Si-in-phengite composition of WGC18-002 equivalent to ~15 kbar (Figure 3.11D) and the composition of WGC18-003 equivalent to ~14 kbar (Figure 3.11E). Some analysis record lower values equating to pressures in the range of 11–12 kbar and subsequently up temperature to 600–675˚C.

6.2 | Retrograde

The retrograde path for samples WGC18-002 and WGC18-003 trace (near)isothermally through 10 kbar, producing biotite growth, aligned within microshear bands, subsequently moving through 6 kbar, causing sillimanite pseudomorphing of kyanite margins along with sillimanite growth, aligned within microshear bands in conjunction with biotite. The samples subsequently cooled though 575˚C at pressures less than 6 kbar, post onset of sillimanite growth and kyanite pseudomorphing to account for chlorite growth around garnet porphyroblast.

7. | ACCESSORY MINERAL GEOCHRONOLOGY AND GEOCHEMISTRY

7.1 | Monazite

Monazite grains found several different textural positions; garnet core; garnet rim; alignment with the foliated quartz-muscovite fabric from samples WGC18-001A, WGC18-002 and WGC18-003. Monazite within sample WGC18-001A yielded a weighted average age of 428.9 ± 1.6 Ma (2σ, MSWD = 1.0) with n = 71 spots analysed (Figure 3.12). Monazite within sample WGC18-002 yielded a weighted average age of 425.8 ± 3.1 Ma (2σ, MSWD = 1.1) with n = 57 spots analysed (Figure 3.12). Monazite within sample WGC18-003 yielded a weighted average age of 429.7 ± 2.5 Ma (2σ, MSWD = 1.9) with n = 45 spots analysed (Figure 3.12).

No obvious trends based on grain location within various textures were observed. See supplementary data table 3 for further data.

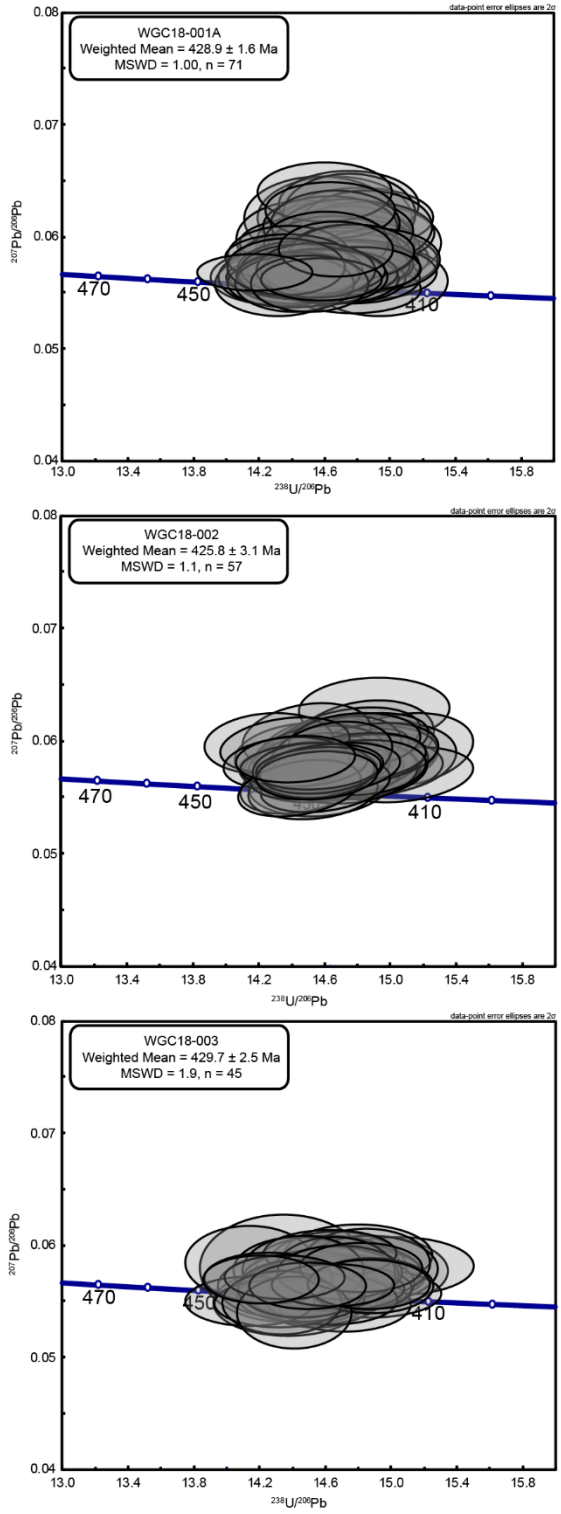

Figure 3.12: U–Pb geochronology of monazite by LA-ICP-MS for samples WGC18-001A, WGC18-002 and WGC18-003. All errors reported as 2SE.

7.2 | Rutile

7.2.1 | U–Pb geochronology

Rutile grains within samples WGC18-001A, WGC18-003, WGC18-008 and WGC18-011 were analysed, sample WGC18-002 was excluded from analysis due to rutile being smaller than the required laser spot size. Rutile within sample WGC18-001A yielded a lower intercept age of 378.6 ± 3.3 Ma (2σ, MSWD = 2.0) from n = 84 spots, while rutile within sample WGC18-003 yielded a lower intercept age of 379.3 ± 5.1 Ma (2σ, MSWD = 2.3) from n = 69 spots (Figure 3.13).

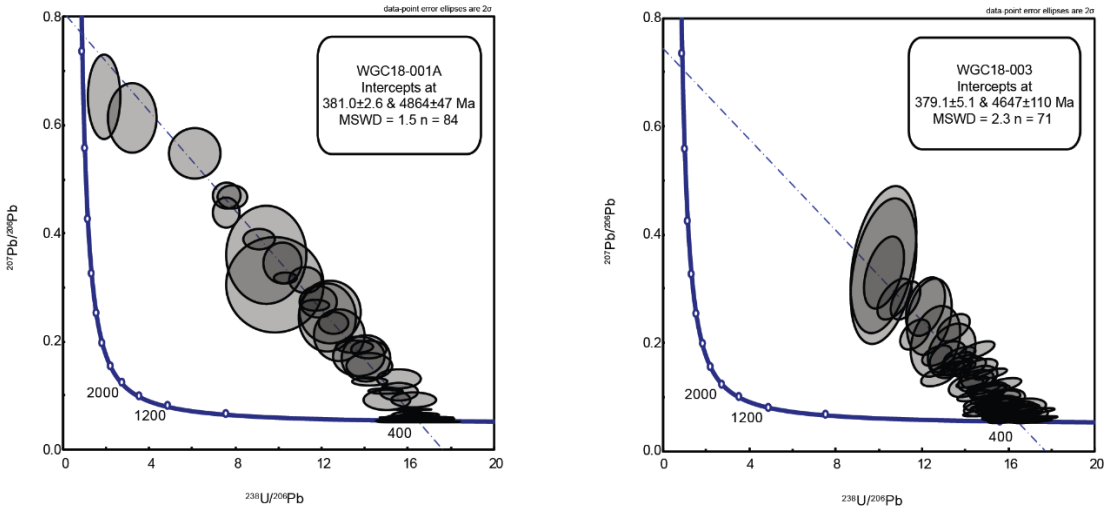

Figure 3.13: U–Pb geochronology of rutile by LA-ICP-MS for samples WGC18-001A and WGC18-003. All errors reported as 2SE.

The (relatively) high MSWD can be explained through a large size variation in rutile grains analysed, differing sized grains, along with differing areas undergoing closure at varying times. Larger grains (>200 µm) are known to close at higher temperatures, ~610˚C; compared to smaller grains (<70 µm), ~570˚C (Cherniak, 2000; Zack & Kooijman, 2017; Zack et al., 2011), hence rims and finer grains recording a younger age than core areas with a diffusion gradient across the grain. This results in a non-singular lower intercept of the Concordia plot, accounting for the larger MSWD. See Supplementary Data Table 4 for further data.

7.2.2 | Zr-in-rutile thermometry

The Zr-in rutile thermometer has been demonstrated to be roust in high grade conditions (Kooijman, Smit, Mezger, & Berndt, 2012); as such it is appropriate to be used in high grade rocks as those presented in this study. Zr concentration from n=156 rutile analyses within two samples (WGC18-001A and WGC18-003) obtained by LASS was used to calculate temperature ranges at 14 kbar, based on the calibration of (Tomkins et al., 2007), using the upper end of the interquartile range for each sample and error of ±25˚C. 14 kbar was chosen for the calculation based on overlapping peak fields for three samples obtained via phase

equilibria modelling. Zr concentration within sample WGC18-001A range from 86 to 376 ppm, recording a temperature of 645 ± 25˚C (Figure 3.14). Zr concentration within sample WGC18-003 range from 112 to 224 ppm, recording a temperature of 616 ± 25˚C at 14 kbar (Figure 3.8). See supplementary data table 2.

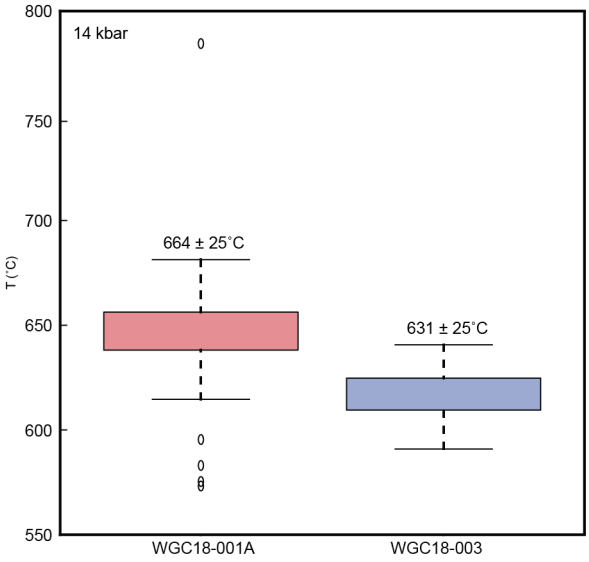

Figure 3.14: Zr-in-rutile thermometry for samples WGC18-001A and WGC18-003, calibration based on Tomkins et al. (2007) at 14 kbar.

8. | DISCUSSION

8.1 | *P–T* evolution

Overlapping peak fields constrained by phase equilibria modelling (samples WGC18-002, WGC18-003 & WGC18-004) along with the application of Si-in-phengite contouring of peak fields gives pressure estimates in the range of 14–15 kbar. These pressures equate to the Hyllestad Complex being subducted to depths in the range of 50–55 km (Figure 3.15). Though outlier lower Si-in-phengite values compared to the mean values for peak P suggest that phengite growth continued to occur down pressure (12–14 kbar) towards peak T of 625–650˚C (Figure 3.15), constrained by Zirconium-in-rutile thermometry. From this it is likely that the rocks of the Hyllestad Complex close to the NSDZ reached peak *P* before reaching peak *T* during exhumation.

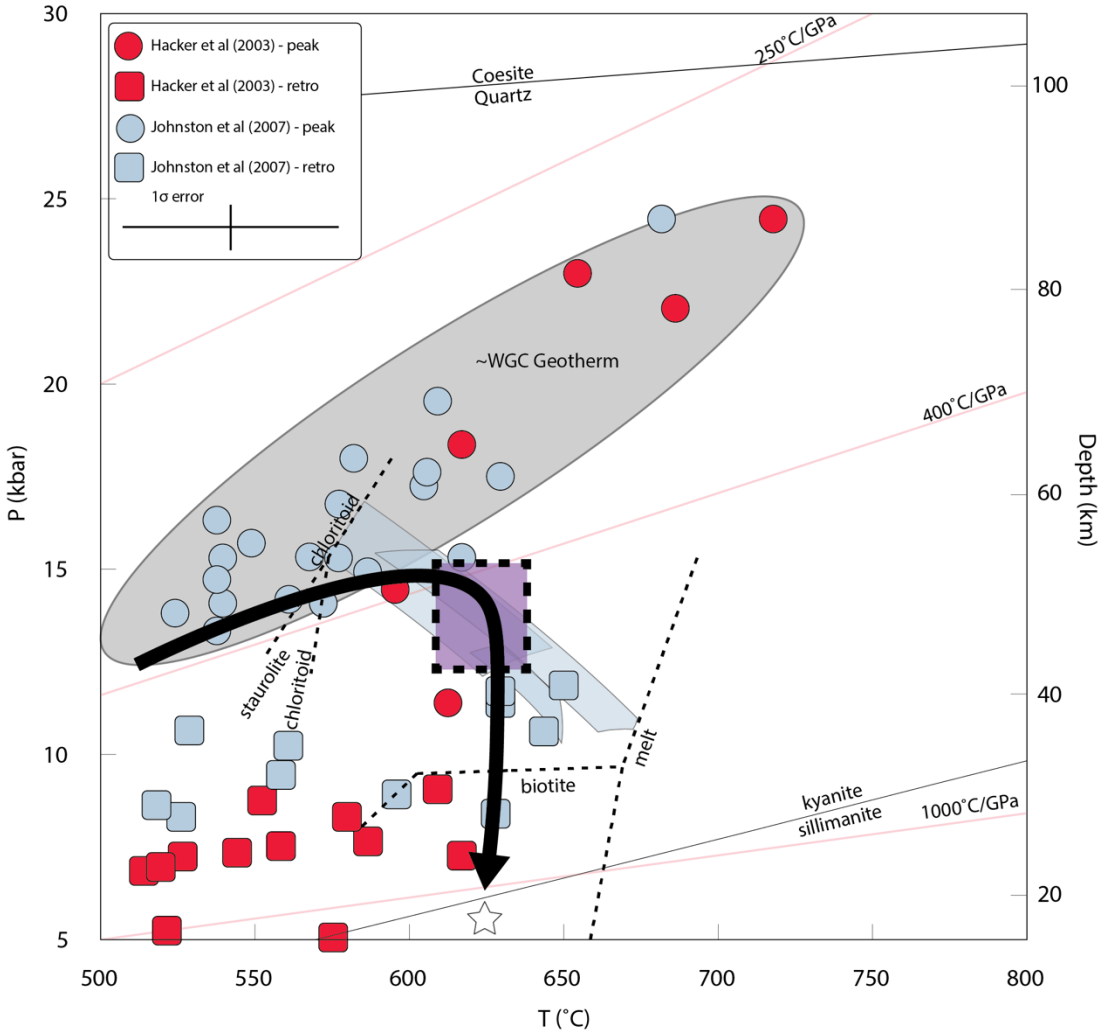

Figure 3.15: P–T path diagram, peak fields for samples WGC18-002, WCG18-003 & WCG18-004 along with chloritoid, staurolite, biotite & melt reactions calculated within THERMOCALC. Overlapping fields of samples WGC18-002, WGC18-003 and WGC18-004 represent peak P–T within the Hyllestad Complex. Peak T constraint calculated by Zr content within rutile at 14 kbar (sample WGC18-001A & WGC18-003), representing peak T reached during shear heating. Purple box represents peak P–T conditions within the Hyllestad Complex from overlapping peak fields and Si-in-phengite barometry. Peak and retrograde assemblages taken from Hacker et al. (2003) & Johnston et al. (2007), Western Gneiss Complex geotherm approximated from this. Prograde path accounts for diminishing chloritoid and increasing staurolite along WGC geotherm. Hollow star represents minimum pressure for samples WGC18-002 & WCG18-003 to account for sillimanite growth, exhumation path of isothermal decompression that occurred post peak.

The timing of the onset of crustal loading can be resolved from monazite in a variety of textural positions within the three samples (428.9 ± 1.6, 425.8 ± 3.1 and 429.7 ± 2.5 Ma). Monazite ages of this study are near identical to the younger age population (c. 430 Ma) of two within the Hyllestad area of Hacker et al. (2015), though we do not find resolve the c. 450 Ma population. The younger population of Hacker et al. (2015), along with the ages obtained by this study likely represents the early onset of Baltic-Laurentian continental collision with the

thrusting of the Allochthons on top of the Precambrian proto-Western Gneiss Complex basement, see Roberts (2003). The older population c. 450 Ma likely represents one of the older pre-Scandian tectonic events that occurred on the Baltic margin, see Roberts (2003).

Kyanite porphyroblast rims exhibit fine sillimanite polymorphs, with this reaction occurring at far lower pressures than the original kyanite porphyroblast growth. The transition from peak *P–T* conditions (14–15 kbar) where kyanite is stable, to those in which sillimanite becomes stable (<6 kbar) occurs along a path of (near)isothermal decompression, with this reaction calculated to occur at temperatures greater than 600˚C. This equates to rapid exhumation to a depth of ~20 km occurs due to the fine-grained nature of the sillimanite as well as the incomplete polymorphic reaction. Fine grained sillimanite and biotite aligned within shear bands imply syn-kinematic growth of these minerals within the bands. Chlorite and biotite growth along the retrograde path at *P–T* conditions <575˚C and <5 kbar within the samples correlates to the late greenschist–amphibolite facies overprint surrounding the Nordfjord–Sogn detachment zone (Eide et al., 1997; Hacker et al., 2003a; Johnston et al., 2007a; Labrousse et al., 2004; Norton, 1987).

This (near)isothermal exhumation and sillimanite polymorphing/growth has been previously recognised in the area by Chauvet et al. (1992) and Hacker et al. (2003a), but neither study provides an explanation for this occurrence. Other studies including Hacker (2007); Kylander-Clark et al. (2009); Root et al. (2005); Terry et al. (2000) Labrousse et al. (2004) and others have all recognised the rapid, (near)isothermal ascent of the Western Gneiss Region and overlying Allochthons as a whole.

8.2 | Nordfjord–Sogn detachment zone movement and timing

Very fine-grained sillimanite and biotite occur within shear fabrics, oriented in the direction of these small-scale (<50 μm wide) anastomosing shear bands. The growth of these minerals confines the *P–T* conditions during their formation to <6 kbar for sillimanite and biotite growth, implying the formation of these shear structures under similar conditions. Such minerals growing within a shear structure points to their growth during the extensional activation of the Nordfjord–Sogn detachment zone, generating this shear structures along with the rapid exhumation of these rocks to pressures less than 6 kbar (20 km depth; Figure 10). The marginal replacement of kyanite porphyroblasts with fine sillimanite as a result of near isothermal exhumation *P–T* path is also likely to be a result of rapid movement and exhumation along the Nordfjord–Sogn detachment zone towards <20 km of depth.

Rutile ages from samples WGC18-001A and WGC18-003 represent cooling ages, with the drop below closure temperatures occurring as the samples were exhumed approximately through 550–600˚C (Cherniak, 2000), preserving lower intercepts of 378.6 ± 3.3 Ma and 379.3

± 5.1 Ma respectively. Discrepancies in the lower closure temperature (but older) $^{40}Ar/^{39}Ar$ muscovite ages of the Hyllestad area (403.3±0.7 Ma, 399.1±0.8 Ma 403.1±1.1 Ma 395.2±1.3 Ma) (Chauvet & Dallmeyer, 1992) and the higher closure temperature (but younger) U–Pb rutile age of this study can be explained threefold. (1) results of the Chauvet and Dallmeyer (1992) study involved the use of the *MMhb-1 hornblende* standard (Samson & Alexander, 1987) which displays extreme age-heterogeneity Renne et al. (1998); Spell and McDougall (2003), as such is not appropriate as an $^{40}Ar/^{39}Ar$ fluence monitor (Jourdan & Renne, 2007). (2) Some degree of radiogenic argon may be retained within analysed grains thus failing to represent an open system, instead recording to some degree in (U)HP rocks the crystallisation (or peak metamorphic) age rather than cooling/decompression (McDonald, Regis, Warren, Kelley, & Sherlock, 2018; Smye, Warren, & Bickle, 2013; Warren, Hanke, & Kelley, 2012). (3) radiogenic argon released from local matrix phases incorporated as in-situ derived excess-Ar (Ar_e), leading to ages between equilibration at (U)HP conditions and cooling through closure temperature (McDonald et al., 2018; Smye et al., 2013).

P–T conditions for this lower intercept can be constrained in that tracing a (near)isothermal exhumation path from peak conditions towards the surface the Hyllestad Complex does not cool though 575–600˚C until being exhumed through at least 6 kbar. This places the Hyllestad Complex at less than 20 km at this time. This implies cooling through this temperature would have occurred at upper structural levels to account for this substantially shallower crustal position than that of the peak conditions.

Obtaining a precise cooling rate from the metamorphic peak of the Hyllestad Complex from current data is difficult though a number assumptions can be made. The nature of cooling of the Hyllestad Complex may be more complex than a simple linear rate may suggest due to its proximity to the large, heat generating NSDZ. Shear heating likely would have assisted in maintaining near peak temperatures for longer periods of time even while exhumation is occurring, with faster cooling rates occurring at a time after the cessation of movement in the detachment. A relatively uniform population of rutile despite a range of core and rim spot locations is present across two samples, thus due to the highly variable closure temperature of rutile when subjected to slow cooling (Kooijman, Smit, Mezger, & Berndt, 2012) the Hyllestad Complex was likely subjected to rapid cooling with the grains closing relatively early in the exhumation cycle.

The degree of movement along the detachment can be determined by the exhumation of the Hyllestad Complex, from a depth 50km (15 kbar) to at least 20km (<6 kbar), equating to 30 km of vertical displacement (Figure 10). Movement along the detachment surface itself can be calculated using the plunge range (20–40˚) of the west dipping extensional lineations present

in the Hyllestad Complex (Hacker et al., 2003a). This equates to ~50–80 km of movement along the detachment surface, though this calculation may overstate movement due to the likelihood of the detachment initially occurring steeper at depth and shallowing to the surface.

Rutile ages of this study (c. 378–379 Ma) are similar to those of Cutts et al. (2019a) 375–380 Ma from further north in the WGC. The similarities in these ages, despite the sample localities of the Hyllestad Complex being some 200 km SW of Nordøyane (c. 375 Ma) suggests synchronous cooling through ~550–600˚C across a large swathe of the WGC and some overlying allochthons (Hyllestad Complex). This homogenous cooling requires the WGC and allochthons to exhumed to relatively flat slab conditions, with homogenous mass removal of material across this wide area driving the cooling, similar to that of erosion on a orogenic plateau (Cutts et al., 2019a).

8.3 | Peak T differences

The peak and retrograde temperatures calculated for the Hyllestad Complex are some 50–100˚C hotter than previous estimates using conventional thermobarometry by studies of Chauvet et al. (1992), Hacker et al. (2003a) and Johnston et al. (2007b), with the authors estimating peak temperatures of 500–600˚C (Figure 3.15). Comparatively peak pressure calculations from this study are in similar ranges to the aforementioned studies of 12–15 kbar.

Shear zone modelling conducted by Souche et al. (2013), on segments of the Nordfjord–Sogn detachment zone along with other studies (Brun & Cobbold, 1980; Campani et al., 2010; Hartz & Podladchikov, 2008) suggest that shear heating may be able to provide increased heat flow, altering the heat budget of the area surrounding the detachment. Modelling suggests that temperatures may be elevated by up to 100˚C within 5 km from the detachment (Duprat-Oualid & Yamato, 2017; Mako & Caddick, 2018; Platt, 2015; Schmalholz & Duretz, 2015; Souche et al., 2013), with the Hyllestad Complex samples of this study falling within this zone. Thus, shear heating may provide extra heat that places peak metamorphic conditions of samples of this study outside of the geothermal gradient, recorded by the bulk of analysed samples from the Western Gneiss Complex (Figure 3.15).

MATLAB code (Clark et al., 2011; Clark et al., 2015) was used to calculate geothermal gradients over time solved by finite difference method (Crank-Nicolson) after England and Thompson (1984). A conservative value of shear stress (τ) of 45 MPa was used based on previous work of (Johnston et al., 2007b; Souche et al., 2013) for the example including shearing, while shear stress (τ) was set to 1 MPa for the pure crustal stacking model. Shear zone width was set as 4 km using the 3–5 km thickness of the brittle-ductile mylonitic layer in the Solund-Sunnfjord area as a proxy for thickness (Andersen & Andresen, 1994; Andersen & Jamtveit, 1990; Hacker et al., 2003a). Shear zone was initiated at 58 km of depth, as if

occurring at the base of the Hyllestad Complex, with a shear zone duration of 1 Ma and velocity of 3 cm/yr, representing the 30 km of crustal section missing to the Western Gneiss Complex in the footwall. Two particles were tracked, initially positioned at 50 (13.2 Kbar) and 55 km (14.6 kbar) of depth, 8 and 3 km above the shear zone respectively.

When τ=1 (i.e. near zero shear stress) this model setup produces peak temperatures for the 55km and 50 km deep particle of 548˚C & 512˚C respectively (Figure 3.16). When τ=45 (i.e. with shear stress,) this model setup produces peak temperatures for the 55km and 50 km deep particle 648˚C & 618˚C respectively (Figure 3.16). This difference equates to ~100˚C of temperature increase with the presence of shear heating, compared to peak temperatures produced purely through crustal stacking. Differences in shear zone duration and velocity may be varied to produce near identical results to the v= 3 cm/yr and duration= 1 ma setup, as long as total vertical displacement is equal to 30 km, equivalent to the missing crust between the Hyllestad Complex and the WGC.

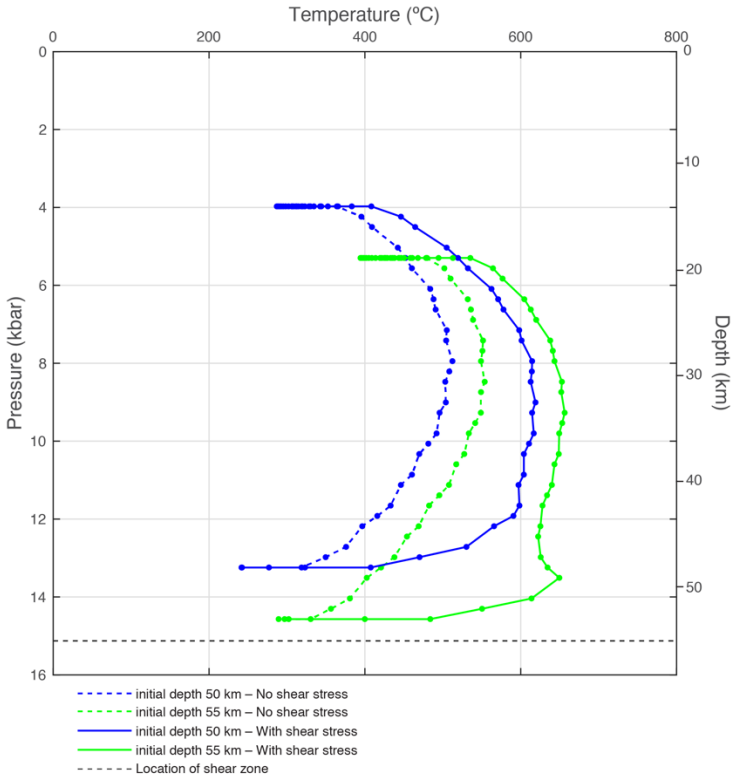

Figure 3.16: Modelled particle paths, green initially at 55 km, blue initially at 50km. Dashed represent nil shear stress (1 MPa), solid with shear stress (45 MPa). Grey dashed represents shear zone initiated at 58 km. See Appendix A for modelled conditions.

The above model demonstrates that without shear heating sufficient heat is not produced required to explain the peak temperatures observed by this study, nor does it produce sufficient heat to explain the (near)isothermal exhumation observed. Recent work (Kiss, Podladchikov, Duretz, & Schmalholz, 2019) suggests that if relative *T* increase within the shear zone is

greater than 50˚C, shear heating is able to overpower convective cooling and that increase in *T* extends far beyond the boundary between the highly strained shear zone and the low-strained wall rock, consistent with the findings of this study.

Shear heating thus is a possible mechanism to explain the discrepancies in the peak T of this study compared to others (Chauvet et al., 1992; Hacker et al., 2003a; Johnston et al., 2007b). Results indicate that shear heating may also provide the extra heat required to maintain rapid (near)isothermal decompression during exhumation, proposed by this and other studies of allochthonous sediments exhumed along Caledonian detachments (Chauvet et al., 1992; Hacker et al., 2003a; Johnston et al., 2007b; Souche et al., 2013).

9. | CONCLUSION

The application of phase equilibria modelling in place of previous conventional thermobarometry coupled with *in-situ* petrochronology has allowed new *P–T–t* constraints to be placed on the allochthonous Hyllestad Complex in the Sognefjorden area. Peak *P–T* conditions in the Hyllestad Complex were calculated by this study to be 12–15 kbar at temperatures of 600–650˚C, equating to reaching 50 km of depth. Monazite geochronology likely records the onset of crustal loading to c. 429–425 Ma, significantly earlier than the peak of eclogite facies metamorphism in the southern Western Gneiss Complex in which it overlies.

Within the aluminous schists of the Hyllestad Complex peak temperatures along with retrograde temperatures as a result of (near)isothermal decompression calculated by this study were found to be 50–100˚C higher than previous applications of conventional thermobarometry (Chauvet et al., 1992; Hacker et al., 2003a; Johnston et al., 2007b). Hyllestad Complex samples of this study were also to have found to exist outside of the geothermal gradient of the south-western Scandinavian Caledonides, in which the majority of samples lie (Chauvet et al., 1992; Hacker et al., 2003a; Johnston et al., 2007b).

Movement along the Nordfjord–Sogn detachment zone is again shown to have played a key part in exhumation post the Scandian Orogeny, with overprinting ductile structures and higher temperature mineral assemblages present throughout the Hyllestad Complex. After the advent of extension leading to exhumation at c. 379 Ma the Hyllestad Complex would have been exhumed to at least 20 km of depth cooling through 575–600˚C. This structure has allowed for rapid exhumation through a very large (30 km) section of crust, allowing the preservation of high temperatures at shallow depths.

Shear heating caused by mechanical work during exhumation of the Hyllestad Complex along the Nordfjord–Sogn detachment zone is proposed to; account for the perturbation from the geothermal gradient of the south-western Scandinavian Caledonides; account for the

differences in peak T estimates of previous workers, working distal to the Nordfjord–Sogn detachment zone; and supply sufficient heat to maintain (near)isothermal conditions during exhumation as recognised by this and other studies (Chauvet et al., 1992; Souche et al., 2013).

4. THESIS CONCLUSIONS

The Western Gneiss Complex (WGC) is a classic area to study deep subduction and return of continental crust. However, the southern segment of the WGC is relatively poorly studied and understood. This thesis investigates the *P–T–t* record of eclogite bodies that occur in the southern portion of the WGC and of allochthonous aluminous schists that crop out within the hanging wall of the Nordfjord–Sogn detachment zone, a large-scale structure that played a major role in the exhumation and juxtaposition of these rocks.

5.1 | Application of phase equilibria modelling to Southern Western Gneiss Complex

This thesis represents some of the first phase equilibrium modelling conducted within the Scandinavian Caledonides for the purpose of ascertaining peak *P–T* conditions. The modelling indicates that aluminous schists of the Hyllestad Complex reached peak conditions of 12–15 kbar (40–50 km) at temperatures of 600–650˚C. Eclogite bodies within the Western Gneiss Complex in the footwall of the Nordfjord–Sogn detachment reached peak conditions of 24–28 kbar and 670–780˚C (85–100 km). Within the Hyllestad Complex, modelling constraints of the aluminous schists show that these rocks record (near)isothermal exhumation to <6 kbar. However, the eclogitic samples are more difficult to model due to high-variance assemblages and a lack of predicted changes in mineral chemistry during exhumation.

5.3 | Lu–Hf geochronology

This work highlights the difficulties of applying the Lu–Hf geochronometer to samples containing low (<5ppm on average) MREE and HREE concentrations. A set of simple calculations and a discussion has been presented around the common accessory phases that may wreak the most havoc if “accidentally” dissolved during this methodology. Many of these effects are not easily quantifiable with the current knowledge base thus further work to understand the micro–nanoscale distribution of REE elements within minerals subjected to selective leaching and dissolution during this analytical process would be pertinent.

5.4 | Shear heating

Samples from within the Hyllestad complex record *P–T* conditions suggesting a deviation from the regional stable geotherm as recorded by a large number of conventional barometers and thermometers. The fidelity of multiple-sample phase equilibria modelling coupled with contouring of peak fields and Zr-in-rutile thermometry give estimates that are more precise than those derived using conventional thermometers. This observation that thermal perturbations due to mechanical work done within the shear zone based on natural samples (as opposed to those modelled by a multitude of 2D and 3D thermomechanical models) can extend outside of the mylonitic zone. This addition of frictional heat maintained a (near)isothermal

exhumation path for the Hyllestad Complex, with potential implications large-scale crustal structures elsewhere.

5.5 | Constraints on the exhumation rate

Some relative constraints can be placed on the timing and rate of exhumation for rocks within the hanging wall (Hyllestad Complex) and footwall (Western Gneiss Complex) of the Nordfjord–Sogn detachment. Exhumation is likely to have been rapid based on a lack of equilibration implied by the Zr-in-rutile thermometry, remaining consistent with peak *T* conditions calculated by phase equilibria modelling. Finer grained low(er) pressure minerals grow within shear bands, pointing to the activation of the Nordfjord–Sogn detachment occurring during this exhumation.

5.6 | Tectonic implications

This thesis confirms that the Nordfjord–Sogn detachment played a key role in evolving tectonostratigraphy of the Scandinavian Caledonides. Within the Hyllestad area, it juxtaposes two distinct lithologies with very different *P–T* histories, which were separated by up to 50 km during the peak of metamorphism, equating to a very large volume of missing rock. Rutile geochronology from rocks of the Hyllestad Complex return similar ages to those from deeply subducted rocks of the Western Gneiss Complex 100 km further to the north. This lends weight to the idea the Western Gneiss Complex and overlying allochthons were exhumed from deep within the subduction zone to (near)flat-slab conditions, with subsequent denudation accounting for their present-day positions.

5.7 | Further work

This thesis raises further questions that could be subjected to future work:

1. Wider-scale application of phase equilibrium modelling to other eclogites throughout the Western Gneiss Complex;
2. Dating the rocks using other geochronometers to ascertain the timing of peak *P–T* conditions and the duration and rates of cooling recorded by the various eclogite bodies within the Sognefjorden area;
3. Additional U–Pb rutile ages from the sampled eclogites to compare with rocks of the Hyllestad Complex as well as with data from rutile and other geochronometers with lower closure temperatures that exists further to the north surrounding the UHP domains. More data from the southern segment of the Western Gneiss Complex will permit a more detailed 4D picture of exhumation of the Western Gneiss Complex.

5. BIBLIOGRAPHY

Agard, P., Jolivet, L., & Goffe, B. (2001). Tectonometamorphic evolution of the Schistes Lustres Complex; implications for the exhumation of HP and UHP rocks in the Western Alps. *Bulletin de la Societe Geologique de France, 172*(5), 617-636.

Åhäll, K. I., & Gower, C. F. (1997). The Gothian and Labradorian orogens: Variations in accretionary tectonism along a late Paleoproterozoic Laurentia-Baltica margin. *Gff, 119*(2), 181-191.

Aleinikoff, J. N., Schenck, W. S., Plank, M. O., Srogi, L. A., Fanning, C. M., Kamo, S. L., & Bosbyshell, H. (2006). Deciphering igneous and metamorphic events in high-grade rocks of the Wilmington complex, Delaware: Morphology, cathodoluminescence and backscattered electron zoning, and SHRIMP U-Pb geochronology of zircon and monazite. *Geological Society of America Bulletin, 118*(1-2), 39-64.

Amato, J., Johnson, C., Baumgartner, L., & Beard, B. (1999). Sm-Nd geochronology indicates rapid exhumation of Alpine eclogites. *Earth Planet. Sci. Lett, 171*, 425-438.

Anczkiewicz, R., Chakraborty, S., Dasgupta, S., Mukhopadhyay, D., & Kołtonik, K. (2014). Timing, duration and inversion of prograde Barrovian metamorphism constrained by high resolution Lu–Hf garnet dating: A case study from the Sikkim Himalaya, NE India. *Earth and Planetary Science Letters, 407*, 70-81.

Anczkiewicz, R., Platt, J. P., Thirlwall, M. F., & Wakabayashi, J. (2004). Franciscan subduction off to a slow start: evidence from high-precision Lu–Hf garnet ages on high grade-blocks. *Earth and Planetary Science Letters, 225*(1-2), 147-161.

Anczkiewicz, R., Thirlwall, M., Vance, D., Mueller, W., & Villa, I. (2003). Geochronology: linking the isotopic record with petrology and textures. *J Geol Soc London Spec Publ, 220*, 83-91.

Andersen, T. B. (1998). Extensional tectonics in the Caledonides of southern Norway, an overview. *Tectonophysics, 285*, 333-351.

Andersen, T. B., & Andresen, A. (1994). Stratigraphy, tectonostratigraphy and the accretion of outboard terranes in the Caledonides of Sunnhordland, W. Norway. *Tectonophysics, 231*(1), 71-84.

Andersen, T. B., & Jamtveit, B. (1990). Uplift of deep crust during orogenic extensional collapse: A model based on field studies in the Sogn-Sunnfjord region of Western Norway. *Tectonics, 9*(5), 1097-1111.

Andersen, T. B., Jamtveit, B., Dewey, J. F., & Swensson, E. (1991). Subduction and eduction of continental crust: major mechanisms during continent-continent collision and orogenic extensional collapse, a model based on the south Norwegian Caledonides. *Terra Nova, 3*(3), 303-310.

Angel, R. J., Mazzucchelli, M. L., Alvaro, M., Nimis, P., & Nestola, F. (2014). Geobarometry from host-inclusion systems: the role of elastic relaxation. *American Mineralogist, 99*(10), 2146-2149.

Angel, R. J., Nimis, P., Mazzucchelli, M. L., Alvaro, M., & Nestola, F. (2015). How large are departures from lithostatic pressure? Constraints from host–inclusion elasticity. *Journal of Metamorphic Geology, 33*(8), 801-813.

Austrheim, H., Corfu, F., Bryhni, I., & Andersen, T. B. (2003). The Proterozoic Hustad igneous complex: a low strain enclave with a key to the history of the Western Gneiss Region of Norway. *Precambrian Research, 120*(1), 149-175.

Axler, J. A., & Ague, J. J. (2015). Exsolution of rutile or apatite precipitates surrounding ruptured inclusions in garnet from UHT and UHP rocks. *Journal of Metamorphic Geology, 33*(8), 829-848.

Baldwin, S. L., Webb, L. E., & Monteleone, B. D. (2008). Late Miocene coesite-eclogite exhumed in the Woodlark Rift. *Geology, 36*(9), 735-738.

Beaumont, C., Jamieson, R. A., Butler, J. P., & Warren, C. J. (2009). Crustal structure: A key constraint on the mechanism of ultra-high-pressure rock exhumation. *Earth and Planetary Science Letters, 287*(1-2), 116-129.

Bercovici, D., & Ricard, Y. (2012). Mechanisms for the generation of plate tectonics by two-phase grain-damage and pinning. *Physics of the Earth and Planetary Interiors, 202-203*, 27-55.

Bingen, B., Andersson, J., Soderlund, U., & Moller, C. (2008a). The Mesoproterozoic in the Nordic countries. *Episodes, 31*(1), 1-6.

Bingen, B., Nordgulen, Ø., & Viola, G. (2008b). A four-phase model for the Sveconorwegian orogeny, SW Scandinavia. *Norsk geologisk tidsskrift., 88*(1), 43.

Bockelie, J. F., & Nystuen, J. P. (1985). The southeastern part of the Scandinavian Caledonides. In D. G. Gee & B. A. Sturt (Eds.), *The Caledonide Orogen–Scandinavia and Related Areas* (pp. 69-88). Chichester.: John Wiley and Sons.

Brown, M., & Johnson, T. (2018). Secular change in metamorphism and the onset of global plate tectonics. *American Mineralogist, 103*(2), 181-196.

Brueckner, H. K., & Van Roermund, H. L. M. (2004). Dunk tectonics: A multiple subduction/eduction model for the evolution of the Scandinavian Caledonides. *Tectonics, 23*(2).

Brun, J. P., & Cobbold, P. R. (1980). Strain heating and thermal softening in continental shear zones: a review. *Journal of Structural Geology, 2*(1), 149-158.

Bryhni, I. (1989). *Status of the supracrustal rocks in the Western Gneiss Region, S. Norway.* Paper presented at the The Caledonides geology of Scandinavia. Conference dedicated to the Memory of Dr Sven Foyn.

Burg, J. P., & Gerya, T. V. (2005). The role of viscous heating in Barrovian metamorphism of collisional orogens: thermomechanical models and application to the Lepontine Dome in the Central Alps. *Journal of Metamorphic Geology, 23*(2), 75-95.

Burov, E., Francois, T., Agard, P., Le Pourhiet, L., Meyer, B., Tirel, C., . . . Brun, J. P. (2014a). Rheological and geodynamic controls on the mechanisms of subduction and HP/UHP exhumation of crustal rocks during continental collision : Insights from numerical models. *Tectonophysics, 631*, 212-1951.

Burov, E., Francois, T., Yamato, P., & Wolf, S. (2014b). Mechanisms of continental subduction and exhumation of HP and UHP rocks. *Gondwana Research, 25*(2), 464-493.

Butler, J., Jamieson, R., Dunning, G., Pecha, M., Robinson, P., & Steenkamp, H. (2018). Timing of metamorphism and exhumation in the Nordøyane ultra-high-pressure domain, Western Gneiss Region, Norway: New constraints from complementary CA-ID-TIMS and LA-MC-ICP-MS geochronology. *Lithos, 310*, 153-170.

Campani, M., Herman, F., & Mancktelow, N. (2010). Two- and three-dimensional thermal modeling of a low-angle detachment: Exhumation history of the Simplon Fault Zone, central Alps. *Journal of Geophysical Research: Solid Earth, 115*(B10).

Carlson, W. D. (2002). Scales of disequilibrium and rates of equilibration during metamorphism. *American Mineralogist, 87*(2), 185-204.

Carswell, D. A., Brueckner, H. K., Cuthbert, S. J., Mehta, K., & O'Brien, P. J. (2003a). The timing of stabilisation and the exhumation rate for ultra-high pressure rocks in the Western Gneiss Region of Norway. *Journal of Metamorphic Geology, 21*(6), 601-612.

Carswell, D. A., Tucker, R. D., O'Brien, P. J., & Krogh, T. E. (2003b). Coesite micro-inclusions and the U/Pb age of zircons from the Hareidland Eclogite in the Western Gneiss Region of Norway. *Lithos, 67*(3), 181-190.

Carswell, D. A., van Roermund, H. L. M., & Wiggers de Vries, D. F. (2006). Scandian Ultrahigh-Pressure Metamorphism of Proterozoic Basement Rocks on Fjørtoft and Otrøy, Western Gneiss Region, Norway. *International Geology Review, 48*(11), 957-977.

Chao, E., Shoemaker, E., & Madsen, B. (1960). First natural occurrence of Coesite. *Science, 132*(3421), 220-222.

Chauvet, A., & Dallmeyer, R. D. (1992). 40Ar/39Ar mineral dates related to Devonian extension in the southwestern Scandinavian Caledonides. *Tectonophysics, 210*(1), 155-177.

Chauvet, A., Kienast, Jr., Pinardon, J., & Brunel, M. (1992). Petrological constraints and PT path of Devonian collapse tectonics within the Scandian mountain belt (Western Gneiss Region, Norway). *J. Geol. Soc., 149*, 383-400.

Chemenda, A. I., Burg, J.-P., & Mattauer, M. (2000). Evolutionary model of the Himalaya–Tibet system: geopoem: based on new modelling, geological and geophysical data. *Earth and Planetary Science Letters, 174*(3), 397-409.

Chemenda, A. I., Mattauer, M., Malavieille, J., & Bokun, A. (1995). A mechanism for syn-collisional rock exhumation and associated normal faulting- Results from physical modelling. *Earth and Planetary Science Letters, 132*(1-4), 225-232.

Cheng, H., King, R. L., Nakamura, E., Vervoort, J. D., & Zhou, Z. (2008). Coupled Lu–Hf and Sm–Nd geochronology constrains garnet growth in ultra-high-pressure eclogites from the Dabie orogen. *Journal of Metamorphic Geology, 26*(7), 741-758.

Cherniak, D. J. (2000). Pb diffusion in rutile. *Contributions to Mineralogy and Petrology, 139*(2), 198-207.

Chopin, C. (1984). Coesite and pure pyrope in high-grade blueschists of the Western Alps: a first record and some consequences. *Contributions to Mineralogy and Petrology, 86*(2), 107-118.

Clark, C., Fitzsimons, I. C. W., Healy, D., & Harley, S. L. (2011). How Does the Continental Crust Get Really Hot? *Elements, 7*, 235-240.

Clark, C., Healy, D., Johnson, T., Collins, A. S., Taylor, R. J., Santosh, M., & Timms, N. E. (2015). Hot orogens and supercontinent amalgamation: A Gondwanan example from southern India. *Gondwana Research, 28*(4), 1310-1328.

Coes, L. (1953). A new dense crystalline silica. *Science, 118*(3057), 131-132.

Connelly, J. N. (2006). Improved dissolution and chemical separation methods for Lu-Hf garnet chronometry. *Geochemistry, Geophysics, Geosystems, 7*(4).

Corfu, F., Torsvik, T., Andersen, T., Ashwal, L., Ramsay, D., & Roberts, R. (2006). Early Silurian mafic–ultramafic and granitic plutonism in contemporaneous flysch, Magerøy, northern Norway: U–Pb ages and regional significance. *Journal of the Geological Society, 163*(2), 291-301.

Crittenden, M. D., Jr., Coney, P. J., & Davis, G. H. (1980). *Cordilleran metamorphic core complexes* (Vol. 153): Geological Society of America.

Cuthbert, S. J., Carswell, D. A., Krogh-Ravna, E. J., & Wain, A. (2000). Eclogites and eclogites in the Western Gneiss Region, Norwegian Caledonides. *Lithos, 52*(1), 165-195.

Cutts, J. A., & Smit, M. A. (2018). Rates of Deep Continental Burial From Lu-Hf Garnet Chronology and Zr-in-Rutile Thermometry on (Ultra)high-Pressure Rocks. *Tectonics, 37*(1), 71-88.

Cutts, J. A., Smit, M. A., Kooijman, E., & Schmitt, M. (2019a). Two-stage cooling and exhumation of deeply subducted continents. *Tectonics, 0*(ja).

Cutts, J. A., Smit, M. A., & Vrijmoed, J. C. (2019b). Evidence for non-lithostatic pressure in subducted continental crust. *Contributions to Mineralogy and Petrology, 175*(1), 3.

de Sigoyer, J., Chavagnac, V., Blichert-Toft, J., Villa, I. M., Luais, B., Guillot, S., . . . Mascle, G. (2000). Dating the Indian continental subduction and collisional thickening in the northwest Himalaya: Multichronology of the Tso Morari eclogites. *Geology, 28*(6), 487-490.

DesOrmeau, J. W., Gordon, S. M., Kylander-Clark, A. R. C., Hacker, B. R., Bowring, S. A., Schoene, B., & Samperton, K. M. (2015). Insights into (U)HP metamorphism of the Western Gneiss Region,

Norway: A high-spatial resolution and high-precision zircon study. *Chemical Geology, 414*, 138-155.

Dobrzhinetskaya, L. F., Eide, E. A., Larsen, R. B., Sturt, B. A., Trønnes, R. G., Smith, D. C., . . . Posukhova, T. V. (1995). Microdiamond in high-grade metamorphic rocks of the Western Gneiss region, Norway. *Geology, 23*(7), 597-600.

Dollase, W. (1971). Refinement of the crystal structures of epidote, allanite and hancockite. *American Mineralogist: Journal of Earth and Planetary Materials, 56*(3-4_Part_1), 447-464.

Duprat-Oualid, S., & Yamato, P. (2017). On the meaning of peak temperature profiles in inverted metamorphic sequences. *Geophysical Journal International, 210*(1), 130-147.

Duprat-Oualid, S., Yamato, P., & Pitra, P. (2013). Major role of shear heating in intracontinental inverted metamorphism: inference from a thermo-kinematic parametric study. *Tectonophysics, 608*, 812-831.

Duretz, T., Gerya, T. V., Kaus, B. J. P., & Andersen, T. B. (2012). Thermomechanical modeling of slab eduction. *Journal of Geophysical Research: Solid Earth, 117*(B8), n/a-n/a.

Eide, E. A., Torsvik, T., & Andersen, T. B. (1997). Absolute dating of brittle fault movements: Late Permian and late Jurassic extensional fault breccias in western Norway. *Terra Nova, 9*(3), 135-139.

Engi, M. (2017). Petrochronology Based on REE-Minerals: Monazite, Allanite, Xenotime, Apatite. *Reviews in Mineralogy & Geochemistry, 83*, 365-418.

Engi, M., Lanari, P., & Kohn, M. J. (2017). Significant Ages—An Introduction to Petrochronology. *Reviews in Mineralogy & Geochemistry, 83*, 1-12.

England, P. C., & Molnar, P. (1993). The interpretation of inverted metamorphic isograds using simple physical calculations. *Tectonics, 12*(1), 145-157.

England, P. C., & Thompson, A. B. (1984). Pressure—Temperature—Time Paths of Regional Metamorphism I. Heat Transfer during the Evolution of Regions of Thickened Continental Crust. *Journal of Petrology, 25*(4), 894-928.

Engvik, A. K., & Andersen, T. B. (2000). Evolution of Caledonian deformation fabrics under eclogite and amphibolite facies at Vårdalsneset, Western Gneiss Region, Norway. *Journal of Metamorphic Geology, 18*(3), 241-257.

Engvik, A. K., Austrheim, H., & Andersen, T. B. (2000). Structural, mineralogical and petrophysical effects on deep crustal rocks of fluid-limited polymetamorphism, Western Gneiss Region, Norway. *J. Geol. Soc., 157*, 121-134.

Engvik, A. K., Austrheim, H., & Erambert, M. (2001). Interaction between fluid flow, fracturing and mineral growth during eclogitization, an example from the Sunnfjord area, Western Gneiss Region, Norway. *Lithos, 57*(2), 111-141.

Ernst, W. G., & Liou, J. (2008). High- and ultrahigh-pressure metamorphism: Past results and future prospects. *American Mineralogist, 93*, 1771-1786.

Fletcher, I. R., McNaughton, N. J., Davis, W. J., & Rasmussen, B. (2010). Matrix effects and calibration limitations in ion probe U–Pb and Th–Pb dating of monazite. *Chemical Geology, 270*(1), 31-44.

Foley, S. F., Barth, M. G., & Jenner, G. A. (2000). Rutile/melt partition coefficients for trace elements and an assessment of the influence of rutile on the trace element characteristics of subduction zone magmas. *Geochimica et Cosmochimica Acta, 64*(5), 933-938.

Foreman, R., Andersen, T. B., & Wheeler, J. (2005). Eclogite-facies polyphase deformation of the Drøsdal eclogite, Western Gneiss Complex, Norway, and implications for exhumation. *Tectonophysics, 398*, 1-32.

Fossen, H. (1992). The role of extensional tectonics in the Caledonides of south Norway. *Journal of Structural Geology, 14*(8-9), 1033-1046.

Fossen, H., & Cavalcante, G. C. G. (2017). Shear zones – A review. *Earth-Science Reviews, 171*, 434-455.

Fossen, H., & Dunlap, W. J. (1998). Timing and kinematics of Caledonian thrusting and extensional collapse, southern Norway: evidence from 40Ar/ 39Ar thermochronology. *Journal of Structural Geology, 20*(6), 765-781.

Froitzheim, N., & Eberli, G. P. (1990). Extensional detachment faulting in the evolution of a Tethys passive continental margin, Eastern Alps, Switzerland. *GSA Bulletin, 102*(9), 1297-1308.

Gebauer, G., Schertl, H.-P., Brix, M., & Schreyer, W. (1997). 35 Ma old ultrahigh-pressure metamorphism and evidence for

very rapid exhumation in the Dora Maira Massif, Western Alps. *Lithos, 41*, 5-24.

Gee, D. G. (1975). A tectonic model for the central part of the Scandinavian Caledonides. *American Journal of Science, 275*(A), 468-515.

Gee, D. G. (1980). Basement-cover relationships in the central Scandinavian Caledonides. *Geologiska Foreningens i Stockholm Forhandlingar, 102*, 455-474.

Gerya, T., Perchuk, L. L., & Burg, J. P. (2008). Transient hot channels: perpetrating and regurgitating ultrahigh-pressure, high temperature crust–mantle associations in collision belts. *Lithos, 103*(1-2), 236-256.

Gerya, T., & Stöckhert, B. (2006). Two-dimensional numerical modeling of tectonic and metamorphic histories at active continental margins. *International Journal of Earth Sciences, 95*(2), 250-274.

Gieré, R., & Sorensen, S. S. (2004). Allanite and Other REE-Rich Epidote-Group Minerals. *Reviews in Mineralogy and Geochemistry, 56*(1), 431-493.

Gilotti, J. A., Nutman, A. P., & Brueckner, H. K. (2004). Devonian to Carboniferous collision in the Greenland Caledonides: U-Pb zircon and Sm-Nd ages of high-pressure and ultrahigh-pressure metamorphism. *Contributions to Mineralogy and Petrology, 148*(2), 216-235.

Gilotti, J. A., & Ravna, E. J. K. (2002). First evidence for ultrahigh-pressure metamorphism in the North-East Greenland Caledonides. *Geology, 30*(6), 551-554.

Govindaraju, K. (1994). Compilation of working values and sample description for 383 geostandards. *Geostandards Newsletter, 18*(S1), 1-158.

Grasemann, B., & Mancktelow, N. S. (1993). Two-dimensional thermal modelling of normal faulting: the Simplon Fault Zone, Central Alps, Switzerland. *Tectonophysics, 225*(3), 155-165.

Green, E. C. R., White, R. W., Diener, J. F. A., Powell, R., Holland, T. J. B., & Palin, R. M. (2016). Activity–composition relations for the calculation of partial melting equilibria in metabasic rocks. *Journal of Metamorphic Geology, 34*(9), 845-869.

Griffin, W. L., & Brueckner, H. K. (1980). Caledonian Sm–Nd ages and a crustal origin for Norwegian eclogites. *Nature, 285*(5763), 319-321.

Hacker, B. R. (2007). Ascent of the ultrahigh-pressure Western Gneiss Region, Norway. *Geological Society of America Special Paper, 419*, 171.

Hacker, B. R., Andersen, T. B., Johnston, S., Kylander-Clark, A. R. C., Peterman, E. M., Walsh, E. O., & Young, D. (2010). High-temperature deformation during continental-margin subduction & exhumation: The ultrahigh-pressure Western Gneiss Region of Norway. *Tectonophysics, 480*, 149-171.

Hacker, B. R., Andersen, T. B., Root, D. B., Mehl, L., Mattison, J. M., & Wooden, J. L. (2003a). Exhumation of high-pressure rocks beneath the Solund Basin, Western Gneiss Region of Norway. *Journal of Metamorphic Geology, 21*.

Hacker, B. R., Calvert, A., Zhang, R., Ernst, W. G., & Liou, J. (2003b). Ultrarapid exhumation of ultrahigh-pressure diamond-bearing metasedimentary rocks of the Kokchetav Massif, Kazakhstan? *Lithos, 70*(3-4), 61-75.

Hacker, B. R., & Gans, P. B. (2005). Continental collisions and the creation of ultrahigh-pressure terranes: Petrology and thermochronology of nappes in the central Scandinavian Caledonides. In *Geol. Soc. Am. Bull.* (Vol. 117, pp. 117-134).

Hacker, B. R., & Gerya, T. V. (2013). Paradigms, new and old, for ultrahigh-pressure tectonism. *Tectonophysics, 603*, 79-88.

Hacker, B. R., Gerya, T. V., & Gilotti, J. A. (2013). Formation and Exhumation of Ultrahigh-Pressure Terranes. *Elements, 9*(4), 289-293.

Hacker, B. R., Kylander-Clark, A., & Holder, R. (2019). REE partitioning between monazite and garnet: Implications for petrochronology. *Journal of Metamorphic Geology, 37*(2), 227-237.

Hacker, B. R., Kylander-Clark, A. R. C., Holder, R., Andersen, T. B., Peterman, E. M., Walsh, E. O., & Munnikhuis, J. K. (2015). Monazite response to ultrahigh-pressure subduction from U–Pb dating by laser ablation split stream. *Chemical Geology, 409*(C), 28-41.

Hacker, B. R., Luffi, P., Lutkov, V., Minaev, V., Ratschbacher, L., Plank, T., . . . Metcalf, J. (2005). Near-Ultrahigh Pressure Processing of Continental Crust: Miocene Crustal Xenoliths from the Pamir. *Journal of Petrology, 46*(8), 1661-1687.

Hacker, B. R., Ratschbacher, L., Webb, L., McWilliams, M. O., Ireland, T., Calvert, A., . . . Chateigner, D. (2000). Exhumation of ultrahigh-pressure continental crust in east central China: Late Triassic-Early Jurassic tectonic unroofing. *Journal of Geophysical Research, 105*(B6), 13339-13364.

Hacker, B. R., Wallis, S. R., Ratschbacher, L., Grove, M., & Gehrels, G. (2006). High-temperature geochronology constraints on the tectonic history and architecture of the ultrahigh-pressure Dabie-Sulu Orogen. *Tectonics, 25*(5).

Haggerty, S. E., Fung, A. T., & Burt, D. M. (1994). Apatite, phosphorus and titanium in eclogitic garnet from the upper mantle. *Geophysical Research Letters, 21*(16), 1699-1702.

Hartz, E. H., & Podladchikov, Y. Y. (2008). Toasting the jelly sandwich: The effect of shear heating on lithospheric geotherms and strength. *Geology, 36*(4), 331-334.

Henry, C., Michard, A., & Chopin, C. (1993). Geometry and structural evolution of ultra-high-pressure and high-pressure rocks from the Dora-Maira massif, Western Alps, Italy. *Journal of Structural Geology, 15*, 965-965.

Hermann, J., Rubatto, D., Korsakov, A., & Shatsky, V. S. (2001). Multiple zircon growth during fast exhumation of diamondiferous, deeply subducted continental crust (Kokchetav Massif, Kazakhstan). *Contributions to Mineralogy and Petrology, 141*(1), 66-82.

Holder, R. M., Hacker, B. R., Kylander-Clark, A. R. C., & Cottle, J. M. (2015). Monazite trace-element and isotopic signatures of (ultra) high-pressure metamorphism: Examples from the Western Gneiss Region, Norway. *Chemical Geology, 409*, 99-111.

Holder, R. M., Viete, D. R., Brown, M., & Johnson, T. E. (2019). Metamorphism and the evolution of plate tectonics. *Nature, 572*(7769), 378-381.

Holland, T. J. B., & Powell, R. (2003). Activity–composition relations for phases in petrological calculations: an asymmetric multicomponent formulation. *Contributions to Mineralogy and Petrology, 145*(4), 492-501.

Holland, T. J. B., & Powell, R. (2011). An improved and extended internally consistent thermodynamic dataset for phases of petrological interest, involving a new equation of state for solids. *Journal of Metamorphic Geology, 29*, 333-383.

Hoskin, P. W. O., & Schaltegger, U. (2003). The Composition of Zircon and Igneous and Metamorphic Petrogenesis. *Reviews in Mineralogy and Geochemistry, 53*(1), 27-62.

Hossack, J. R. (1984). The geometry of listric growth faults in the Devonian basins of Sunnfjord, W Norway. *Journal of the Geological Society, 141*(4), 629-637.

Hossack, J. R., Garton, M. R., & Nickelsen, R. P. (1985). The geological section from the foreland up to the Jotun thrust sheet in the Valdres area, south Norway. In D. G. Gee & B. A. Sturt (Eds.), *The Caledonide Orogen–Scandinavia and Related Areas* (pp. 443-456). Chichester.: John Wiley and Sons.

Jamtveit, B., Carswell, D. A., & Mearns, E. W. (1991). Chronology of the high-pressure metamorphism of Norwegian garnet peridotites/pyroxenites. *Journal of Metamorphic Geology, 9*(2), 125-139.

Jochum, K. P., Weis, U., Stoll, B., Kuzmin, D., Yang, Q., Raczek, I., . . . Enzweiler, J. (2011). Determination of Reference Values for NIST SRM 610–617 Glasses Following ISO Guidelines. *Geostandards and Geoanalytical Research, 35*(4), 397-429.

Jochum, K. P., Willbold, M., Raczek, I., Stoll, B., & Herwig, K. (2005). Chemical Characterisation of the USGS Reference Glasses GSA-1G, GSC-1G, GSD-1G, GSE-1G, BCR-2G, BHVO-2G and BIR-1G Using EPMA, ID-TIMS, ID-ICP-MS and LA-ICP-MS. *Geostandards and Geoanalytical Research, 29*(3), 285-302.

John, T., & Schenk, V. (2003). Partial eclogitisation of gabbroic rocks in a late Precambrian subduction zone (Zambia): prograde metamorphism triggered by fluid infiltration. *Contributions to Mineralogy and Petrology, 146*(2), 174-191.

John, T., Schenk, V., Mezger, K., & Tembo, F. (2004). Timing and PT Evolution of Whiteschist Metamorphism in the Lufilian Arc–Zambezi Belt Orogen (Zambia): Implications for the Assembly of Gondwana. *The Journal of Geology, 112*(1), 71-90.

Johnston, S., Hacker, B. R., & Andersen, T. B. (2007a). Exhuming Norwegian ultrahigh-pressure rocks: Overprinting extensional structures and the role of the Nordfjord-Sogn Detachment Zone. *Tectonics, 26*(5).

Johnston, S., Hacker, B. R., & Ducea, M. N. (2007b). Exhumation of ultrahigh-pressure rocks beneath the Hornelen segment of the Nordfjord-Sogn Detachment Zone, western Norway. *GSA Bulletin, 119*(9/10), 1232-1248.

Jourdan, F., & Renne, P. R. (2007). Age calibration of the Fish Canyon sanidine 40Ar/39Ar dating standard using primary K–Ar standards. *Geochimica et Cosmochimica Acta, 71*(2), 387-402.

Kalfoun, F., Ionov, D., & Merlet, C. (2002). HFSE residence and Nb/Ta ratios in metasomatised, rutile-bearing mantle peridotites. *Earth and Planetary Science Letters, 199*(1-2), 49-65.

Kaneko, Y., Katayama, I., Yamamoto, H., Misawa, K., Ishikawa, M., Rehman, H., . . . Shiraishi, K. (2003). Timing of Himalayan ultrahigh-pressure metamorphism: Sinking rate and subduction angle of the Indian continental crust beneath Asia. *Journal of Metamorphic Geology, 21*(6), 589-599.

Kaneko, Y., Maruyama, S., Terabayashi, M., Yamamoto, H., Ishikawa, M., Anma, R., . . . Katayama, I. (2000). Geology of the Kokchetav UHP-HP metamorphic belt, Northern Kazakhstan. *Island Arc, 9*(3), 264-283.

Kelly, E. D., Carlson, W. D., & Connelly, J. N. (2011). Implications of garnet resorption for the Lu–Hf garnet geochronometer: an example from the contact aureole of the Makhavinekh Lake Pluton, Labrador. *Journal of Metamorphic Geology, 29*(8), 901-916.

Kinny, P. D., & Maas, R. (2003). Lu–Hf and Sm–Nd isotope systems in zircon. *Reviews in Mineralogy and Geochemistry, 53*(1), 327-341.

Kiss, D., Podladchikov, Y., Duretz, T., & Schmalholz, S. M. (2019). Spontaneous generation of ductile shear zones by thermal softening: Localization criterion, 1D to 3D modelling and application to the lithosphere. *Earth and Planetary Science Letters, 519*, 284-296.

Kohn, M. J. (2009). Models of garnet differential geochronology. *Geochimica et Cosmochimica Acta, 73*(1), 170-182.

Kohn, M. J. (2014). "Thermoba-Raman-try": Calibration of spectroscopic barometers and thermometers for mineral inclusions. *Earth and Planetary Science Letters, 388*, 187-196.

Kohn, M. J., & Malloy, M. A. (2004). Formation of monazite via prograde metamorphic reactions among common silicates: implications for age determinations. *Geochimica et Cosmochimica Acta, 68*(1), 101-113.

Kooijman, E., Smit, M. A., Mezger, K., & Berndt, J. (2012). Trace element systematics in granulite facies rutile: implications for Zr geothermometry and provenance studies. *Journal of Metamorphic Geology, 30*(4), 397-412.

Korhonen, F. J., Saw, A. K., Clark, C., Brown, M., & Bhattacharya, S. (2011). New constraints on UHT metamorphism in the Eastern Ghats Province through the application of phase equilibria modelling and in situ geochronology. *Gondwana Research, 20*(4), 764-781.

Korneliussen, A., & Foslie, G. (1985). Rutile-bearing eclogites in the Sunnfjord region of Western Norway. *Bulletin-Norges geologiske undersokelse*(402), 65-71.

Krogh Ravna, E. J., & Terry, M. P. (2004). Geothermobarometry of UHP and HP eclogites and schists – an evaluation of equilibria among garnet–clinopyroxene–kyanite–phengite–coesite/quartz. *Journal of Metamorphic Geology, 22*(6), 579-592.

Krogh, T. E., Kamo, S. L., Robinson, P., Terry, M. P., & Kwok, K. (2011). U–Pb zircon geochronology of eclogites from the Scandian Orogen, northern Western Gneiss Region, Norway: 14–20 million years between eclogite crystallization and return to amphibolite-facies conditions. *Canadian Journal of Earth Sciences, 48*(2), 441-472.

Kröner, A., & Willner, A. (1998). Time of formation and peak of Variscan HP-HT metamorphism of quartz-feldspar rocks in the central Erzgebirge, Saxony, Germany. *Contributions to Mineralogy and Petrology, 132*(1), 1-20.

Kylander-Clark, A. R. C. (2017). Petrochronology by Laser-Ablation Inductively Coupled Plasma Mass Spectrometry. *Reviews in Mineralogy and Geochemistry, 83*(1), 183-198.

Kylander-Clark, A. R. C., Hacker, B. R., & Cottle, J. M. (2013). Laser-ablation split-stream ICP petrochronology. *Chemical Geology, 345*, 99-112.

Kylander-Clark, A. R. C., Hacker, B. R., Johnson, C. M., Beard, B. L., & Mahlen, N. J. (2009). Slow subduction of a thick ultrahigh-pressure terrane. *Tectonics, 28*.

Kylander-Clark, A. R. C., Hacker, B. R., Johnson, C. M., Beard, B. L., Mahlen, N. J., & Lapen, T. J. (2007). Coupled Lu–Hf and Sm–Nd geochronology constrains prograde and exhumation histories of high- and ultrahigh-pressure eclogites from western Norway. *Chemical Geology, 242*, 137-154.

Kylander-Clark, A. R. C., Hacker, B. R., & Mattinson, C. G. (2012). Size and exhumation rate of ultrahigh-pressure terranes linked to orogenic stage. *Earth and Planetary Science Letters, 321-322*, 115-120.

Kylander-Clark, A. R. C., Hacker, B. R., & Mattinson, J. M. (2008). Slow exhumation of UHP terranes: Titanite and rutile ages of the Western Gneiss Region, Norway. *Earth and Planetary Science Letters, 272*, 531-541.

Labrousse, L., Jolivet, L., Andersen, T. B., Agard, P., Hébert, R., Maluski, H., & Schärer, U. (2004). Pressure-temperature-time deformation history of the exhumation of ultra-high pressure rocks in the Western Gneiss Region, Norway. In D. L. Whitney, C. Teyssier, & C. S. Siddoway (Eds.), *Gneiss Domes in Orogeny* (Vol. 380, pp. 155-183): Geological Society of America.

Lanzirotti, A. (1995). Yttrium zoning in metamorphic garnets. *Geochimica et Cosmochimica Acta, 59*(19), 4105-4110.

Lapen, T. J., Johnson, C. M., Baumgartner, L. P., Mahlen, N. J., Beard, B. L., & Amato, J. M. (2003). Burial rates during prograde metamorphism of an ultra-high-pressure terrane: an example from Lago di Cignana, western Alps, Italy. *Earth and Planetary Science Letters, 215*(1-2), 57-72.

Larson, S. (1996). The Gothian and Sveconorwegian terranes of SW Sweden. *Gff, 118*(S4), 17-17.

Leech, M. L., Singh, S., & Jain, A. (2007). Continuous metamorphic zircon growth and interpretation of U-Pb SHRIMP dating: An example from the Western Himalaya. *International Geology Review, 49*(4), 313-328.

Li, Z., Gerya, T., & Burg, J. P. (2010). Influence of tectonic overpressure on P–T paths of HP–UHP rocks in continental collision zones: thermomechanical modelling. *Journal of Metamorphic Geology, 28*(3), 227-247.

Liou, J., Zhang, R., Ernst, W., Liu, J., & McLimans, R. (1998). Mineral parageneses in the Piampaludo eclogitic body, Gruppo di Voltri, western Ligurian Alps. *Schweizerische Mineralogische und Petrographische Mitteilungen, 78*(2), 317-335.

Liou, J. G., Ernst, W. G., Zhang, R. Y., Tsujimori, T., & Jahn, B. M. (2009). Ultrahigh-pressure minerals and metamorphic terranes – The view from China. *Journal of Asian Earth Sciences, 35*(3), 199-231.

Lister, G. S., & Davis, G. A. (1989). The origin of metamorphic core complexes and detachment faults formed during Tertiary continental extension in the northern Colorado River region, U.S.A. *Journal of Structural Geology, 11*(1), 65-94.

Little, T. A., Hacker, B. R., Gordon, S. M., Baldwin, S. L., Fitzgerald, P. G., Ellis, S., & Korchinski, M. (2011). Diapiric exhumation of Earth's youngest (UHP) eclogites in the gneiss domes of the D'Entrecasteaux Islands, Papua New Guinea. *Tectonophysics, 510*(1-2), 39-68.

Ludwig, K. R. (2003). *Isoplot, rev. 3.75. A geochronological toolkit for microsoft excel* (Vol. 5).

Mako, C. A., & Caddick, M. J. (2018). Quantifying magnitudes of shear heating in metamorphic systems. *Tectonophysics, 744*, 499-517.

Mancktelow, N. S. (1995). Nonlithostatic pressure during sediment subduction and the development and exhumation of high pressure metamorphic rocks. *Journal of Geophysical Research: Solid Earth, 100*(B1), 571-583.

Mancktelow, N. S. (2008). Tectonic pressure: Theoretical concepts and modelled examples. *Lithos, 103*(1-2), 149-177.

Martin, C., & Duchêne, S. (2015). Residual water in hydrous minerals as a kinetic factor for omphacite destabilization into symplectite in the eclogites of Vårdalsneset (WGR, Norway). *Lithos, 232*, 162-173.

Martin, C., Duchêne, S., Luais, B., Goncalves, P., Deloule, E., & Fournier, C. (2010). Behavior of trace elements in relation to Lu–Hf and Sm–Nd geochronometers during metamorphic dehydration–hydration in the HP domain of Vårdalsneset, Western Gneiss Region, Norway. *Contributions to Mineralogy and Petrology, 159*(4), 437-458.

Massonne, H. J., Kennedy, A., Nasdala, L., & Theye, T. (2007). Dating of zircon and monazite from diamondiferous quartzofeldspathic rocks of the Saxonian Erzgebirge–hints at burial and exhumation velocities. In: De Gruyter.

Massonne, H. J., & Schreyer, W. (1987). Phengite geobarometry based on the limiting assemblage with K-feldspar, phlogopite, and quartz. *Contributions to Mineralogy and Petrology, 96*(2), 212-224.

Mattinson, C. G., Wooden, J. L., Liou, J. G., Bird, D., & Wu, C. (2006). Age and duration of eclogite-facies metamorphism, North Qaidam HP/UHP terrane, Western China. *American Journal of Science, 306*(9), 683-711.

Mazzucchelli, M. L., Burnley, P., Angel, R. J., Morganti, S., Domeneghetti, M. C., Nestola, F., & Alvaro, M. (2018). Elastic geothermobarometry: Corrections for the geometry of the host-inclusion system. *Geology, 46*(3), 231-234.

McClelland, W. C., Power, S. E., Gilotti, J. A., Mazdab, F. K., & Wopenka, B. (2006). U-Pb SHRIMP geochronology and trace-element geochemistry of coesite-bearing zircons, North-East Greenland Caledonides. *SPECIAL PAPERS-GEOLOGICAL SOCIETY OF AMERICA, 403*, 23.

McDonald, C. S., Regis, D., Warren, C. J., Kelley, S. P., & Sherlock, S. C. (2018). Recycling argon through metamorphic reactions: The record in symplectites. *Lithos, 300-301*, 200-211.

Mearns, E. W. (1986). Sm-Nd ages for norwegian garnet peridotite. *Lithos, 19*(3), 269-278.

Meinhold, G. (2010). Rutile and its applications in earth sciences. *Earth-Science Reviews, 102*(1), 1-28.

Milnes, A. G., Wennberg, O. P., Skar, O., & Koestler, A. G. (1997). Contraction, extension and timing in the South Norwegian Caledonides: the Sognefjord transect. In J. P. Burg

& M. Ford (Eds.), *Orogeny Through Time, Geological Socienty Special Publication No. 121* (pp. 123-148). London: Geological Society.

Molnar, P., & England, P. (1990). Temperatures, heat flux, and frictional stress near major thrust faults. *Journal of Geophysical Research: Solid Earth, 95*(B4), 4833-4856.

Monteleone, B., Baldwin, S. L., Webb, L., Fitzgerald, P. G., Grove, M., & Schmitt, A. (2007). Late Miocene–Pliocene eclogite facies metamorphism, D'Entrecasteaux Islands, SE Papua New Guinea. *Journal of Metamorphic Geology, 25*(2), 245-265.

Mørk, M. B. E., & Mearns, E. W. (1986). Sm-Nd isotopic systematics of a gabbro-eclogite transition. *Lithos, 19*(3), 255-267.

Nabelek, P. I., Whittington, A. G., & Hofmeister, A. M. (2010). Strain heating as a mechanism for partial melting and ultrahigh temperature metamorphism in convergent orogens: Implications of temperature-dependent thermal diffusivity and rheology. *Journal of Geophysical Research: Solid Earth, 115*(B12).

Nakamura, D. (2009). A new formulation of garnet–clinopyroxene geothermometer based on accumulation and statistical analysis of a large experimental data set. *Journal of Metamorphic Geology, 27*(7), 495-508.

Nilsen, T. (1968). The relationship of sedimentation to tectonics in the Solund Devonian District of southwestern Norway. *Norges Geologiske Undersøkelse Bulletin, 259*, 1-108.

Norton, M. G. (1986). Late Caledonide Extension in western Norway: A response to extreme crustal thickening. *Tectonics, 5*(2), 195-204.

Norton, M. G. (1987). The Nordfjord-Sogn Detachment, W. Norway. *Norsk Geologisk Tidsskrift, 67*(2), 93-106.

Parrish, R. R., Gough, S. J., Searle, M. P., & Waters, D. J. (2006). Plate velocity exhumation of ultrahigh-pressure eclogites in the Pakistan Himalaya. *Geology, 34*(11).

Paton, C., Hellstrom, J., Paul, B., Woodhead, J., & Hergt, J. (2011). Iolite: Freeware for the visualisation and processing of mass spectrometric data. *Journal of Analytical Atomic Spectrometry, 26*(12), 2508-2518.

Paton, C., Woodhead, J. D., Hellstrom, J. C., Hergt, J. M., Greig, A., & Maas, R. (2010). Improved laser ablation U-Pb zircon geochronology through robust downhole fractionation correction. *Geochemistry, Geophysics, Geosystems, 11*(3).

Pearce, M. A., White, A. J. R., & Gazley, M. F. (2015). TCInvestigator: automated calculation of mineral mode and composition contours for thermocalc pseudosections. *Journal of Metamorphic Geology, 33*(4), 413-425.

Peterman, E., Hacker, B., & Baxter, E. (2009). Phase transformations of continental crust during subduction and exhumation: Western Gneiss Region, Norway. *European Journal of Mineralogy, 21*(6), 1097-1118.

Petrini, K., & Podladchikov, Y. (2000). Lithospheric pressure-depth relationship in compressive regions of thickened crust. *Journal of Metamorphic Geology, 18*, 67-77.

Platt, J. P. (2015). Influence of shear heating on microstructurally defined plate boundary shear zones. *Journal of Structural Geology, 79*, 80-89.

Powell, R., & Holland, T. J. B. (1988). An internally consistent dataset with uncertainties and correlations: 3. Applications to geobarometry , worked examples and a computer program. *Journal of Metamorphic Geology, 6*, 173-204.

Powell, R., & Holland, T. J. B. (2008). On thermobarometry. *Journal of Metamorphic Geology, 26*(2), 155-179.

Pyle, J. M., & Spear, F. S. (1999). Yttrium zoning in garnet coupling of major and accessory phases during metamorphic reactions. *Geological Materials Research*(6).

Ratschbacher, L., Frisch, W., Neubauer, F., Schmid, S. M., & Neugebauer, J. (1989). Extension in compressional orogenic belts: The eastern Alps. *Geology, 17*(5), 404-407.

Reddy, Wheeler, & Cliff. (1999). The geometry and timing of orogenic extension: an example from the Western Italian Alps. *Journal of Metamorphic Geology, 17*(5), 573-589.

Renne, P. R., Swisher, C. C., Deino, A. L., Karner, D. B., Owens, T. L., & DePaolo, D. J. (1998). Intercalibration of standards, absolute ages and uncertainties in 40Ar/39Ar dating. *Chemical Geology, 145*(1), 117-152.

Roberts, D. (2003). The Scandinavian Caledonides: event chronology, palaeogeographic settings and likely modern analogues. *Tectonophysics, 365*(1-4), 283-299.

Roberts, D., & Gee, D. G. (1985). An introduction to the structure of the Scandinavian Caledonides. In D. G. Gee & B. A. Sturt (Eds.), *The Caledonide Orogen–Scandinavia and Related Areas* (pp. 55-68). Chichester.: John Wiley and Sons.

Root, D. B., Hacker, B. R., Gans, P. B., Ducea, M. N., Eide, E. A., & Mosenfelder, J. L. (2005). Discrete ultrahigh-pressure domains in the Western Gneiss Region, Norway: implications for formation and exhumation. *Journal of Metamorphic Geology, 23*(1), 45-61.

Rubatto, D., & Hermann, J. r. (2001). Exhumation as fast as subduction? *Geology, 29*(1), 3-6.

Rudnick, R. L., Barth, M., Horn, I., & McDonough, W. F. (2000). Rutile-bearing refractory eclogites: missing link between continents and depleted mantle. *Science, 287*(5451), 278-281.

Samson, S. D., & Alexander, E. C. (1987). Calibration of the interlaboratory 40Ar□39Ar dating standard, MMhb-1. *Chemical Geology: Isotope Geoscience section, 66*(1), 27-34.

Scherer, E., Cameron, K. L., & Blichert-Toft, J. (2000). Lu–hf garnet geochronology: closure temperature relative to the Sm–Nd system and the effects of trace mineral inclusions. *Geochimica et Cosmochimica Acta, 64*(19), 3413-3432.

Scherer, E., Münker, C., & Mezger, K. (2001). Calibration of the lutetium-hafnium clock. *Science, 293*(5530), 683-687.

Schmalholz, S. M., & Duretz, T. (2015). Shear zone and nappe formation by thermal softening, related stress and temperature evolution, and application to the Alps. *Journal of Metamorphic Geology, 33*(8), 887-908.

Schmalholz, S. M., Duretz, T., Schenker, F. L., & Podladchikov, Y. Y. (2014). Kinematics and dynamics of tectonic nappes: 2-D numerical modelling and implications for high and ultra-high pressure tectonism in the Western Alps. *Tectonophysics, 631*, 160-175.

Schmalholz, S. M., & Podladchikov, Y. Y. (2013). Tectonic overpressure in weak crustal-scale shear zones and implications for the exhumation of high-pressure rocks. *Geophysical Research Letters, 40*(10), 1984-1988.

Scholz, C. H. (1988). The brittle-plastic transition and the depth of seismic faulting. *Geologische Rundschau, 77*(1), 319-328.

Shatsky, V., Jagoutz, E., Sobolev, N., Kozmenko, O., Parkhomenko, V., & Troesch, M. (1999). Geochemistry and age of ultrahigh pressure metamorphic rocks from the Kokchetav massif (Northern Kazakhstan). *Contributions to Mineralogy and Petrology, 137*(3), 185-205.

Sibson, R. H. (1977). Fault rocks and fault mechanisms. *Journal of the Geological Society, 133*(3), 191-213.

Sizova, E., Gerya, T., & Brown, M. (2012). Exhumation mechanisms of melt-bearing ultrahigh pressure crustal rocks during collision of spontaneously moving plates. *Journal of Metamorphic Geology, 30*(9), 927-955.

Sizova, E., Hauzenberger, C., Fritz, H., Faryad, S. W., & Gerya, T. (2019). Late Orogenic Heating of (Ultra) High Pressure Rocks: Slab Rollback vs. Slab Breakoff. *Geosciences, 9*(12), 499.

Skår, Ø. (2000). Field relations and geochemical evolution of the Gothian rocks in the Kvamsoy area, southern Western Gneiss Complex, Norway. *NORGES GEOLOGISKE UNDERSOKELSE, 437*, 5-24.

Skår, Ø., & Pedersen, R. B. (2003). Relations between granitoid magmatism and migmatization: U–Pb geochronological evidence from the Western Gneiss Complex, Norway. *Journal of the Geological Society, 160*(6), 935-946.

Skjerlie, K., Pedersen, R., Wennberg, O., & De La Rosa, J. (2000). Volatile phase fluxed anatexis of metasediments during late Caledonian ophiolite obduction: evidence from the Sogneskollen Granitic Complex, west Norway. *J. Geol. Soc., 157*, 1199-1213.

Slagstad, T., & Kirkland, C. L. (2018). Timing of collision initiation and location of the Scandian orogenic suture in the Scandinavian Caledonides. *Terra Nova, 30*(3), 179-188.

Smith, D. C. (1984). Coesite in clinopyroxene in the Caledonides and its implications for geodynamics. *Nature, 310*, 641-644.

Smye, A. J., Warren, C. J., & Bickle, M. J. (2013). The signature of devolatisation: Extraneous 40Ar systematics in high-pressure metamorphic rocks. *Geochimica et Cosmochimica Acta, 113*, 94-112.

Sobolev, N. V., & Shatsky, V. S. (1990). Diamond inclusions in garnets from metamorphic rocks: a new environment for diamond formation. *Nature, 343*(6260), 742.

Song, S., Zhang, L., Niu, Y., Su, L., Song, B., & Liu, D. (2006). Evolution from oceanic subduction to continental collision: a case study from the Northern Tibetan Plateau based on geochemical and geochronological data. *Journal of Petrology, 47*(3), 435-455.

Souche, A., Medvedev, S., Andersen, T. B., & Dabrowski, M. (2013). Shear heating in extensional detachments: Implications for the thermal history of the Devonian basins of W Norway. *Tectonophysics, 608*, 1073-1085.

Spandler, C., Hermann, J., Arculus, R., & Mavrogenes, J. (2003). Redistribution of trace elements during prograde metamorphism from lawsonite blueschist to eclogite facies; implications for deep subduction-zone processes. *Contributions to Mineralogy and Petrology, 146*(2), 205-222.

Spell, T. L., & McDougall, I. (2003). Characterization and calibration of 40Ar/39Ar dating standards. *Chemical Geology, 198*(3), 189-211.

Spencer, K. J., Hacker, B. R., Kylander-Clark, A. R. C., Andersen, T. B., Cottle, J. M., Stearns, M. A., . . . Seward, G. G. E. (2013). Campaign-style titanite U–Pb dating by laser-ablation ICP: Implications for crustal flow, phase transformations and titanite closure. *Chemical Geology, 341*, 84-101.

Stephens, M. B., & Gee, D. G. (1985). A tectonic model for the evolution of the eugeoclinal terranes in the central Scandinavian Caledonides. In D. G. Gee & B. A. Sturt (Eds.), *The Caledonide Orogen–Scandinavia and Related Areas* (pp. 953-978). Chichester.: John Wiley and Sons.

Stern, R. A., & Berman, R. G. (2001). Monazite U–Pb and Th–Pb geochronology by ion microprobe, with an application to in situ dating of an Archean metasedimentary rock. *Chemical Geology, 172*(1), 113-130.

Stipp, M., Stünitz, H., Heilbronner, R., & Schmid, S. M. (2002). The eastern Tonale fault zone: a 'natural laboratory' for crystal plastic deformation of quartz over a temperature range from 250 to 700°C. *Journal of Structural Geology, 24*(12), 1861-1884.

Swensson, E., & Andersen, T. B. (1991). Contact relationships between the Askvoll Group and the basement gneisses of the Western Gneiss Region (WGR), Sunnfjord, western Norway. *Norsk Geologisk Tidsskrift, 71*(1), 15-27.

Taylor, R. J. M., Clark, C., Fitzsimons, I. C. W., Santosh, M., Hand, M., Evans, N., & McDonald, B. (2014). Post-peak, fluid-mediated modification of granulite facies zircon and monazite in the Trivandrum Block, southern India. *Contributions to Mineralogy and Petrology, 168*(2), 1044.

Terry, M. P., Robinson, P., Hamilton, M. A., & Jercinovic, M. J. (2000). Monazite geochronology of UHP and HP metamorphism, deformation, and exhumation, Nordøyane, Western Gneiss Region, Norway. *American Mineralogist, 85*(11-12), 1651-1664.

Tillung, M. (1999). *Structural and Metamorphic Development of the Hyllestad–Lifjorden Area, Western Norway.* (Cand. Scient. Thesis), University of Bergen, Bergen, Bergen.

Tomascak, P. B., Krogstad, E. J., & Walker, R. J. (1996). U-Pb Monazite Geochronology of Granitic Rocks from Maine: Implications for Late Paleozoic Tectonics in the Northern Appalachians. *The Journal of Geology, 104*(2), 185-195.

Tomkins, H. S., Powell, R., & Ellis, D. J. (2007). The pressure dependence of the zirconium-in-rutile thermometer. *Journal of Metamorphic Geology, 25*(6), 703-713.

Torsvik, T. H., & Cocks, L. R. M. (2005). Norway in space and time: A Centennial cavalcade. *Norwegian Journal of Geology/Norsk Geologisk Forening, 85*.

Toussaint, G., Burov, E., & Jolivet, L. (2004). Continental plate collision: Unstable vs. stable slab dynamics. *Geology, 32*(1), 33-36.

Tribuzio, R., Messiga, B., Vannucci, R., & Bottazzi, P. (1996). Rare earth element redistribution during high-pressure–low-temperature metamorphism in ophiolitic Fe-gabbros (Liguria, northwestern Italy): implications for light REE mobility in subduction zones. *Geology, 24*(8), 711-714.

Tucker, R. D., Krogh, T., & Råheim, A. (1990). Proterozoic evolution and age-province boundaries in the central part of the Western Gneiss Region, Norway: Results of U-Pb dating of accessory minerals from Trondheimsfjord to Geiranger. *Mid-Proterozoic Laurentia-Baltica, 38*, 149-173.

Tucker, R. D., Robinson, P., Solli, A., Gee, D. G., Thorsnes, T., Krogh, T., . . . Bickford, M. E. (2004). Thrusting and extension in the scandian hinterland, Norway: New U-Pb ages and tectonostratigraphic evidence. In *Am. J. Sci.* (Vol. 304, pp. 477-532).

Vervoort, J. D., & Blichert-Toft, J. (1999). Evolution of the depleted mantle: Hf isotope evidence from juvenile rocks through time. *Geochimica et Cosmochimica Acta, 63*(3-4), 533-556.

Vervoort, J. D., & Patchett, P. J. (1996). Behavior of hafnium and neodymium isotopes in the crust: constraints from Precambrian crustally derived granites. *Geochimica et Cosmochimica Acta, 60*(19), 3717-3733.

Vervoort, J. D., Patchett, P. J., Söderlund, U., & Baker, M. (2004). Isotopic composition of Yb and the determination of Lu concentrations and Lu/Hf ratios by isotope dilution using MC-ICPMS. *Geochemistry, Geophysics, Geosystems, 5*(11).

Vrijmoed, J. C., Podladchikov, Y. Y., Andersen, T. B., & Hartz, E. H. (2009). An alternative model for ultra-high pressure in the Svartberget Fe-Ti garnet-peridotite, Western Gneiss Region, Norway. *European Journal of Mineralogy, 21*(6), 1119-1133.

Walsh, E. O., & Hacker, B. R. (2004). The fate of subducted continental margins: Two-stage exhumation of the high-pressure to ultrahigh-pressure Western Gneiss Region, Norway. *Journal of Metamorphic Geology, 22*, 671-687.

Walsh, E. O., Hacker, B. R., Gans, P. B., Grove, M., & Gehrels, G. (2007). Protolith ages and exhumation histories of (ultra)high-pressure rocks across the Western Gneiss Region, Norway. *GSA Bulletin, 119*(3/4), 289-301.

Walsh, E. O., Hacker, B. R., Gans, P. B., Wong, M. S., & Andersen, T. B. (2013). Crustal exhumation of the Western Gneiss Region UHP terrane, Norway: 40Ar/39Ar thermochronology and fault-slip analysis. *Tectonophysics, 608*, 1159-1179.

Warren, C. J., Beaumont, C., & Jamieson, R. A. (2008a). Formation and exhumation of ultra-high-pressure rocks during continental collision: Role of detachment in the subduction channel. *Geochemistry, Geophysics, Geosystems, 9*(4), n/a-n/a.

Warren, C. J., Beaumont, C., & Jamieson, R. A. (2008b). Modelling tectonic styles and ultra-high pressure (UHP) rock exhumation during the transition from oceanic subduction to continental collision. *Earth and Planetary Science Letters, 267*(1-2), 129-145.

Warren, C. J., Hanke, F., & Kelley, S. P. (2012). When can muscovite 40Ar/39Ar dating constrain the timing of metamorphic exhumation? *Chemical Geology, 291*, 79-86.

Webb, L., Baldwin, S. L., Little, T. A., & Fitzgerald, P. G. (2008). Can microplate rotation drive subduction inversion. *Geology, 36*(10), 823.

Werner, O., & Lippolt, H. J. (2000). White mica 40Ar/39Ar ages of Erzgebirge metamorphic rocks: simulating the chronological results by a model of Variscan crustal imbrication. *Geological Society, London, Special Publications, 179*(1), 323-336.

White, R. W., Powell, R., Holland, T. J. B., Johnson, T. E., & Green, E. C. R. (2014a). New mineral activity–composition relations for thermodynamic calculations in metapelitic systems. *Journal of Metamorphic Geology, 32*, 261-286.

White, R. W., Powell, R., & Johnson, T. E. (2014b). The effect of Mn on mineral stability in metapelites revisited: new a–x relations for manganese-bearing minerals. *Journal of Metamorphic Geology, 32*, 809-828.

Whitney, D. L., & Evans, B. W. (2010). Abbreviations for names of rock-forming minerals. *American Mineralogist, 95*(1), 185-187.

Wiest, J. D., Osmundsen, P. T., Jacobs, J., & Fossen, H. (2019). Deep Crustal Flow Within Postorogenic Metamorphic Core Complexes: Insights From the Southern Western Gneiss Region of Norway. *Tectonics, 38*(12), 4267-4289.

Yamamoto, H., Ishikawa, M., Anma, R., & Kaneko, Y. (2000). Kinematic analysis of ultrahigh-pressure–high-pressure metamorphic rocks in the Chaglinka–Kulet area of the Kokchetav Massif, Kazakhstan. *Island Arc, 9*(3), 304-316.

Yin, A., Manning, C. E., Lovera, O., Menold, C. A., Chen, X., & Gehrels, G. E. (2007). Early Paleozoic Tectonic and Thermomechanical Evolution of Ultrahigh-Pressure (UHP) Metamorphic Rocks in the Northern Tibetan Plateau, Northwest China. *International Geology Review, 49*(8), 681-716.

Young, D. (2017). Structure of the (ultra)high-pressure Western Gneiss Region, Norway: Imbrication during Caledonian continental margin subduction. *GSA Bulletin, 130*(5-6), 926-940.

Young, D., Hacker, B. R., Andersen, T. B., & Corfu, F. (2007). Prograde amphibolite facies to ultrahigh-pressure transition along Nordfjord, western Norway: Implications for exhumation tectonics. *Tectonics, 26*(1).

Young, D., Hacker, B. R., Andersen, T. B., & Gans, P. B. (2011). Structure and 40Ar/39Ar thermochronology of an ultrahigh-pressure transition in western Norway. *Journal of the Geological Society, London, 168*, 887-989.

Zack, T., & Kooijman, E. (2017). Petrology and Geochronology of Rutile. *Reviews in Mineralogy and Geochemistry, 83*(1), 443-467.

Zack, T., Kronz, A., Foley, S. F., & Rivers, T. (2002). Trace element abundances in rutiles from eclogites and associated garnet mica schists. *Chemical Geology, 184*(1-2), 97-122.

Zack, T., Stockli, D., Luvizotto, G., Barth, M., Belousova, E., Wolfe, M., & Hinton, R. (2011). In situ U–Pb rutile dating by LA-ICP-MS: 208 Pb correction and prospects for geological applications. *Contributions to Mineralogy and Petrology, 162*(3), 515-530.

Zhenyu, C., Yuchuan, C., Denghong, W., Jue, X., & Jianxiong, Z. (2005). *Rutiles in eclogite from the Sulu UHPM Terrane: a preliminary study.* Paper presented at the Mineral Deposit Research: Meeting the Global Challenge.

Zirakparvar, N. A., Baldwin, S. L., & Vervoort, J. D. (2011). Lu–Hf garnet geochronology applied to plate boundary zones: Insights from the (U)HP terrane exhumed within the Woodlark Rift. *Earth and Planetary Science Letters, 309*(1), 56-66.

6. APPENDICES

Appendix A

Sample locations for samples used within this study

Sample ID	Location	W	E	Zone	Latitude	Longitude
WGC18-001A	Hyllestad 1	301102	6786869	32V	61.1656992	5.30191132
WGC18-002	Hyllestad 1	301102	6786869	32V	61.1656992	5.30191132
WGC18-003	Hyllestad 2	301242	6786639	32V	61.1637066	5.30474292
WGC18-004	Hyllestad 2	301242	6786639	32V	61.1637066	5.30474292
WGC18-007	Hyllestad 6	293265	6794057	32V	61.2260270	5.14871877
WGC18-008	Drøsdal	295242	6796892	32V	61.2524621	5.18237505
WGC18-011	Drøsdal	295242	6796892	32V	61.2524621	5.18237505
WGC18-016	Vardehia	299318	6803502	32V	61.3137930	5.25111010
WGC18-022	Vardalsneset	295124	6806052	32V	61.3344572	5.17017611
WGC18-027	Naustdal	325524	6824775	32V	61.5170727	5.71968474
WGC18-029	Engebøfjellet	310528	6823065	32V	61.4946930	5.44011549

Appendix B

Electron Microprobe Methodology

Operating conditions

Quantitative compositions of silicates were determined using a Cameca SX-Five electron probe microanalyzer (EPMA), equipped with 5 tunable wavelength-dispersive spectrometers. The instrument is running PeakSite v6.2 software for microscope operation, and Probe for EPMA software (distributed by Probe Software Inc.) for all data acquisition and processing. Instrument operating conditions were 15 kV/20nA with a defocused beam of 2um.

The full list of elements analysed along with primary and interference standards are presented in Tables 1&2. Oxygen was calculated by stoichiometry, assuming that all Fe was Fe^{2+}. Matrix corrections of Armstrong-Love/Scott φ(ρz) (Armstrong (1988)) and Henke MACs were used for data reduction.

Beam damage and alkali element migration in silicate analyses were minimized via use of a defocused electron beam, in addition to use of the Mean Atomic Number (MAN) background correction (e.g. Donovan and Tingle (1996); Donovan et al. (2016)) over traditional 2 point background interpolation. This allows single point analysis time to be greatly shortened (from ~3.5 min to ~1.5 min), reducing the aforementioned effects of beam damage and element migration and their subsequent impact on the quality of analysis.

In addition to this, elements that are particularly mobile (e.g. Na, F, Cl) were analysed first on the detector and the Time Dependent Intensity (TDI) correction feature of Probe for EPMA was utilized (e.g. Donovan and Rowe (2005)). Using this method, the decay of x-ray counts over time is measured and modelled to return a t=0 intercept, and from this a concentration is calculated.

References

Armstrong, J.T., 1988. Quantitative analysis of silicate and oxide minerals: Comparison of Monte Carlo, ZAF, and φ(ρz) procedures. Microbeam Analysis, D.E. Newbury, ed., San Fransisco Press, 239-246.

Donovan, J.J., Tingle, T.N., 1996. An Improved Mean Atomic Number Background Correction for Quantitative Microanalysis. Microscopy and Microanalysis, 1, pp. 1-7.

Donovan, J.J., Rowe, M., 2005. Techniques for Improving Quantitative Analysis of Mineral Glasses. Geochimica et Cosmochimica Acta, Goldschmidt abstracts.

Donovan, J.J., Singer, J.W., Armstrong, J.T., 2016. A new EPMA method for fast trace element analysis in simple matrices. American Mineralogist, 101 (8), 1839-1853.

Table 1; EPMA setup for analysis of silicates

Element and Line	Diffracting Crystal (Sp#)	Background type/fit	kV/nA/spot size(µm)	Peak Count Time	Bkgd Count Times		# bkgd points acquired (Lo/Hi)	Standards*		Ov
					Lo	Hi		Primary Standard	Interference Standards	Int
Cl Ka	LPET (1)	MAN	15/20/5	15	-	-	-	545		
Ca Ka	LPET (1)	MAN	15/20/5	15	-	-	-	558		
K Ka	LPET (1)	MAN	15/20/5	15	-	-	-	541		
Ba Ka	LPET (1)	MAN	15/20/5	15	-	-	-	505		
F Ka	PC0 (2)	MAN	15/20/5	15	-	-	-	555	576,578	N
P Ka	LPET (3)	MAN	15/20/5	15	-	-	-	504		
Ti Ka	LPET (3)	MAN	15/20/5	15	-	-	-	559		
Na Ka	TAP (4)	MAN	15/20/5	15	-	-	-	735		
Si Ka	TAP (4)	MAN	15/20/5	15	-	-	-	735		
Mg Ka	TAP (4)	MAN	15/20/5	15	-	-	-	1335		
Al Ka	TAP (4)	MAN	15/20/5	15	-	-	-	1327		
Fe Ka	LLIF (5)	MAN	15/20/5	15	-	-	-	502		
Mn Ka	LLIF (5)	MAN	15/20/5	15	-	-	-	557	577	
Cr Ka	LLIF (5)	MAN	15/20/5	15	-	-	-	577		
Zn Ka	LLIF (5)	MAN	15/20/5	15	-	-	-	546		
Ni Ka	LLIF (5)	MAN	15/20/5	15	-	-	-	1347		

* Standard # refers to internal database. Full list of standards in Table 2

Table 2; Standard information

Reference #	Mineral composition	Natural/Synthetic	Manufacturer
502	Almandine garnet	Natural	Astimex
505	Barite	Natural	Astimex
541	Sanidine	Natural	Astimex
545	Tugtupite	Natural	Astimex
546	Willemite	Natural	Astimex
555	Apatite	Natural	Astimex
557	Rhodonite	Natural	Astimex
558	Wollastonite	Natural	P&H and Associates
559	Rutile	Natural	P&H and Associates
576	Periclase	Synthetic	P&H and Associates
577	Chromium oxide	Synthetic	P&H and Associates
578	Specularite	Natural	P&H and Associates
735	Albite	Natural	C.M. Taylor
1327	Anorthite	Natural	NMNH-137041
1335	Olivine	Natural	NMNH-113312-44
1347	Nickel Olivine	Synthetic	NMNH

Appendix C

Modelled conditions for shear heating modelling

```
tau = 45 ;                  % shear zone stress, MPa
vel = 3 ;                   % shear zone velocity, cm per year
width = 4 ;                 % shear zone width, km
zShear = 58 ;               % shear zone depth, km
tShear = 10 ;               % shear zone duration, My
depth = 20;                 % base depth of heat producing layer, km
heat_prod= 1.5;             % constant volumetric heat production, µW m^-3

erosion = 35 ;              % amount of uplift, km
t_erosion = 50 ;            % duration of uplift, My
delay_erosion = 5 ;         % delay before uplift starts, My

deltaz = 0.5 ;              % depth increment, km
maxz = 150 ;                % depth to base lithosphere
numz = maxz / deltaz ;      % number of depths
z = 0:deltaz:maxz ;         % array of depths

deltat = 0.1 ;              % time increment, My
maxt = 80 ;                 % time to end of model run, My
numt = maxt / deltat ;      % time to end of model run, My
t = 0:deltat:maxt ;         % array of times

Tbaselith = 1300 + 273 ;    % fixed T at base lithosphere, deg K
k = 2.25 ;                  % Watts per metre per K
zCrust = 35 ;               % initial thickness of crust, km
zLith = maxz ;              % thickness of lithosphere, km
rho = 2700 ;                % density, kg per cu metre
cp = 1000 ;                 % specific heat capacity, J per kg per K
```

tau (shear zone stress, MPa) was changed to equal 1 for non-shear stress conditions, all other values remained the same between runs.